Geochemical Investigation of Weathering in a High Arctic Watershed and Provenance of Sediments in Kongressvatnet, Svalbard, Norway

Maya Li Wei-Haas

Submitted to the Department of Geology
of Smith College
in partial fulfillment
of the requirements for the degree of
Bachelor of Arts

Robert Newton, Faculty Advisor

Al Werner, Mt. Holyoke College and
Mike Retelle, Bates College,
Project Advisors

May 11, 2009

Caveat Lector

In this thesis, landforms will be referred to in their proper Norwegian names, which generally are composed of a prefix denoting the locality and a suffix describing the geomorphic feature. The Norwegian words for the primary features discussed in this study are as follows: "-dalen" means valley, "-vatnet" is a lake, "-elva" denotes a river, and "-breen" means glacier. Therefore, Kongress Valley becomes *Kongressdalen*, Lake Kongress is *Kongressvatnet*, etc.

Table of Contents

ABSTRACT

This study uses changes in the chemistry and mineralogy of lake and surface sediments in a small lake in Kongress Valley (Kongressdalen), to interpret Late Holocene climate change in Western Spitsbergen, Svalbard.

Changes in clay mineralogy across an inactive outwash fan (Black Fan) in the valley reflect weathering since the fan's formation during the Little Ice Age (LIA) (1550-1920). X-Ray Diffraction analysis of clay samples from the meltwater channels and the Kapp Starostin rocks that compose the fan reveal a strong 10 Å peak, unaffected by ethylene glycol solvation or heating to 375°C and 550 °C, indicative of illite. However, samples collected from vegetated debris flows between the meltwater channels reveal a diminished 10 Å phase and a slightly expandable peak at approximately 14 Å, unaffected by magnesium and glycerol saturation (d 060 of 1.54 Å), indicative of vermiculite. The inverse relationship between these peaks reflects the weathering of illite to vermiculite, suggesting an early period of Kapp Starostin Fm. deposition subsequently eroded by meltwater from Kongressbreen (glacier) during the LIA.

Changes in lake sediment chemistry should reflect changing sources of sediment inflow as meltwater from an advancing ice activated the Black Fan. X-Ray Fluorescence analysis of the White and Black Fan, which are the only sources of sediment inflow to the lake, reveals that the Black Fan sediments have greater concentrations of K_2O, Fe_2O_3, Zr, and Cr, while the White Fan is characterized by higher concentrations of MgO, CaO, Sr, and U. However, analysis of sediment cores from the central part of the lake reveals a chemical composition that resembles only that of the White Fan sediment, indicating almost no Black Fan input into Kongressvatnet. The most likely hypothesis to explain this absence is that Kongressbreen was a cold-based glacier and therefore did not produce fine glacial flour from scour of bedrock.

Despite the dominant White Fan signature in the core sediments, ITRAX Scanning X-Ray Fluorescence analysis reveals significant variations in core chemistry with depth, which is likely due to changes in climate. Periodic, massive high calcium layers, lacking internal laminations characterize the upper 200 mm of the core, which correlates using MS to cores dated to the LIA (Guilizzoni et al., 2006). Preliminary SEM analysis reveals the presence of euhedral, sharp-edged rhombohedra and fibrous needles of calcite, high-Mg calcite, and dolomite, suggesting the precipitation of carbonate. The current supersaturation of Kongressvatnet waters below the chemocline with respect to calcite further supports this hypothesis. Alternatively, periods of extended ice cover during which the formation of lake ice concentrates the calcium in the underlying lake water, and may result in the formation of cryogenic calcite. Anomalous peaks in iron and sulfur characterize the lower core (300-400 mm), which MS correlations indicate corresponds to the Medieval Warm Period (Guilizzoni et al., 2006). An increase in organic terriginous inflow during this period likely spurs the activity of sulfur reducing bacteria, resulting in reducing conditions and the precipitation of iron sulfides. This analysis suggests that although provenance cannot be used in Kongressvatnet to constrain the timing of the Little Ice Age, changes in climate are intimately associated with fluctuations in lake chemistry and the lake's biogeochemical cycles, providing the opportunity to interpret past climate change from lake sediment chemistry.

Acknowledgements

Thanks to Al Werner (Mt. Holyoke College), Mike Retelle (Bates College), and Steve Roof (Hampshire College) for introducing me to the world of polar research. Thank you to my fellow REU field partners, Megan, Emily, Dave, Kristen, Jesse, Steve, Leo, Antoine, Missy, and Anthony with whom I walked hundreds of miles. I could not have imagined a better group to share this experience with.

Thanks to Erik Brown and Marian Kramer from the Scanning XRF facility at the University of Minnesota, Duluth for their willingness to help me in analyzing the Kongress core sediments. Thanks to Mike Rhodes and especially Mike Vollinger from the X-Ray Fluorescence lab at the University of Massachusetts for their uncountable hours spent helping me with elemental analysis.

Thank you to the Smith College Geology Department who have made my last four years truly memorable. A special thanks to my advisor, Robert Newton, for his continued support and inspiring enthusiasm throughout this venture. Thank you for your guidance and patience throughout this crazy year. Thanks to the people who have helped me understand the many facets of this project: Amy Rhodes, Bosiljka Glumac, and John Brady (Smith College). Thanks to Kathy Richardson and Tony Caldanaro for help in the technical aspects of writing a thesis.

To my housemates who, although I didn't always appreciate it at the time, forced me out of the lab at least once a day. You have helped keep me sane this year. Thank you to my parents, for continually supporting my desires to continue research. Special thanks to my mother, who helped push me through the last hurdles of writing.

This project would not be possible without the support from the University in Svalbard and the Svalbard Research Experience for Undergraduates. Funding for this project was provided by the U.S. National Science Foundation Research Experience for Undergraduates, Nancy Kershaw Tomlinson Fund, Smith College Geology Marshall Schalk Fund, Smith College's President's Discretionary Fund, and the Mellon Mays Foundation.

LIST OF FIGURES

LIST OF TABLES

1. INTRODUCTION

Global climate change is the most important issue facing our society today. Understanding past climate dynamics is essential to apprehend the implications and issues associated with the current climate change. The Arctic is extremely sensitive to variations in climate due to a series of positive feedback mechanisms such as changes in snow cover, sea ice, and cloud dynamics (Overpeck et al., 1997). These feedback mechanisms both result from and subsequently accelerate climate change in the Arctic, and thus act as the driving forces in global climate fluctuations. Together with the remoteness of most Arctic environments from anthropogenic influence, this sensitivity makes this region an optimal location to study climate. Since historic climate records cover only the last 100 years, it is necessary to use proxies to determine older climate fluctuations (Overpeck et al., 1997). Polar lake basin sediments in particular provide valuable proxies for climate change in variations in grain size, mineralogy, chemistry, carbon content, and sedimentation rate (Smol et al., 1991).

This study focuses on interpreting Late Holocene climate change based on the sediment chemistry and mineralogy of Kongressvatnet, a small lake located in Western Spitsbergen, Svalbard (Figure 1.1). The lake catchment is composed of two distinct rock types and is an ideal location for study of past climate change since glacial advance influences the provenance of sediments deposited into the lake.

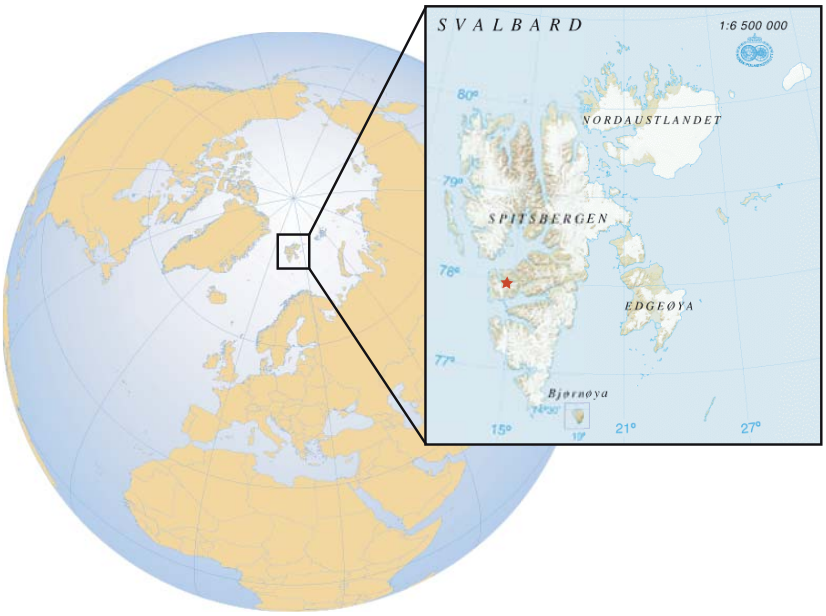

Figure 1.1. Location of Spitsbergen, the largest island in the Svalbard archipelago (study site labeled with a black star). Map adapted from the Norsk Polarinstituitt online.

1.1 Geographic Setting

Svalbard is an archipelago located above the Arctic Circle lying between 78° to 81°N latitude and 10° to 35°E longitude, on the boundary between the Barents Sea, the Norwegian Sea, and the Arctic Ocean (Humlum et al., 2005) (Figure 1.1). Svalbard consists of six principal islands and covers a total area of 63,000 km^2 (Humlum et al., 2005). Kongressvatnet is located in western Spitsbergen, within western Nordenskiøld Land, whose boundaries extend between Isfjord and Bellsund (Figure 1.2). This small glacial lake is positioned at an elevation of 94 m, on a topographic divide between Linnédalen to the west and Grønfjord to the east at 78^o1' N and 13^o59' E (Bøyum and Kjensmo, 1970) (Figure 1.2).

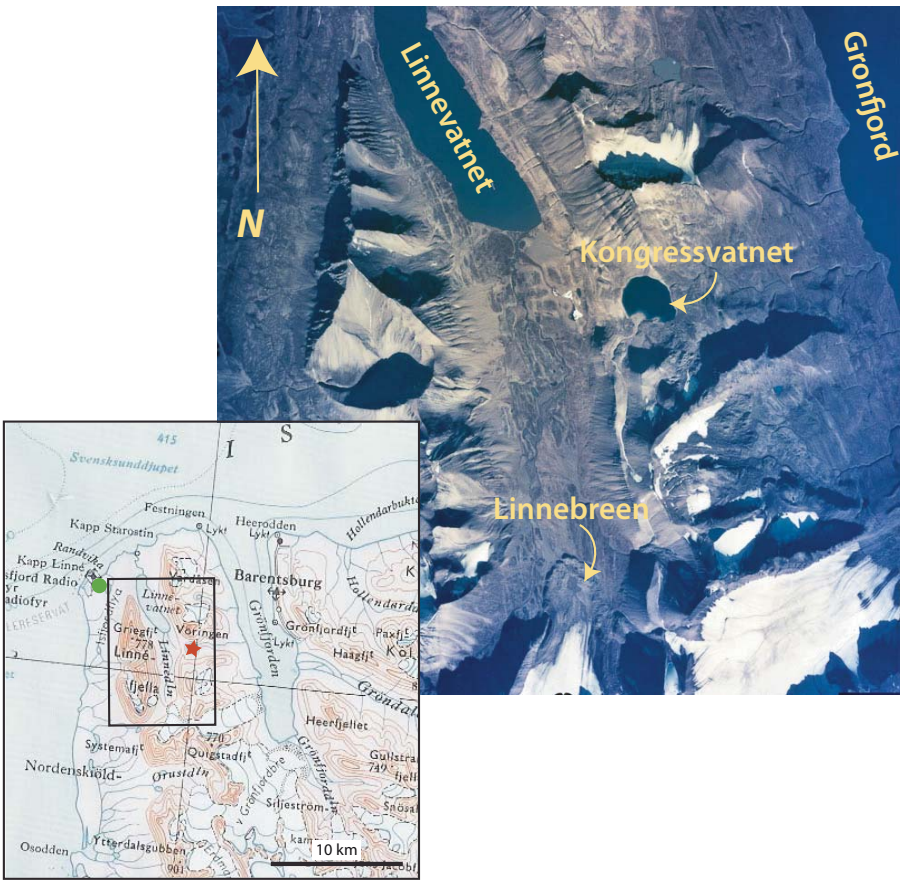

Figure 1.2. Topographic map and aerial photograph of study location (red star). Isfjord radio station is located in Kapp Linné, 9 km NW of Kongressvatnet (green circle). Aerial photo and map adapted from the Norsk Polarinstituitt.

1.2 Climactic Setting

Svalbard has a tundra climate based on the Köppen-Greiger climate classification (Peel et al., 2007), yet the comparatively mild climate of western Spitsbergen is the result of the warm Gulf Stream flowing just off of the west coast (Guilizzoni et al., 2006). The mean annual air temperature is -6.3 °C (Guilizzoni et al., 2006). However, recent records reveal warmer winters evidenced by a slightly warmer average air temperature of -5.8 °C measured between 1975 and 2000 (Ingólfsson, 2006). February is the coldest month of the year with the average annual air temperatures at Kapp Linné, located 9 km to the northwest of Kongressvatnet, of approximately -12 °C (Guilizzoni et al., 2006; Ingólfsson, 2006). July is the warmest month, with temperatures

averaging 5 °C in Kapp Linné (Guilizzoni et al., 2006). Annual precipitation along the west coast of Spitsbergen ranges from 400-600 mm, with the driest period occurring from April to May (Ingólfsson, 2006). Ice persists on Kongressvatnet for most of the year, except for 2-3 months during the summer (Guilizzoni et al., 2006).

1.3 Geologic Setting

Svalbard is located in the northwest corner of the Barents Shelf and has a rich geologic history, with outcrops dating to the Precambrian (Figure 1.3). In northern Spitsbergen, these units consist of high-grade metamorphic gneiss and migmatite complexes (Ingólfsson, 2006).

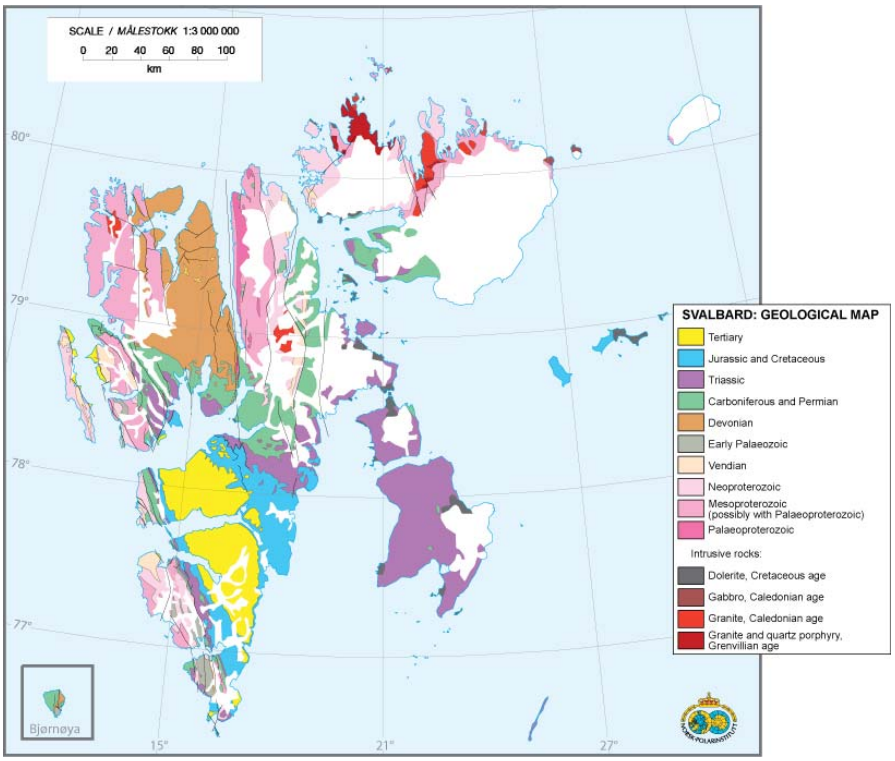

Figure 1.3. Simplified geologic map of Spitsbergen (From Hjelle, 1993).

Unmetamorphosed sedimentary rocks and low-grade metasedimentary and marble units compose the Precambrian assemblage that outcrops in a North-South trending belt along the Western Coast of Spitsbergen (Ingólfsson, 2006). Cambrian and Ordovician units composed of calcareous limestone are oriented along the same North-South belt east of the Precambrian rocks. These units were deposited in the Lapetus Ocean, evidenced by abundant trilobite and graptolite fossil remains (Ingólfsson, 2006) (Figure 1.3).

During the Silurian the Lapetus Ocean closed and Laurentia, Baltica, and Avalonia collided in the Caledonain Orogeny, causing abundant granite intrusions and variable amounts of deformation throughout Svalbard (Ingólfsson, 2006). The Hecla Hoek Formation, which is positioned to the west of Linnévatnet, is a highly deformed phyllite unit metamorphosed during this orogeny (Ingólfsson, 2006) (Figure 1.4).

Paleomagnetic records indicate that the archipelago began migrating northward during the Devonian period, starting near the equator but traveling to approximately 25°-30° N latitude by the Carboniferous (Ingólfsson, 2006; Chwieduk, 2007). The abundant flora and fauna that developed during this period resulted in the formation of coal seams, the erosion and deposition of which make radiocarbon dating difficult in Linnévatnet (Ingólfsson, 2006).

The two primary units present in Kongressdalen were deposited during the cyclic marine transgressions and regressions in the transition between the Upper Carboniferous and Permian periods. The dolomitic limestone of the Gipshuken Formation was deposited as Svalbard developed into a carbonate platform (Chwieduk, 2007; Braathen, 2007) (Figure 1.5). Sea level fluctuations during the deposition of this unit and associated periodic subaerial exposure resulted in the formation of gypsum and anhydrite evaporite deposits (Ingólfsson, 2006).

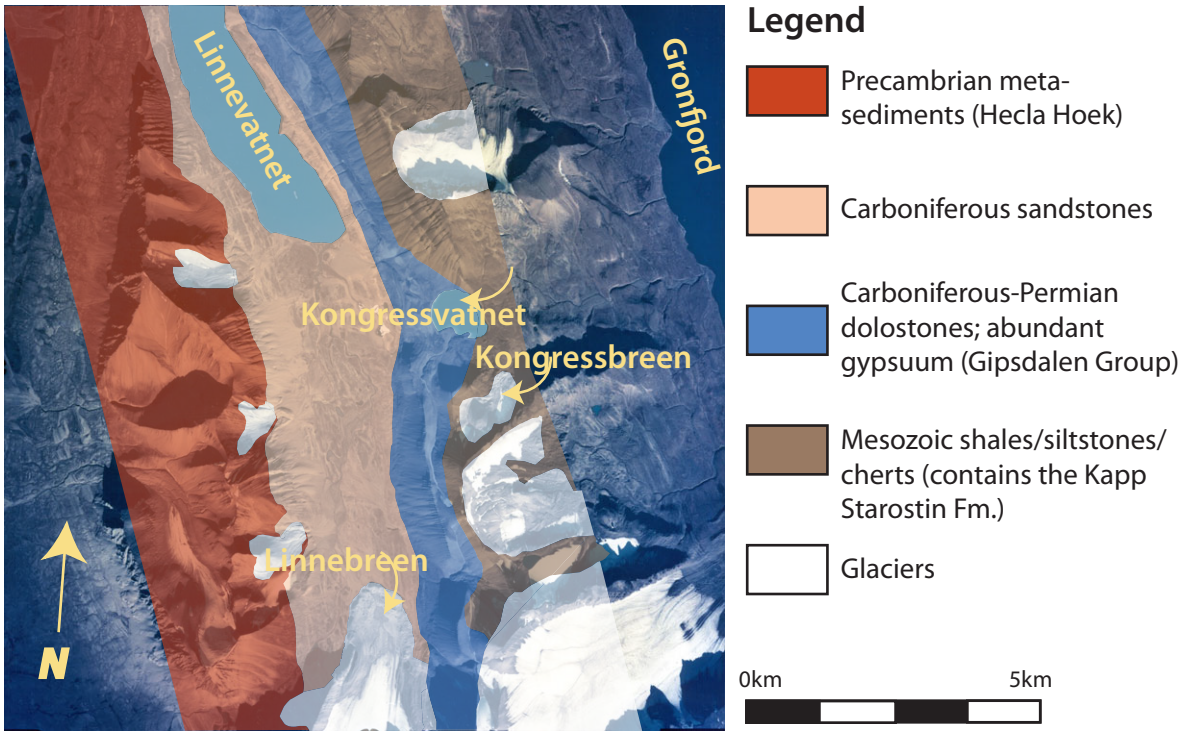

Figure 1.4. Simplified geologic map of Linnédalen and Kongressdalen superimposed on an aerial photograph of the region (Based on Hjelle et al., 1986; aerial photo from the Norsk Polarinstituitt, 1995).

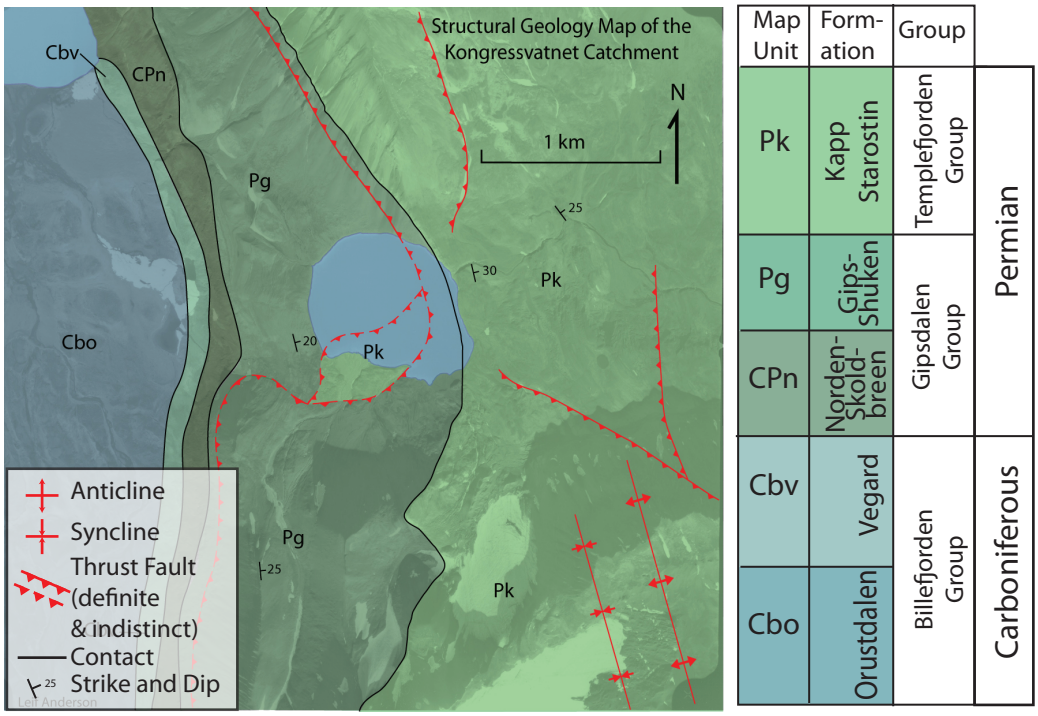

Figure 1.5. Geologic map of the Kongressvatnet compiled by a previous Svalbard Research for Undergraduates (REU) participant (Anderson, 2007).

Extensive marine transgression occurred on Svalbard during the Permian period and renewed clastic influx resulted in the deposition of the Kapp Starostin Formation that outcrops to the east and south of the lake basin (Figure 1.5) (Cutbill and Challinor, 1956; Braathen, 2007). This unit, deposited in an outer marine shelf environment, consists predominantly of fine-grained siliceous beds containing abundant sponge spicules, brachiopods, corals, mollusks, echinoderms, and foraminfera (Chwieduk, 2007). Very fine-grained glauconitic sandstones with subordinate limestone characterize the Kapp Starostin Formation exposed in the catchment of Kongressvatnet (Anderson, 2007) (Figure 1.5).

Svalbard emerged as an archipelago during extensive Mesozoic and Cenozoic crustal movements (Braathen, 2007). During the early Eocene, dextral strike-slip separated Svalbard from Greenland, which opened the Barents Shelf and formed the Greenland and Norwegian seas (Braathen, 1997; Lowell, 1972; Saalmann and Thiedg, 2001). Svalbard reached its current location above the Arctic Circle at the end of the Tertiary period (Ingólfsson, 2006).

1.4 Glacial History of Svalbard

Svalbard has undergone numerous periods of glaciation during the last few hundred thousand years (Mangerud et al., 1998) and currently 60% of the surface area remains ice-covered (Norsk Polarinstituitt Online). The Last Glacial Maximum (LGM) in Svalbard occurred during Late Weichselian (30-15 ka), when the glaciers extended out over the Barents Sea, forming the Barents Ice Sheet (Mangerud et al., 1998; Mangerud and Landvik, 2007) (Figure 1.6). Glacial deposits exposed in Linnédalen coarsen upward from marine silt to beach gravel and are capped with a diamicton that is interpreted as basal till. These deposits represent the

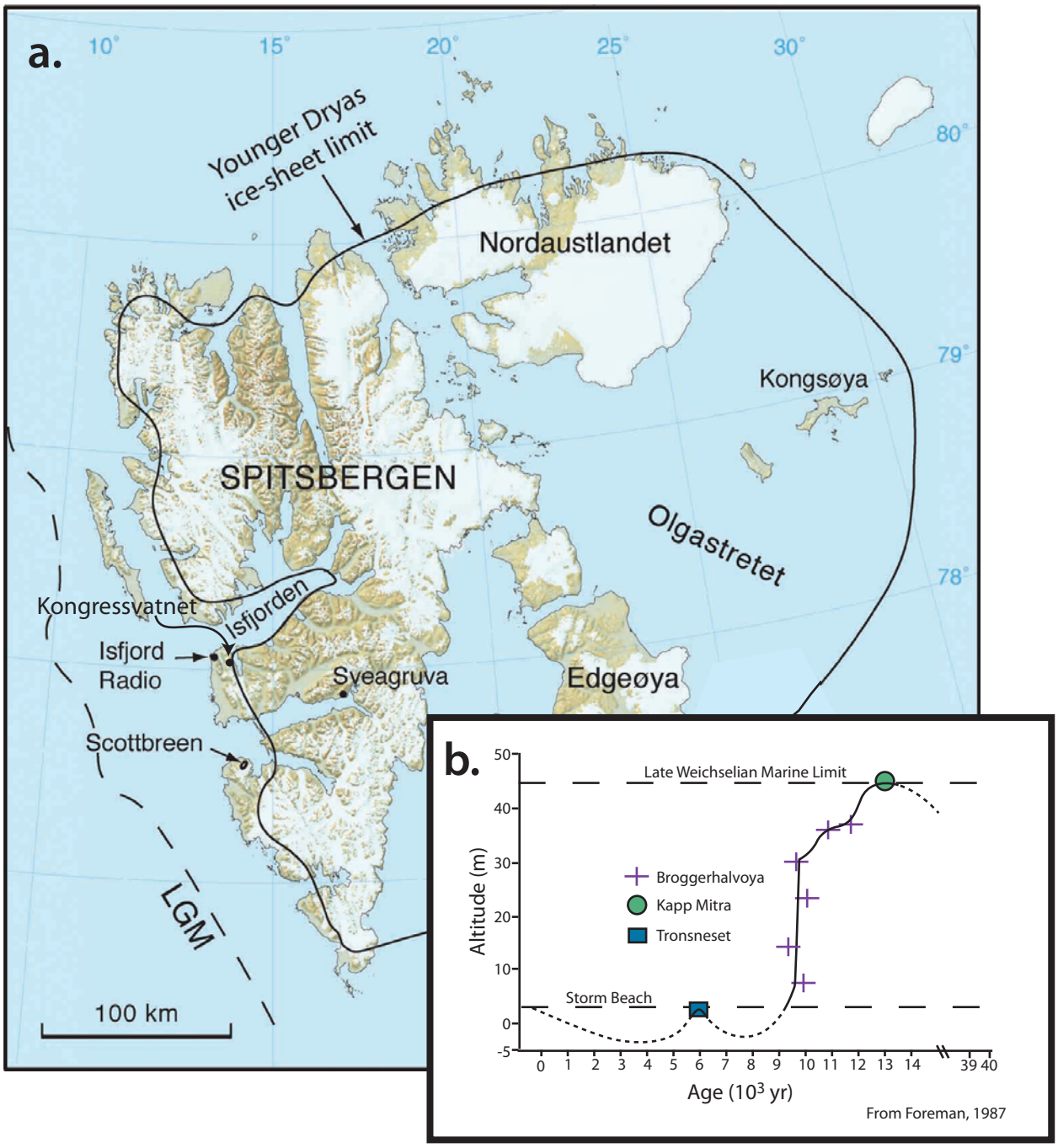

Figure 1.6. a. Map displaying the current glacial extent (white shaded regions), the maximum extent of the Barent's Ice Sheet during the Last Glacial Maximum (LGM) (dashed line) and the limit of the Younger Dryas ice sheet on Svalbard (From Mangerud et al). Errors in the YD limit are assumed to rarely exceed 30 km along the west coast yet may exceed 100 km in the eastern limit. The approximate position of Kongressvatnet and Isfjord radio, 9km to the northeast of Kongressvatnet, are labeled. b. Sea level curve for Spitsbergen based on radiocarbon dates and elevations of drift wood and Whale vertebra. The dashed line indicates inferred regions of the curve (Adapted from Foreman 1987).

advance of Linnébreen, the glacier in the valley to the west of Kongressdalen, during the Last Glacial Maximum (Mangerud et al., 1998).

Deglaciation of the Barents ice sheet began approximately 12,300 years BP (Mangerud and Svendsen, 1992). Morphologic analysis of raised beach terraces in Brøggerhalvøya, located approximately 115km NNW of Kongress along the coast of Spitsbergen, indicates a slow marine regression due to isostatic rebound with at least three intervening halts or possible transgressions between 13,000 yr BP and 10,000 yr BP (Forman, 1987) (Figure 1.6b). After this period, sea level was recorded to fall rapidly as glaciers disappeared from the Spitsbergen Fjords until modern sea level was attained at approximately 9,000 yr BP (Forman, 1987).

During deglaciation, isostatic rebound of the land resulted in the separation of the marine Linnéfjord from the sea and the formation of Linné Valley at approximately 9,600 BP (Svendsen and Mangerud, 1997). Lake cores at Linnévatnet suggest that few glaciers existed in Svalbard during the early to mid Holocene (Svendsen and Mangerud, 1997). Despite evidence of extensive glaciation during the Younger Dryas, which began between 12,000-13,000 yr BP and terminated ~11,500 yr BP (Alley, 2000; Houghten et al., 2000), and 8.2 cal yr BP event throughout Western Europe and Scandinavia, similar glacial advance has not been documented in Spitsbergen (Mangerud and Landvik, 2007; Anderson et al, 1995).

Linnébreen reformed during the late Holocene, 4,000-5,000 years ago, as the climate became progressively colder (Svendsen and Mangerud, 1996). Renewed glaciation as determined from dating of exhumed organic material, lake core analysis, and moraine records mark two Neoglacial advances which comprises the Little Ice Age (LIA) in Svalbard: a period that began during the fourteenth century and terminated during the early twentieth century (Ingolfsson, 2006; Grove, 2001; Svendsen and Mangerud, 1997; Werner, 1993).

There is significant spatial and temporal variation of maximum advance of glacial ice during the LIA throughout the northern hemisphere and the length of the LIA in Svalbard is still under debate. In Western Norway, LIA glacial advances peak around AD 1350, 1600, and 1850-1860 (Nesje et al., 2008). Data from ice-core records from the Lomonosov plateau, located in northeast Spitsbergen, suggest two phases of maximum glaciation, the first during 1180-1500 AD and the second 1700-1900 AD (Grove, 2001).

The Little Ice Age advance is commonly attributed to lower summer temperatures. However, Nesje et al. (2008) suggests that cool summers alone cannot account for the significant glacial advance and concludes that there must also have been significant increases in snowfall. The conditions on Svalbard during the Little Ice Age are still debated.

1.5 Description of Kongressvatnet

Kongressvatnet is an oligotrophic, meromctic lake, stabilized by sulfur-rich mineral springs entering from the northern shore of the lake (Bøyum and Kjensmo, 1970). Aerial photographs reveal a surface area of 0.51 km^2 during 1992. The maximum depth of the lake was 52m during the 2006 field season (Figure 1.7). However, a curious mass drainage event, likely due to subsurface karst outlets, occurred before the 2008 field season. This resulted in a lowering of the lake level to approximately 47-48m depth and a significant reduction in lake surface area. The lake is both thermally and chemically stratified and has a distinct summer thermocline at approximately 10m and a chemocline at approximately 44m depth (Figure 1.8). The pH of the lake is approximately 8.0 above the chemocline, dropping to 7.4 below. The Secchi disc transparency is 5.2 m, as measured upon the initial documentation of the lake during (Holm, T.M., personal communication, 2008). The lake is bordered to the North and Southeast

by mountains ranging from 450m to 675m in elevation, which shields it from winds from the dominant NE winds (Akerman, 1980).

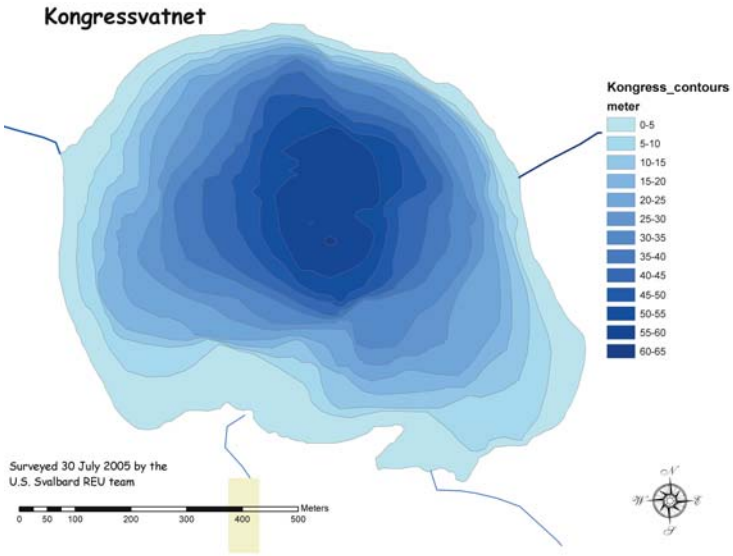

Figure 1.7. Bathometric map constructed by participants of the 2005 Svalbard-REU. Note that the lake level was significantly greater when the measurements were taken for the map than when samples were collected for the present study.

After the retreat of the late Weischelian Ice Sheet, isostatic rebound resulted in the elevation of the marine limit in Spitsbergen to approximately 65-78m above current sea level (Guilizzoni et al., 2006). Thus the lake's elevation (94 m) above this limit indicates no marine influence in Kongress (Guilizzoni et al., 2006). Kongressvatnet is eroded into the lower Permian Gipshulken Formation—a weak rock composed of dolomitic, bioclastic limestone—and is bordered to the east and west by ridges of more resistant rock units (Harland et al., 1997). The highlands to the east of the valley are composed of Middle to Upper Permain Kapp Starostin Formation, while the Permian to Carboniferous Nordenskoldbreen Formation, composed of sandstone, shale, and carbonates, forms the ridge to the west (Harland et al., 1997) (Figure 1.5). The lake may have initially formed as a karst sinkhole and thus contains a complicated subsurface drainage network (Werner, A., personal communication, 2008).

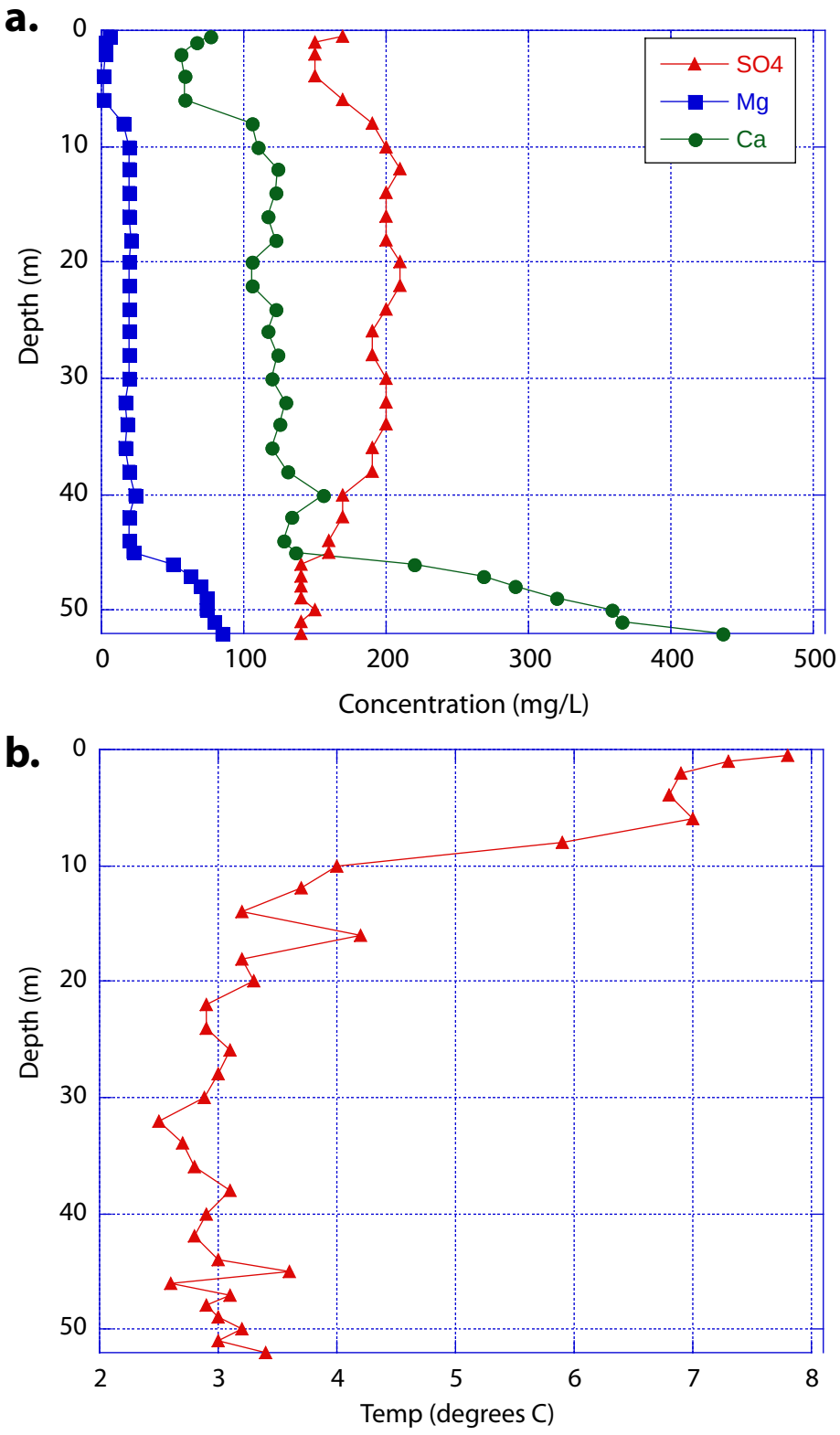

Figure 1.8. a. Magnesium, calcium and sulfate concentrations for Kongressvatnet. Note the sharp chemocline at approximately 44m depth. b. Temperature profile for Kongressvatnet illustrating the summer thermocline at approximately 10m depth. (Holm, T.M., Personal communication, 2006).

During periods of high lake level, Kongressvatnet drains subaerially through an outlet on the east side of the lake (Figure 1.9a). However, during the 2008 field season, low water levels prevented surface outflow. Previous studies have suggested that a subsurface drainage outlet exists approximately 15 m below the lake surface on the eastern side of Kongressvatnet, emerging as a spring approximately 11 km from the lake edge (Bøyum and Kjensmo, 1970). Several other springs that emerge to the Northwest of the lake, draining into Linnévatnet, have also been tentatively attributed to subsurface drainage from Kongressvatnet (Anderson, 2007).

Most of the water entering the lake originates from two distinctly different alluvial fans (Figure 1.9). The White Fan is covered by alluvial sediments derived from the carbonate Gipshuken Formation and is fed by meltwaters from permanent snowfields located on the southern hill in the upper part of the Strike Valley, a North-South trending valley in the western part of the catchment (Figure 1.10). The orientation of this v-shaped valley parallel to the strike of the bedrock strike suggests that it formed from differential erosion of two subunits within the Gipshuken Formation (Anderson, 2007) (Figure 1.10a).

Figure 1.9. Photograph of Kongressvatnet facing north overlooking the lake. The black arrows mark the position of the White Fan (left) and the Black Fan (right). Linnévatnet is in the top left corner of the image.

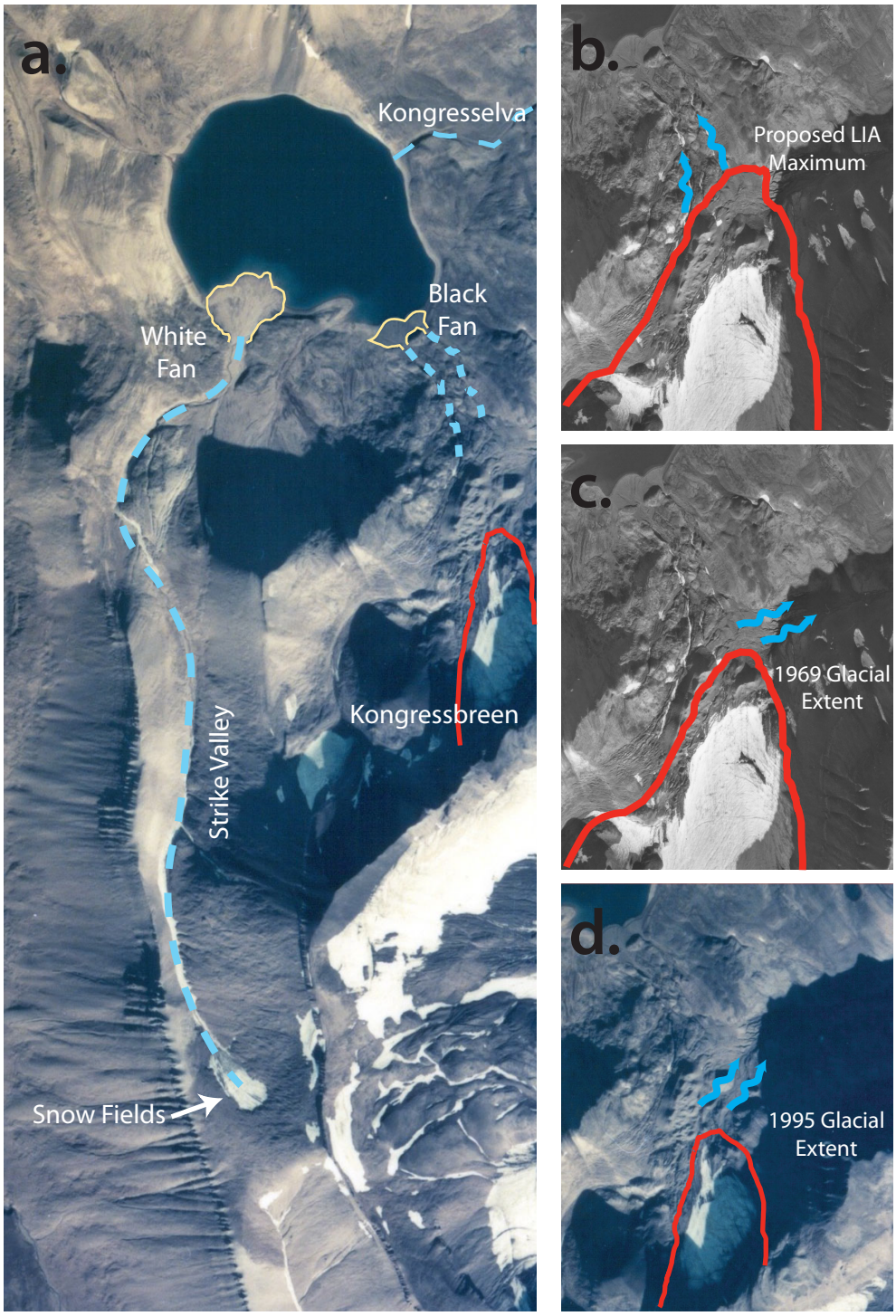

Figure 1.10. a. 1995 Norsk Polarinstuitt Aerial photograph of Kongressdalen highlighting the position of the White and Black Fans, Kongresselva, and Kongressbreen. b. 1969 aerial photograph with the proposed maximum glacial extent of Kongressbreen during the LIA when the glacier may have drained into the valley, forming the Black Fan (red line). c. 1969 glacial extent illustrating the redirection of water toward Grønfjord after the retreat of Kongressbreen. d. 1995 aerial photograph revealing continued retreat of Kongressbreen (modified from Anderson, 2007).

The Black Fan is located east of the White Fan and is composed of sediment derived from the Permian Kapp Starostin Formation. The Black Fan is positioned adjacent to the drainage divide between Kongressdalen and Grønfjord (Figure 1.10). Using aerial photograph observations, pebble counts, sediment texture, and lichenometric dating of till, a former Svalbard Research Experience for Undergraduates (REU) student, Leif Anderson (2007), determined that Kongressbreen is the most likely source of Black Fan sediment. Aerial photographs from just after the end of the Little Ice Age suggest that during that glacial maximum, Kongressbreen likely advanced to abut this topographic divide, allowing meltwater to transport Permian Kapp Starostin Fm. rocks that form the Black Fan (Figure 1.10b-d). Retreat of the glacier caused the outlet to the Black Fan to be abandoned as meltwater was redirected down valley toward Grønfjord (Figure 1.10c-d).

The only other inlet of water to the lake is the aforementioned sulfurous rivulet entering from the northwest. The low discharge and short flow path makes this an insignificant source of sediment (Anderson, 2007). Snowmelt flows from colluvial deposits located between the White and Black fans, but the sediment load of these small channels is also insignificant in comparison to that of the meltwater channels feeding the White Fan and the once active Black Fan (Anderson, 2007).

This shows that the White and Black Fans dominate the sediment inflow in Kongressvatnet and the provenance of lake sediments may be determined through accurate characterization of the two fans. Since the deposition of the Black Fan likely occurred during the LIA maximum glacial advance, the sediment record from Kongress should reflect the addition of this meltwater sediment and thereby constrain the age of the onset and termination of the Little Ice Age as well as provide information about activity prior to glacial retreat.

1.6 Previous Research on Kongressvatnet

Alden (2007) used loss on ignition (LOI) as a proxy for provenance. LOI measurements for the sediments of the fan and the core were collected after heating for 2.5 hours at 550° C to calculate weight loss due to organics. The results of these analyses indicate that the Black Fan may be characterized by high LOI (Alden, 2007). However, many factors influence LOI, including the high carbonate and clay content of the core sediments as well as the inflow of organic material into the lake. These multiple contributors indicate that LOI may not be an accurate proxy for sediment provenance.

Alden (2007) additionally used the carbonate index, as determined through XRD, as a proxy for provenance of sediments in Kongressvatnet. The carbonate index is a ratio that compares the total peak area of calcite and dolomite to all other minerals present (Leonard, 1986) (Equation 1.1).

$$CI = \frac{(dolomite + calcite)}{(quartz + dolomite + calcite)} \qquad (1.1)$$

However, the carbonate indices of the lake sediment are greater than either of the fans alone, forcing an interpretation based on the relative carbonate indices. Alden (2007) suggested that the elevated carbonate index in the lake sediments might reflect subsurface inflow through karst inlets, which introduces excess carbonate sediment, and prevents the use of CI as a provenance indicator (Alden, 2007).

Guillizzoni et al. (2006) conducted a multi-proxy analysis of Kongressvatnet lake cores including chemical analysis (Pressed Pellet XRF), mineralogy (XRD), diatom characterization, pigment analysis, and loss on ignition (LOI). This analysis revealed four distinct zones of chemical composition within core sediments and Guillizzoni et al. (2006) postulated that these changes reflect varying input from the White and Black Fans due to both glacial advance and

variations in the course of the streams feeding each fan. The problem with this study is that they failed to analyze any of the watershed material that contributed to the lake sediments.

1.7 Purpose of Study

This thesis will test two principle hypotheses as described below and a synthesis of these analyses will be used interpret late Holocene climate change in Western Spitsbergen, Svalbard.

I. *Changes in the chemistry and mineralogy of Kongressvatnet lake sediments reflect Late Holocene climate change in this region.*

The deposition of the Black Fan during the Little Ice Age provides the opportunity to interpret the onset and termination of the LIA in Svalbard. Therefore, this study aims to refine previous analyses of provenance in Kongressvantet, using elemental chemistry of surface and core sediments to characterize the White and Black Fans and differentiate the influence of these sources in the lake sediment.

The chemical analysis will further focus on the influence of lake chemistry and biogeochemical cycles on the observed core sediment chemistry. Due to the long residence time for the lake water and the presence of sulfate reducing bacteria, the lake's biogeochemical cycles respond to changes in climate through a series of feedback mechanisms. This section will focus on the influence of climate on water chemistry and how that will in turn affect the sediment chemistry via precipitation or dissolution.

II. *Mineral weathering products reflect the relative age of the surfaces of meltwater deposits.*

Multiple studies document the occurrence of chemical weathering in periglacial environments (e.g. Anderson et al., 1997; Egli et al., 2008; Drever and Hurcomb, 1986) and the utility of the resultant mineralogic changes in the interpretation of landscape evolution (Allen et

al., 2001). The Black Fan deposition history is addressed through a study of clay mineral weathering patterns across the fan. The amount of primary to secondary clay mineral alteration is used to interpret the relative surface ages.

2. METHODS

2.1 Field Methods

All samples were collected during July and August of 2008 with the Svalbard Research Experience for Students (REU), a National Science Foundation funded project. Three Cores were collected from Kongressvatnet: one from the deep basin at 49 m depth (DB-49), one from offshore of the White Fan from 43 m depth (WF-43), and one from offshore of the Black Fan at 31 m depth (BF-31) (Figure 2.1). Cores were dewatered at base camp before transport in their original sampling tubes to the United States.

A total of 48 samples of surface sediment were collected from the Kongressvatnet catchment. Collection sites were selected to include the finest material present in an attempt to mimic the sediment entering Kongressvatnet. Whenever possible, sediment was collected within or adjacent to active or previously active stream channels. Samples were collected at 15 sites on the Black Fan and 17 sites on the White Fan along both transverse and axial transects (Figure 2.1). At 2 of the Black Fan sampling locations, sediment was collected at the surface

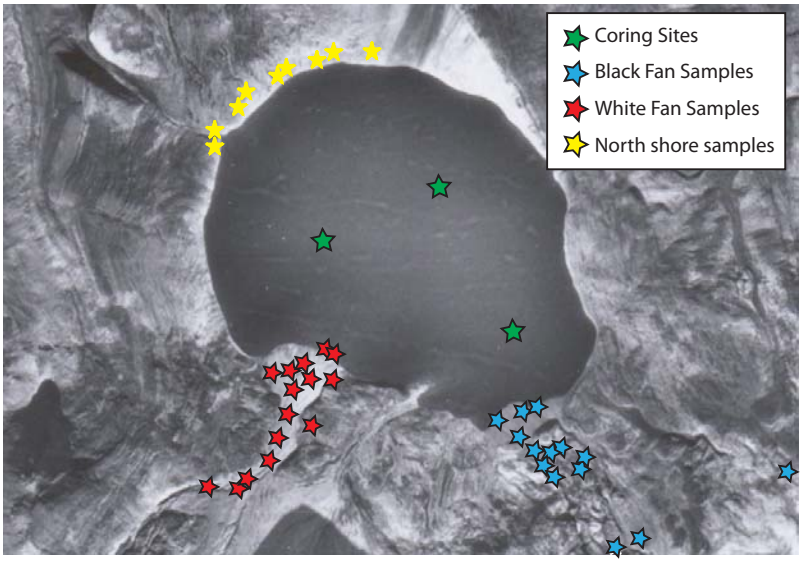

Figure 2.1. Location of sampling sites in Kongressdalen.

(approximately top 2 cm) and at 5-10 cm depth to examine possible weathering profiles. A sediment profile of 3 samples was collected at site BF002 at depths of 0-2 cm, 5-10 cm, and 10-15 cm. Samples were additionally collected from 9 locations along the northern slope bordering Kongressvatnet to verify the homogeneity of the Gipshuken Formation. Finally, rock samples were collected from the surface of both the White and Black Fans.

2.2 Laboratory Methods

2.2.1 ITRAX Scanning X-Ray Fluorescence Analysis of Core Sediments

2.2.1.a Core preparation

Cores were placed in a v-shaped cradle and the tubes were sliced using a small, mounted circular saw. After opposite sides of the tube walls were cut, core sediments were split using a taught piano wire. The surface of each core was cleaned using a razor blade before digital photographs were collected.

2.2.1.b Scanning XRF analysis

ITRAX scanning XRF is a non-destructive procedure that provides relative concentrations of elements in counts per second (cps) for the following elements: Al, Si, P, S, Cl, Ar, K, Ca, Ti, V, Cr, Mn, Fe, Ni, Cu, Zn, As, Rb, Sr, Y, Zr, and Pb. Prior to analysis, the surface of each core was cleaned with a glass slide and then covered in 1.5 μμm (15,240 Å) Chemplex spectro ultra-polyester film to prevent sediment desiccation. Cores were analyzed at the Large Lakes Observatory of the University of Minnesota, Duluth using the ITRAX X-Ray Fluorescence Core Scanner, manufactured by Cox Analytical Systems of Gotenburg, Sweden (Croudace et al., 2006; Brown et al., 2007). The cores were analyzed using a Molybdenum tube

at a voltage of 30 KV and a current of 20 mA. The deep basin core (DB-49) was analyzed at a 500 μm step size with a 50 second exposure time. The core collected from in front of the Black Fan was analyzed at a 0.2 cm (2,000 μm) step size at an exposure time of 50 seconds. The core collected from in front of the White Fan was analyzed at a 400 μm step size with a 50 second exposure time.

Digital X-Radiograph images for each core were additionally obtained at 500 μm resolution. These images reflect density changes on a grayscale with black representing the densest sections of the core. Since the ITRAX scanning XRF results are sensitive to changes in porosity and thus the sediment grain sizes, the core collected from the deep basin (DB-49) was selected as the focus of this study as it contains the least variation in grain size.

2.2.2 X-Ray Fluorescence Spectroscopy

2.2.2.a Surface sediment grain size separation

A total of 8 samples from the Black Fan, 6 samples from the White Fan, and 1 sample from the northern shore were prepared for analysis using X-Ray Fluorescence Spectroscopy (XRF). Samples were quartered to prevent preferential selection of grain sizes and the initial weights of the samples were recorded. Each sample was sieved through a -1.25 ϕ (2.38 mm mesh) sieve and the masses of the two grain size factions were recorded. A portion of the <2.38 mm grain size faction was separated for bulk analyses of fan sediments. This sample was powdered using a tungsten carbide shatterbox to homogenize the sediment prior to making the fused glass discs and pressed pellets for XRF analysis.

Samples for elemental analysis of the <63 μm grain size fraction were obtained through wet filtration of the <2.38 mm sediments. The samples were added to distilled water and

suspended using the Fischer 550 Sonic Dismembrator for approximately one minute. The sample was filtered through a 4.0 ϕ and a 1 ϕ sieve, placed over a large aluminum funnel to separate out the <63 μm grain size faction. Distilled water was used to wash the sample through the sieves. Filtrate was collected and acidified with 2-3 drops of concentrated hydrochloric acid per 500 ml of solution. The acidified samples were centrifuged at 15000 rpm for 15 min, until flocculated. The water was decanted and the sample was placed in the oven at 60 °C until dry (2-3 hours). The dry samples were then ground with an agate mortar and pestle before prepped for XRF analysis.

For collection of the <1 μm grain size faction for both fans, samples were initially suspended in solution using the Fischer 550 Sonic dismembrator. Based on Stoke's law of settling, the <1 μm grain size faction was separated through centrifuging at 1500 rpm for 5 min 40 sec. The resulting suspension was decanted and 2-3 drops of concentrated hydrochloric acid were added for every 500 ml of water. The flocculated clays were then centrifuged at 2000 rpm for 10-15 min to compact the sediment for collection. The water was decanted and the remaining <1 μm material was placed in the oven to dry overnight at 50-60 °C.

2.2.2.b Sub-sampling of core sediment

Regions displaying the highest and lowest values of calcium and silica based on the ITRAX scanning XRF results were additionally sub-sampled for elemental analysis using the fused glass disc and pressed powdered pellet XRF methods. Three samples were collected from high calcium, low silica regions of the deep basin core (30-40mm, 99-111mm, and 195-211mm) and two samples were collected from low calcium, high silica sections of the deep basin core (0-22mm and 383-400mm). One sample was collected from a low calcium, high silica region of the

White Fan core (213-238mm). Samples were dried overnight in the oven (~60 °C) and crushed using an agate mortar and pestle.

2.2.2.c Major element analysis

X-Ray Fluorescence Spectroscopy using the fused glass disc method provides elemental content in percent composition by weight for the following oxides: SiO_2, TiO_2, Al_2O_3, Fe_2O_3, MnO, MgO, CaO, Na_2O, K_2O, and P_2O_5. Fused glass discs were prepared using methods adapted by Norrish and Hutton (1969). Approximately 1.3 g of each powdered sample (<2.38 mm and <63 μm) was weighed and ignited to 1,020 °C for at least 8 hours (Black Fan samples were heated at approximately 875 °C for at least 8 hours due to the high silica content) to drive off organic material, reduce carbonates, and oxidize iron.

After each sample was removed from the oven it was re-ground using an agate mortar and pestle. Each of the ignited samples (0.3000±0.0003 g) was mixed with 1.6073±0.0002 g of a flux composed of 47% lithium tetraborate ($Li_2B_4O_7$), 36.7% Lithium metaborate ($LiBO_2$) and 16.3% Lananthum oxide (La_2O_3). Before weighing the flux was dried in the oven for approximately 8 hours at 500 °C and then cooled for approximately 1 hour. Two replicates of each sample were prepared for analysis.

Samples were then placed in a platinum crucible and melted in the furnace at 1,040 °C for six minutes. After two minutes and again after four minutes, the sample was removed and swirled to ensure a homogenous mixture of sample and flux. After the material was molten, it was poured into a brass and carbon mold that was heated on a hotplate to 232 °C. Each sample was then quickly pressed into a thin glass disc using an aluminum plunger. The discs were slowly cooled overnight on the unplugged hotplate.

After the fused glass cooled, the edges of each disc were filed and the disc was cleaned with acetone. The samples were analyzed using a Siemens MRS-400 multi-channel X-ray spectrometer using the USGS basalt standard, BHVO-1, and granite standard, G-2 (USGS online) (analytical methods adapted from Norrish and Hutton, 1969).

2.2.2.d Trace element analysis

X-Ray Fluorescence Spectroscopy using the pressed pellet method provides elemental content in parts per million (ppm) for the following elements: Nb, Zr, Y, Sr, U, Rb, Th, Pb, Ga, Zn, Ni, Cr, V, Ce, Ba, and La. To prepare the pressed pellets, approximately 10 g of each powdered sample was weighed and mixed with 13-15 drops of polyvinyl alcohol binder (20 g Poly vinyl alcohol per 1 L of deionized water) and then pressed into pellets under approximately 6,000 T of pressure. Pressed pellets were dried overnight at 60 °C. Pressed powder discs were analyzed on a PW2400 sequential spectrometer. Errors due to interference, non-linear background, and mass absorption coefficient variations were corrected for using methods adapted from Norrish and Chapel (1967).

2.2.3 X-Ray Diffractometry of Surface Sediments

The same surface and core samples that were analyzed using X-Ray Fluorescence Spectroscopy were also analyzed using X-Ray Diffractometry (8 samples from the Black Fan, 6 samples from the White Fan, 1 sample from the northern shore, and 5 core samples).

2.2.3.a Clay extraction from rock samples

Clay material (<1 μm) was extracted from the White Fan rocks via removal of carbonates using a 1 N sodium acetate (NaOAc) buffer of pH 5 as described by Jackson (1969). The buffer was prepared by mixing NaOAc (82.03 g) with glacial acetic acid (HOAc) (27 ml). Deionized water was added to the mixture to make 1 L of the buffer solution. Enough buffer was added to cover the crushed White Fan rock material, and the mixture was stirred into suspension and then placed in a near-boiling water bath (approximately 90 °C) for at least 30 min, with occasional stirring. The resulting suspension was decanted and then centrifuged to flocculate the suspended material. After the suspended material flocculated, the buffer was decanted and distilled water was added to the remaining material. The material was then suspended using the Fischer 550 Sonic dismembrator (at least 2 min) before centrifuging for 6 min at a minimum of 1500 rpm. If the material completely flocculated, the water was decanted and fresh distilled water was added. The solution was again placed under ultrasound and centrifuged. This process was repeated until the material remained in suspension. Once this occurred, the material was re-suspended using ultrasound for approximately one minute and the <1 μm grain size faction was collected by centrifuging at 1500 rpm for 5 min and 40 sec.

Clay material from the Black Fan rocks was collected for XRD analysis by crushing the rock using the Braun Chipmunk VD67 rock crusher. The crushed rock material was mixed with deionized water and the sediments were suspended using ultrasound.

2.2.3.b Oriented slide preparation

Oriented clay mineral mounts were prepared based on methods described by Moore and Reynolds (1997) and Velde (1992). Distilled water was added to each surface sediment sample

(<2.38 mm) and core samples; the fine material was suspended using the Fischer 550 Sonic dismembrator for approximately one minute. The resulting suspension was decanted into a centrifuge bottle and more distilled water was added. The sample was again suspended in water using ultrasound. This process was repeated until centrifuge bottle was full (about three times). Based on Stoke's law of settling, the combined decanted fluid was centrifuged at 1500 rpm for 5 min and 40 sec to separate the grains smaller than 1 μm.

The <1 μm grain size faction of the suspension was decanted and suction filtered through a 0.45 μm Millipore filter. Suction filtration was terminated before all liquid passed through the filter to prevent alteration of clay mineral orientation. Remaining liquid was poured out from the top of the funnel. Each filter was placed upside down on a glass slide and heated in the oven at 40^{o} C for approximately a minute, until the surface of the slide appeared damp but not wet. Once removed from the oven, the filter was peeled of rapidly and the clay minerals remained on the glass slide.

After preparation of the slides, suspensions of <1μm material of select samples were saturated with potassium and magnesium. 2-3 drops of concentrated hydrochloric acid was added to each clay suspension to be saturated. The sample was then centrifuged at approximately 2000 rpm for 10-15 min until the clay flocculated. The water was decanted and a pea-sized amount of the flocculated material was placed into a 10 ml test tube, which was then filled with 1N KCl or MgCl. Clay samples were disaggregated in an ultrasonic water bath before shaken on the shaker table for at least 4 hours. The test tubes were centrifuged and the resulting liquid was decanted. Deionized water was added to each test tube, which was shaken by hand and then centrifuged for approximately 30 sec. If the material flocculated, the solution was decanted and fresh deionized water was added. This process was repeated until the clay

remained suspended after centrifuging to ensure complete removal of excess chloride ions (methods adapted from Moore and Reynolds, 1997). Oriented clay mineral aggregates were subsequently prepared using suction filtration (see above).

2.2.3.c Oriented powder mount preparation

Samples of less than 1 μm material of the surface sediment (extraction methods described in section 2.2.1.1) were prepared in oriented powder mounts for analysis of the 060 reflections using side-loading mounts as described by Moore and Reynolds (1997). The upper edge of a plastic powder mount was sliced to extend the reservoir to the edge of the mount. The back of a second slide was placed against the reservoir and secured using a screw clamp. A piece of weigh paper was secured around the top of the holder to prevent loss of sample during loading. The sample holder was then placed on a vibrating surface (a fish tank air-pump was used) as the less than1 μm material was loaded, occasionally tapping the apparatus on the counter, to tightly pack the oriented sediments in the holder.

2.2.3.d X-Ray Diffractometry analysis

All samples were analyzed using copper Kα radiation on the Scintag XRD 2000. Oriented glass slides were analyzed from 2° 2θ to 32° 2θ at a rate of 1° per minute and powder mounts were analyzed from 55° 2θ to 65° 2θ at a rate of 1° per minute. Oriented glass slides were initially analyzed under air dried conditions and then placed in a desiccator containing a layer of ethylene glycol for at least one day before reanalysis. Each sample was then heated to 375° C for 1 hour to drive off structural water and then reanalyzed. The samples were again heated to 550 °C for one hour to collapse remaining clay structures before reanalysis. Samples

saturated with magnesium were analyzed under air dry and glycerol saturated conditions (Moore and Reynolds, 1997; Bergaya et al., 2006).

2.2.4 Magnetic susceptibility

Magnetic susceptibility of the deep basin core was analyzed at 1 cm increments using the Barrington MS2 Magnetic Susceptibility meter and the MS2E1 high-resolution surface-scanning sensor. The machine was corrected for drift after every third or fifth analysis and subsequently re-zeroed. The data was collected and analyzed using the MULTISUS21 software.

2.2.5 Scanning Electron Microscope (SEM) and Electron Dispersive Spectroscopy (EDS)

Three samples were prepared for Scanning Electron Microscope analysis (SEM) from depths of 10-50 mm, 122-173 mm, and 450-500 mm. Each sample was collected from the deep basin core using a mold composed of a small rectangular box of thin aluminum approximately 1 mm to 2 mm deep. This apparatus was then placed edge-down into the core surface and a thin wire was used to slice underneath the edges of the mold. Then the entire unit was removed from the core. The samples were dried overnight and subsequently heated to approximately 70 °C to drive off any residual moisture. After drying, the samples fractured along bedding planes. In addition to analysis of the sediments in the aluminum holders, two pieces of the bedding planes from approximately 40-50 mm depth were mounted on stubs. All samples were coated with Pd-Au using the Technics Sputter Coater. The samples were analyzed on the JOEL JMS-6400 Scanning Electron Microscope (SEM). Energy Dispersive Spectroscopy (EDS) was used to analyze the elemental composition of the sediment.

3. RESULTS

3.1 X-Ray Diffractometry

The characteristics that define vermiculite are broad (Moore and Reynolds, 1997). Thus for the purpose of this analysis, vermiculite is operationally defined as a trioctahedral mineral resembling talc with negligible expansion upon ethylene glycol solvation, yet uptakes a single layer of glycerol after magnesium saturation and subsequent glycerol saturation, evident in a shift of the 001 vermiculite reflection from 14 Å in the Mg-saturated samples to 14.5 Å after glycerol saturation. Heating to 375 °C for 1 hour causes this peak to collapses to 10 Å (Moore and Reynolds, 1997).

For the purpose of this analysis, smectite is defined as a dioctahedral clay that expands upon ethylene glycol solvation to approximately 17 Å and expands to 18 Å with magnesium saturation and subsequent glycerol saturation. The smectite 001 reflection collapses to 10 Å upon potassium saturation and low temperature heat treatments (Reynolds and Moore, 1997).

3.1.1 X-Ray Diffraction of Black Fan clays

XRD spectra of the Black Fan clays (<1 μm) collected from newly exposed surfaces within meltwater channels display an intense, asymmetric peak at 10.2 Å (8.7° 2θ), a medium to low intensity peak at 5.0 Å (17.8° 2θ), and a medium to low intensity peak at 3.3 Å (26.7° 2θ), the positions of which are unaffected by ethylene glycol saturation, potassium saturation, magnesium and glycerol saturation, or heating for 1 hour to 550 °C (Figure 3.1, 3.2). Stability during heating and saturation of this series, 10 Å, 5 Å, and 3.3 Å, indicates the presence of illite (Moore and Reynolds, 1997).

Figure 3.1. Photograph of the Black Fan facing southeast. The "fresh" sediments were collected from the channels leading to the fan (arrows), while the "altered" samples were collected from the debris flow lobes between the two primary channels.

Diffractograms of the unaltered sediments also reveal a low intensity peak at an average of 14.2 Å (6.2° 2θ) that broadens and slightly shifts to approximately 5.9° 2θ (15.1 Å) upon ethylene glycol solvation. The slight expandability of the peak at 14 Å in the air dried Black Fan samples indicates the presence of a smectite or vermiculite-like clay (Figure 3.2).

Upon heating to 375 °C, the 14 Å peak collapses to ~10 Å. Magnesium and glycerol saturation does not affect the peak position, yet potassium saturation results in collapse of the 001 reflection to ~10 Å, a habit common to high charge vermiculite (Figure 3.2b) (Moore and Reynolds, 1997). Magnesium saturation additionally resolves the vermiculite 003 reflection at an average of 4.7 Å (18.7° 2θ), which is masked in the air-dried samples by the 5 Å illite reflection (002). Thus, after magnesium saturation a rational series of vermiculite reflections occurs at approximately 14.1 Å, 7.1 Å, 4.7 Å, and 3.5 Å (Moore and Reynolds, 1997) (Figure 3.2b).

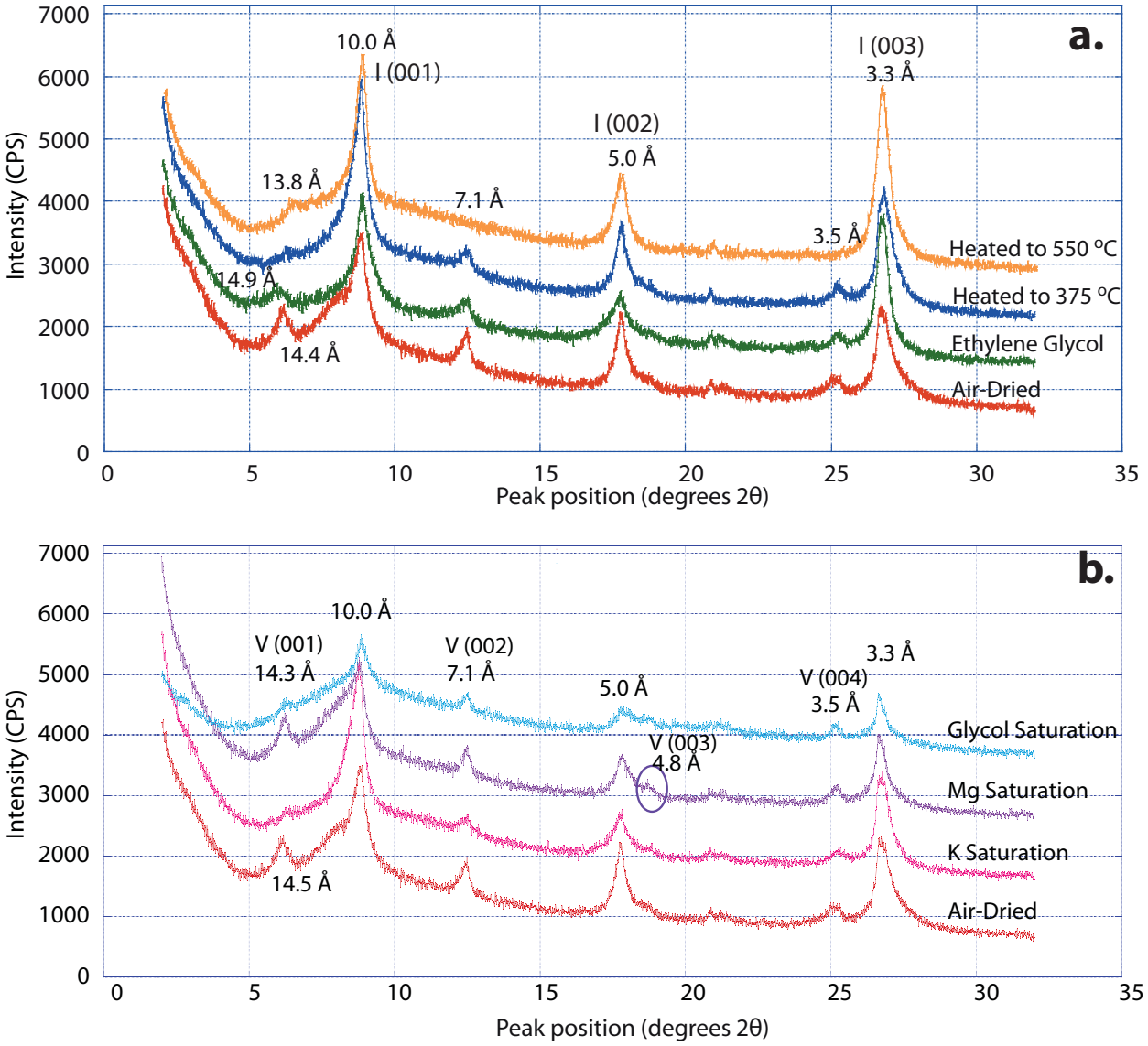

Figure 3.2. X-Ray Diffraction pattern for an oriented clay mount of sample BF006 under six different treatments, representing the typical unaltered sediment from within the meltwater channels leading to Black Fan or across the fan surface. Positions of primary peaks are labeled in angstroms (I = illite; V = vermiculite).

After ethylene glycol solvation and low temperature heating, a remnant peak is evident at ~14Å that intensifies upon heating to 550 °C, a habit common to chlorite (Moore and Reynolds, 1997) (Figure 3.2). The presence of this remnant peak suggests chloritization of the vermiculite. Chlorite is a 2:1 trioctahedral clay that contains layers brucite [$Mg_3(OH)_6$] between each 2:1

layer (Velde, 1992). Chlorite is similar in structure to vermiculite and the distinction between these classes of clays is not well defined (Moore and Reynolds, 1997).

The peak at 10 Å in the air-dried samples is slightly asymmetric, but becomes more symmetric with ethylene glycol solvation. This behavior is common to illite and vermiculite mixed-layer clays since the slight expansion of vermiculite layers with ethylene glycol solvation reduces the asymmetry of the ~10 Å peak (Moore and Reynolds, 1997) (Figure 3.2a). Analysis of powder mounts of the <1 μm material, oriented with a vertical c axis, further supports the presence of both discreet vermiculite and mixed layer vermiculite/illite in strong 060 reflections at 1.54 Å (59.97° 2θ) and 1.50Å (61.73° 2θ) respectively (Moore and Reynolds, 1997) (Figure 3.3).

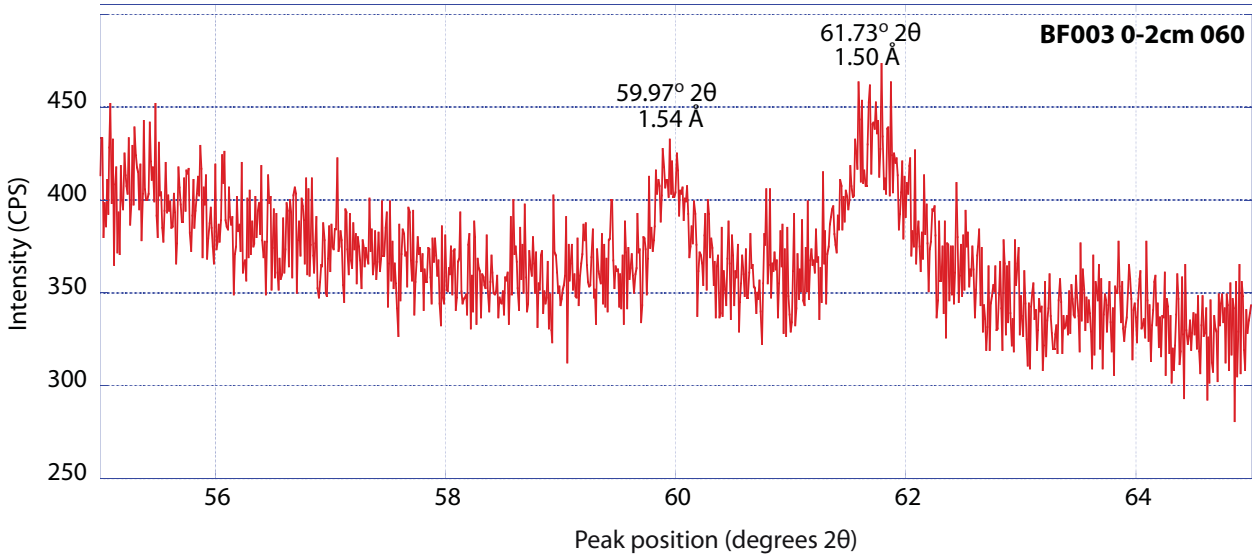

Figure 3.3: X-Ray Diffraction pattern for a powder mount of <1 μm material (BF003) with the c-axis oriented vertically to determine the position of the 060 reflection. This sample was collected between 0-2 mm of the raised debris flow lobes on the southeastern slope of Kongressdalen.

The relative intensities of the mixed layer illite/vermiculite 001 reflection (10 Å) compared to the discreet chloritized vermiculite 001 peak (14 Å) vary considerably between samples (Figure 3.2, 3.4). The illite 001 reflection (10 Å) dominates over vermiculite (14 Å) in the samples collected across the fan surface and within the meltwater channels leading to the fan (BF006, BF012, BF016) (Figure 3.2). The clays extracted from the Black Fan rock samples have little to no 14 Å peak, indicating that the samples are primarily composed of interstratified illite/vermiculite (Figure 3.5). Conversely, the opposite trend occurs in the samples collected from the upper surfaces of debris flow lobes (BF003 0-2 cm, BF002 0-2 cm) (Figure 3.4).

Diffractograms of BF002 sediments collected from 5-10 cm and 10-15 cm depth reveal the formation of an additional broad peak centered at approximately 11 Å (Figure 3.6). This peak is more intense in the sample from 5-10 cm depth than at 10-15 cm, yet is nearly destroyed in the surface sediment samples (0-2 cm) (Figure 3.6). Similar to hydro-biotite, the formation of this peak indicates regular interstratification of nearly equal amounts of vermiculite and illite, resulting in an intermediate reflection between illite 001 (10 Å) and vermiculite 001 (14 Å) (Moore and Reynolds, 1997).

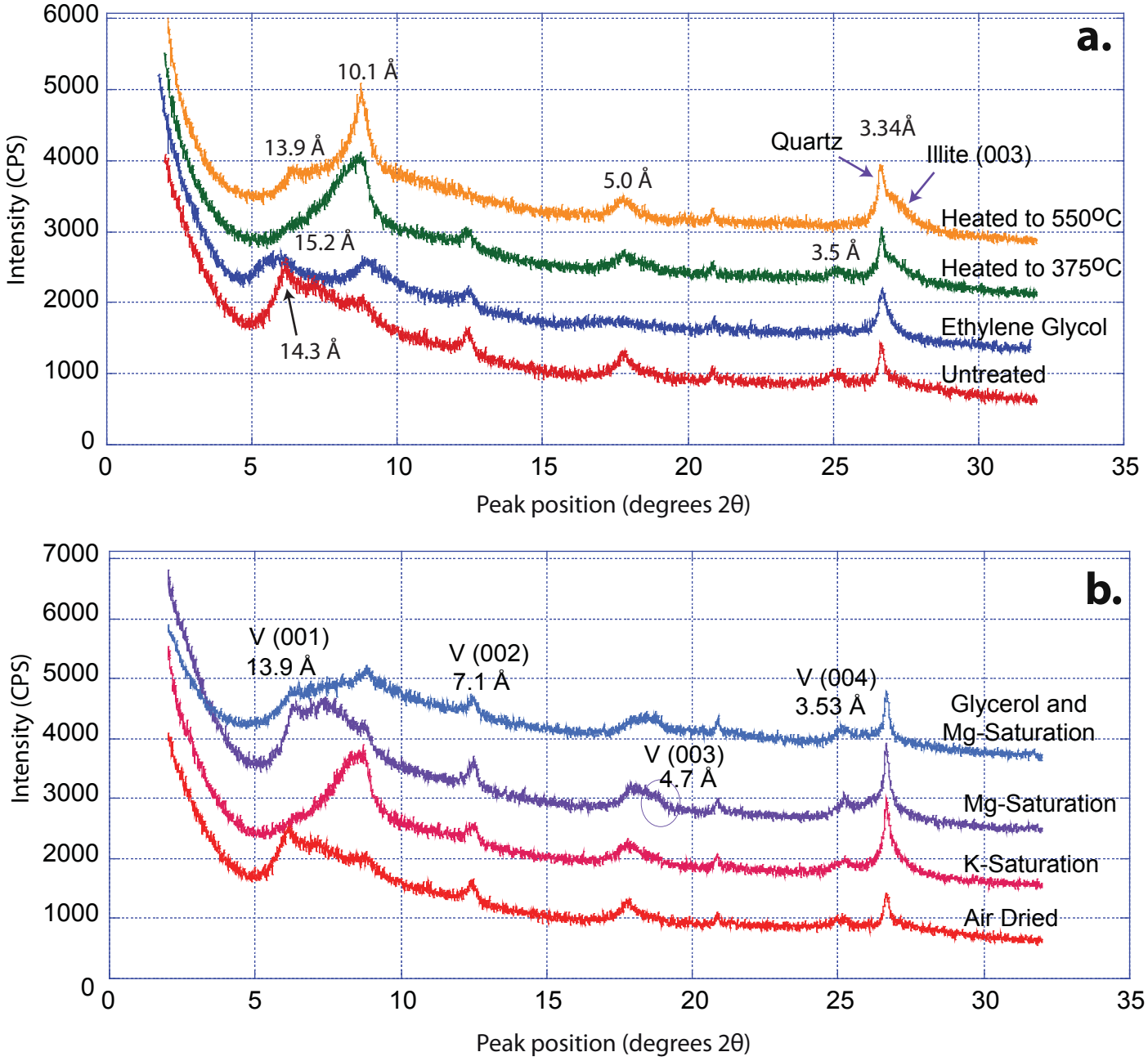

Figure 3.4. X-Ray Diffraction pattern for an oriented clay mount of sample BF003 0-2 cm under the six treatments used to identify the clay minerals. This sample is representative of the material collected from the upper 2 cm of the debris flow lobes on the southeastern slope of Kongressdalen.

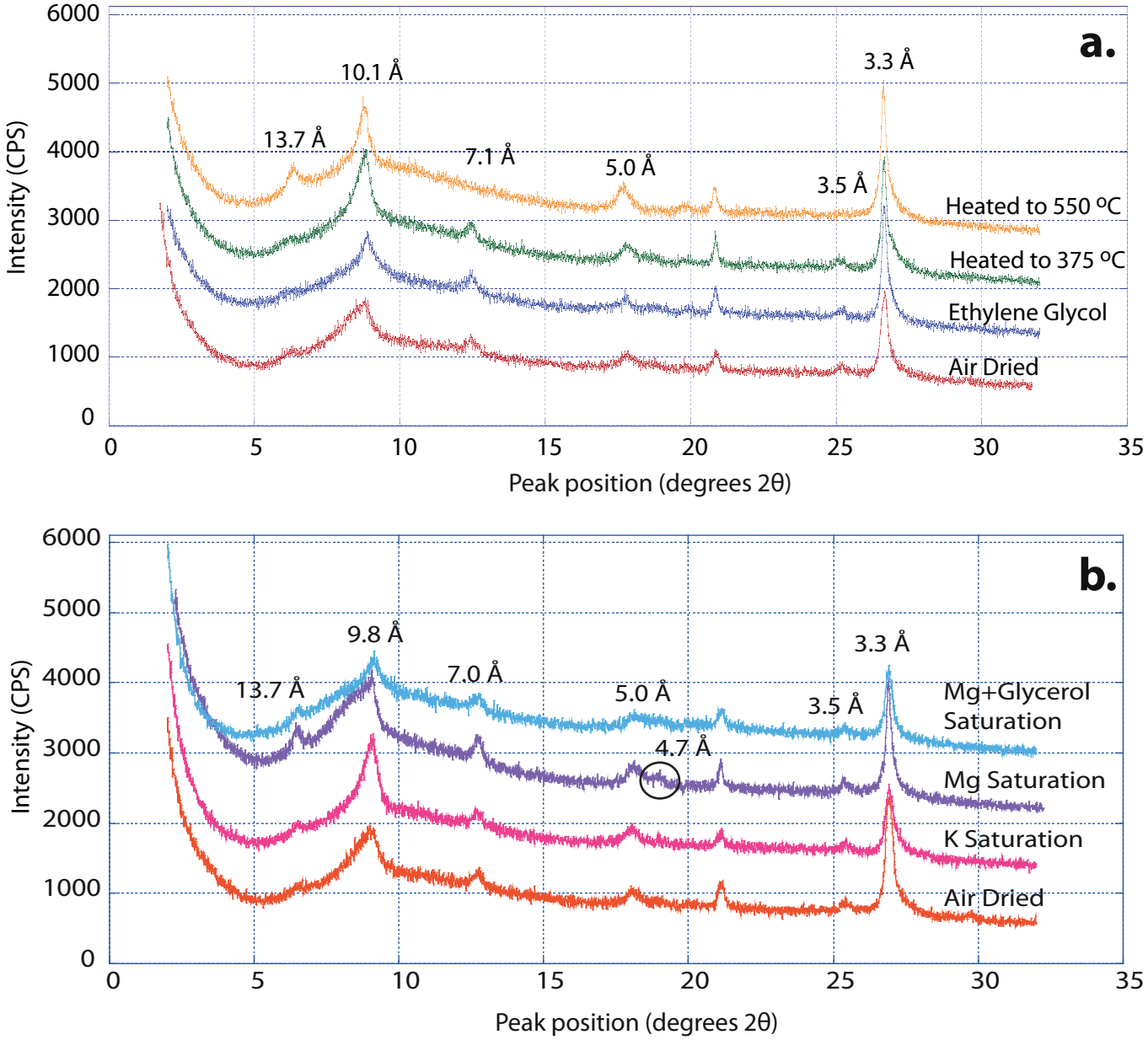

Figure 3.5. Diffractograms of an oriented clay mount for clays extracted from the Kapp Starostin Formation rocks collected from the surface of the Black Fan.

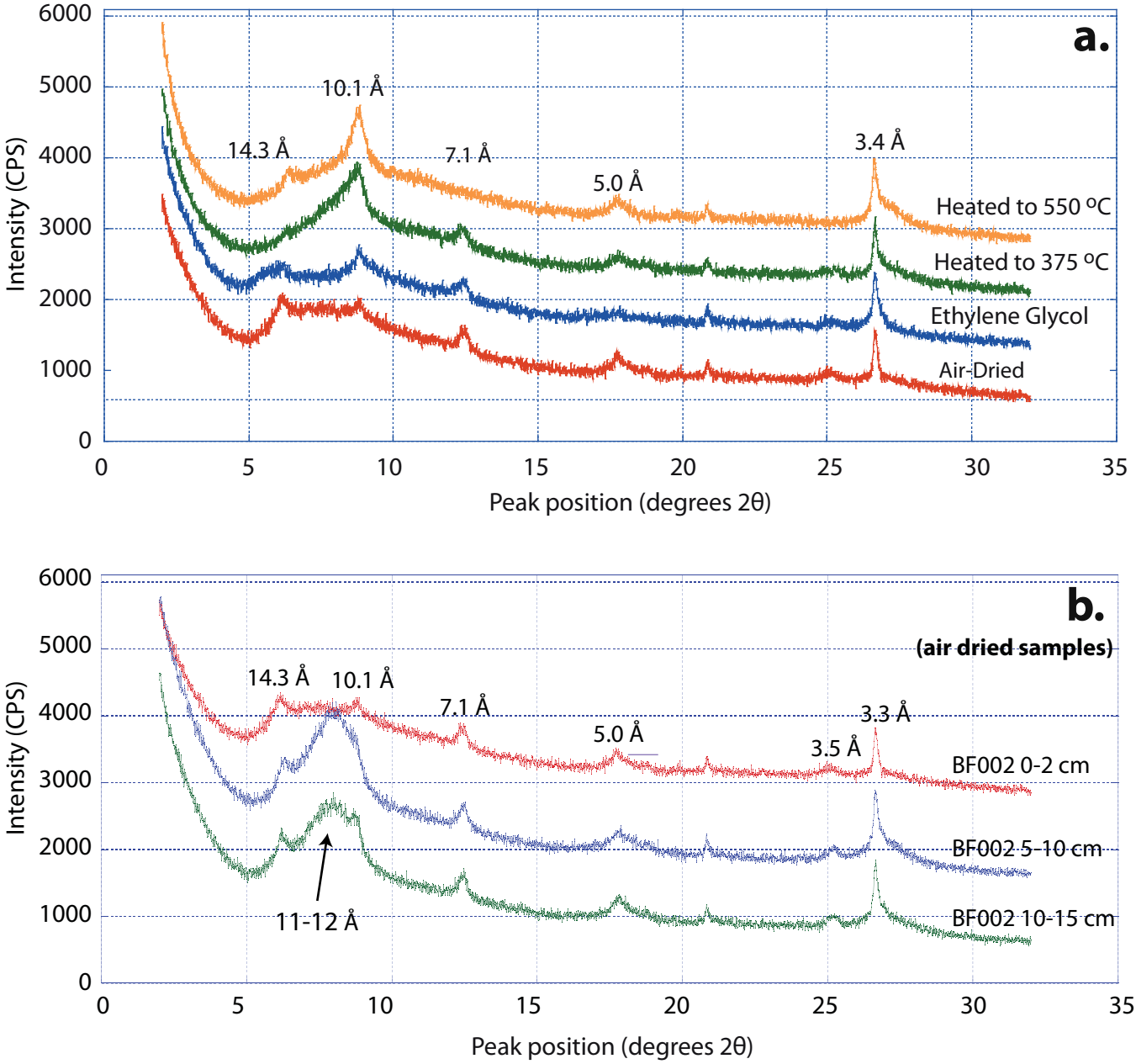

Figure 3.6. Diffractogram for an oriented clay mount of sample BF002, collected from vegetated debris flow lobes. a. Behavior of the clay under 3 different treatments used to identify the clay minerals. b. X-ray patterns for BF002 samples collected at 0-2 cm (red), 5-10 cm (blue), and 10-15 cm (green) depth. Note the ~11-12 Å peak at 5-10 cm and 10-15 cm depth not apparent in the other samples analyzed.

3.1.2 X-Ray Diffraction of White Fan clays

X-ray diffraction analysis of air-dried White Fan samples reveals a series of peaks at 10.1 Å (8.8° 2θ), 5.0 Å (17.9° 2θ), and 3.3 Å (26.84° 2θ) the positions of which are unaffected by ethylene glycol solvation or heating to 550° C (Figure 3.7). As in the Black Fan clays, the stability of this group of peaks (10 Å, 5 Å, and 3.3 Å) during heating and saturation is characteristic of illite (Moore and Reynolds, 1997).

The x-ray diffraction patterns also reveal a peak of equal intensity to the illite 001 reflection (10 Å) located at an average position of 14.4 Å (6.2° 2θ). This peak shifts to approximately 16.4 Å (5.4° 2θ) upon ethylene glycol solvation, a characteristic common to smectite (Moore and Reynolds, 1997) (Figure 3.7**)**. After heating to 375 °C for 1 hour the 16 Å peak collapses back to 10 Å; only a remnant peak remains at ~14 Å, which is diminished upon ignition to 550 °C (Figure 3.1). Potassium saturation causes this phase to collapse to ~10 Å (Figure 3.2).

Magnesium and subsequent glycerol saturation resolves two peaks: a minor peak at 14.34 Å and a medium intensity peak centered at 18.0 Å. The separation of these two peaks suggests the presence of both vermiculite (14.3 Å) and smectite (18.0 Å) (Figure 3.7b). Magnesium saturation additionally resolves a high-angle shoulder on the ~5 Å peak at 4.7 Å (18.7° 2θ), suggestive of the 003 reflection from vermiculite. Two very low intensity peaks at approximately 7.1 Å (12.4° 2θ) and 3.6 Å (25.0° 2θ) are unaffected by ethylene glycol solvation and heating to 375 °C, yet destroyed upon heating to 550 °C. These peaks likely represent the 002 and 004 reflections from vermiculite (Moore and Reynolds, 1997) (Figure 3.7b). Similar to the Black Fan clays, the illite 001 reflection (10 Å) is slightly asymmetric, which is diminished with

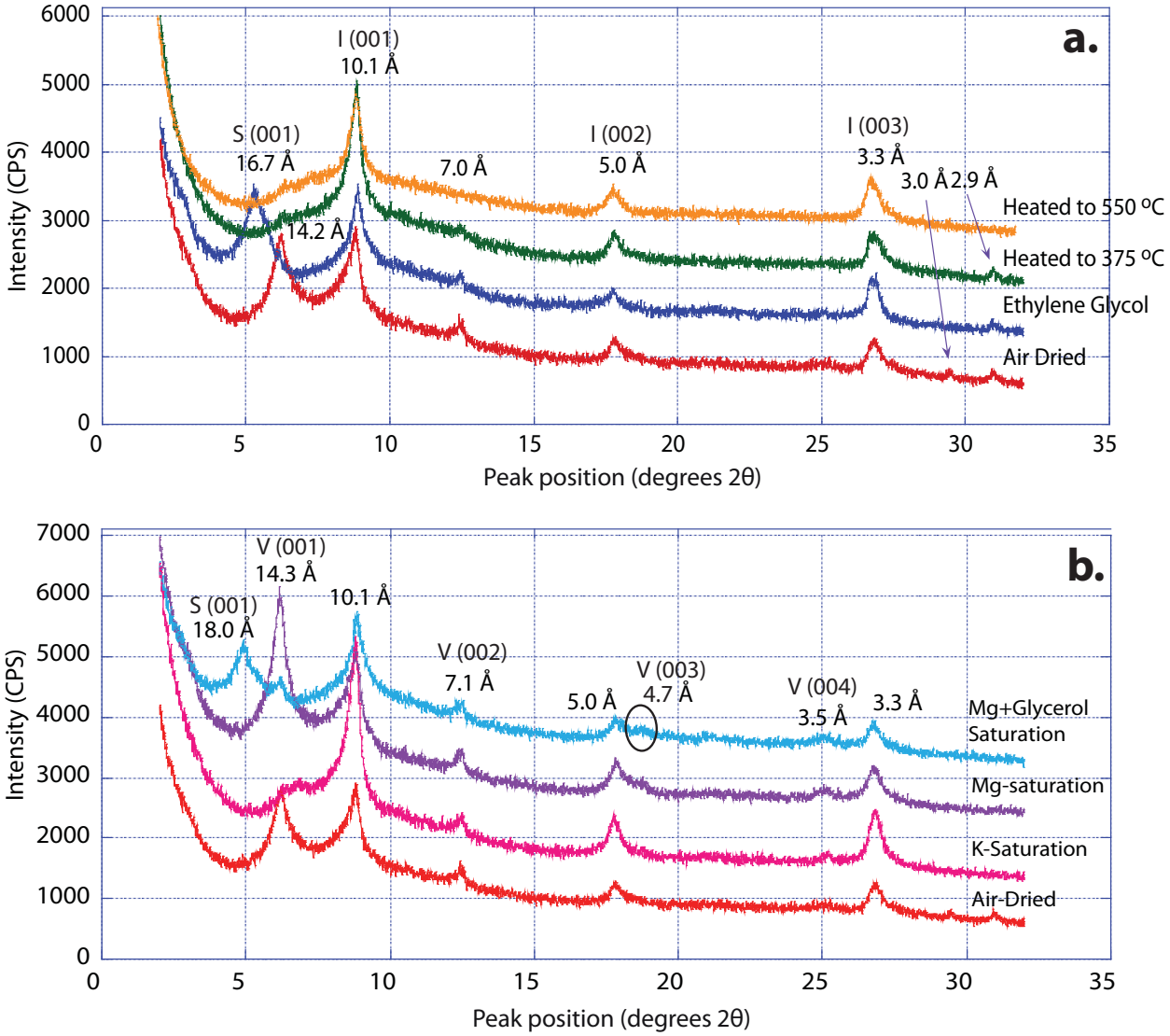

Figure 3.7. X-Ray Diffraction patterns of oriented clay mounts for a representative sample of White Fan clays collected from the fan surface. The six treatments used to characterize the mineralogy are displayed in a. and b. Peak positions are labeled in angstroms (I = illite, V = vermiculite, S = smectite).

ethylene glycol solvation, suggesting that the vermiculite originates in part in a mixed-layered illite/vermiculite. However, some discreet vermiculite may also be present in the White Fan clays. Powder mounts of the <1 µm material oriented with the c axis vertical, reveals a strong 060 reflection located at 61.70° 2θ (1.50Å), which may reflect the presence of both the mixed layer illite/vermiculite and smectite (Moore and Reynolds, 1997) (Figure 3.8).

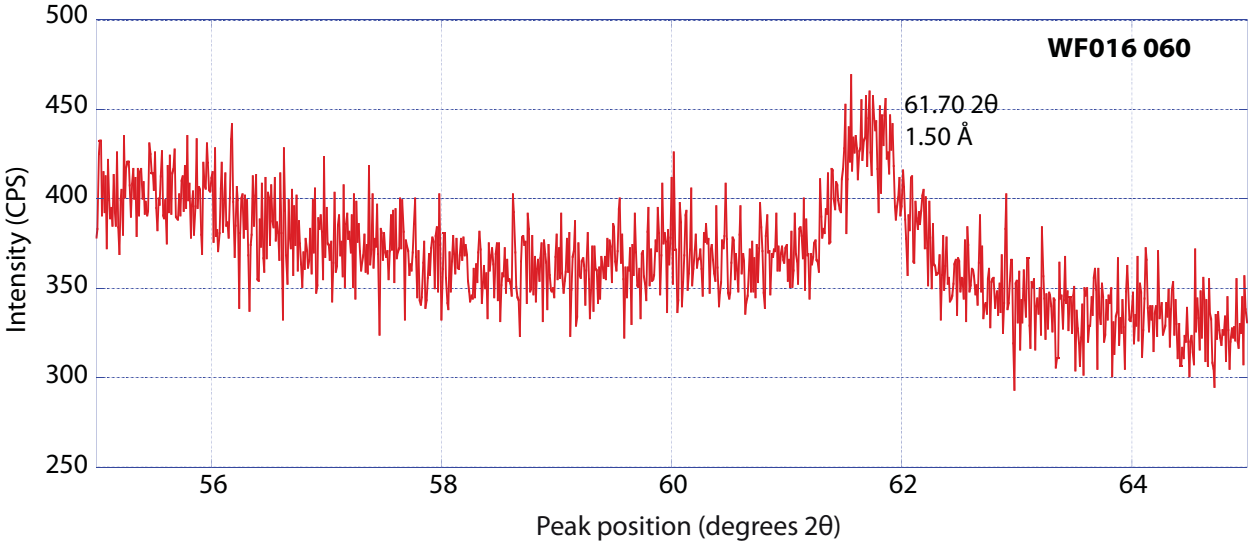

Figure 3.8. X-Ray Diffraction pattern for a powder mount of <1 µm material (WF016) with the c-axis oriented vertically to determine position of the 060 reflection. This sample was collected just offshore of the White fan at ~ 0.5 m depth.

X-ray diffraction patterns of the clays extracted from the White Fan rock material display similar patterns to the clay collected from the fan surface with peaks located at 14.2 Å, 10.1 Å, 5.0 Å, and 3.3 Å in the air dried samples (Figure 3.9a). However, the clays extracted from the White Fan rocks have significantly diminished ~14 Å reflections. The 14 Å peak becomes diffuse with negligible intensity after ethylene glycol solvation. Potassium saturation collapses this peak to ~10 Å, yet no change in position occurs after magnesium and subsequent glycerol saturation of samples, indicating the presence of vermiculite (Moore and Reynolds, 1997) (Figure 3.9b). The broadness and low intensity of vermiculite 001, and the asymmetry of illite 001 indicates illite/vermiculite interlayering, rather than discreet clay minerals (Figure 3.9b).

A low-intensity, sharp peak at 2.9 Å (31° 2θ) indicates the presence of dolomite. Although apparent in both the surface sediment and clays extracted from the White Fan rocks, it is most pronounced in the extracted clays from the rock (Figure 3.9).

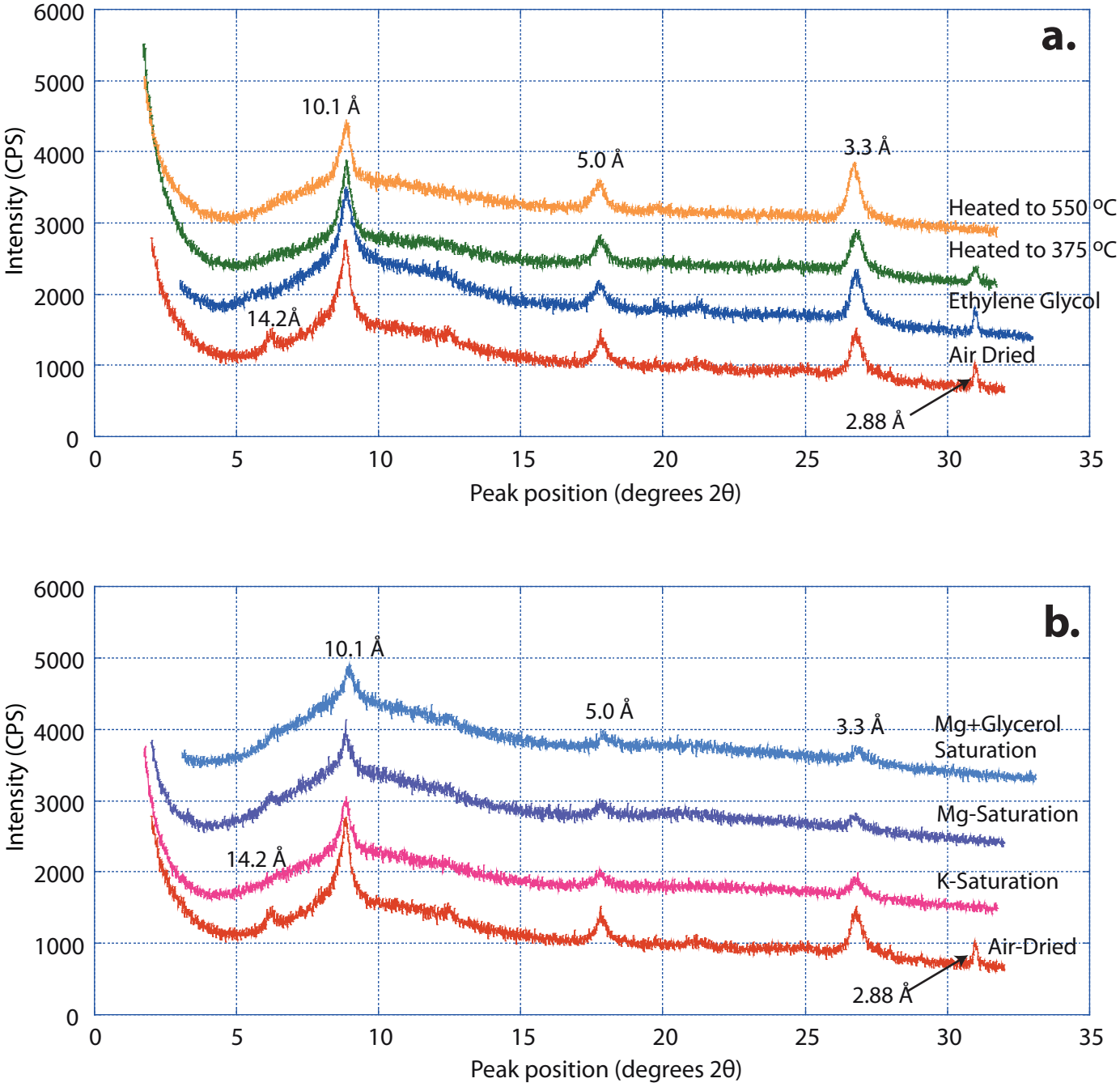

Figure 3.9: Diffractograms of an oriented clay mount for clays extracted from the Gipshuken Formation rocks that were collected from the surface of the White Fan. The six treatments used to characterize the mineralogy are displayed in a. and b.

3.1.3 X-Ray Diffraction of core clays

Five samples of clay from the deep basin core (DB-49) collected at depths of 0-22 mm, 30-40 mm, 99-111 mm, 195-211 mm, and 383-400 mm were analyzed using X-Ray Diffractometry. Similar to the surface sediments, analysis of the core clays reveals three peaks unaffected by ethylene glycol saturation, magnesium and glycerol saturation, or heating to 550 °C for 1 hour, positioned at average values of 9.7 Å, 4.9 Å, 3.3 Å. These peaks indicate the presence of illite (Moore and Reynolds, 1997) (Figure 3.10).

With the exception of the sample collected between 0-22 mm, the core clay samples display a peak positioned at 13.2 Å in air-dried samples, with nearly equivalent intensity to illite 001 reflection (10 Å). Upon ethylene glycol saturation, this peak shifts to an average position of 15.5 Å (Figure 3.10a). Since the samples do not expand to the expected 17 Å, yet the ~14 Å peak still considerably expands, the clays are likely randomly interstratified illite/smectite (Moore and Reynolds, 1997). After K-saturation, a peak is evident at approximately 12.9 Å, but after magnesium and subsequent glycerol saturation the ~14 Å peak in the air-dried samples splits into two peaks at 13.7 Å and 16.9 Å (Moore and Reynolds, 1997) (Figure 3.10b). Similar to the White Fan clays, the shifted peak indicates smectite, while the peak remaining at ~14 Å suggests vermiculite. The asymmetry of the illite 001 reflection (10 Å), which becomes more symmetric upon ethylene glycol saturation, suggests the vermiculite originates as a mixed-layer phase with illite.

The core sample collected from 0-22 mm depth reveals a notably different X-ray pattern than the four other samples analyzed, displaying only a minor peak at 13.27 Å in the air dried samples (Figure 3.11a). Upon ethylene glycol saturation, the ~14 Å peak broadens and reduces in intensity. Another notable difference between 0-22 mm sample and the other core sediments

analyzed is the lack of expansion for the ~14Å peak after magnesium and glycerol saturation, indicative of vermiculite rather than smectite (Moore and Reynolds, 1997) (Figure 3.11b). The low intensity and broadness of the vermiculite 001 reflection (14 Å) is likely due to mixed layering with illite.

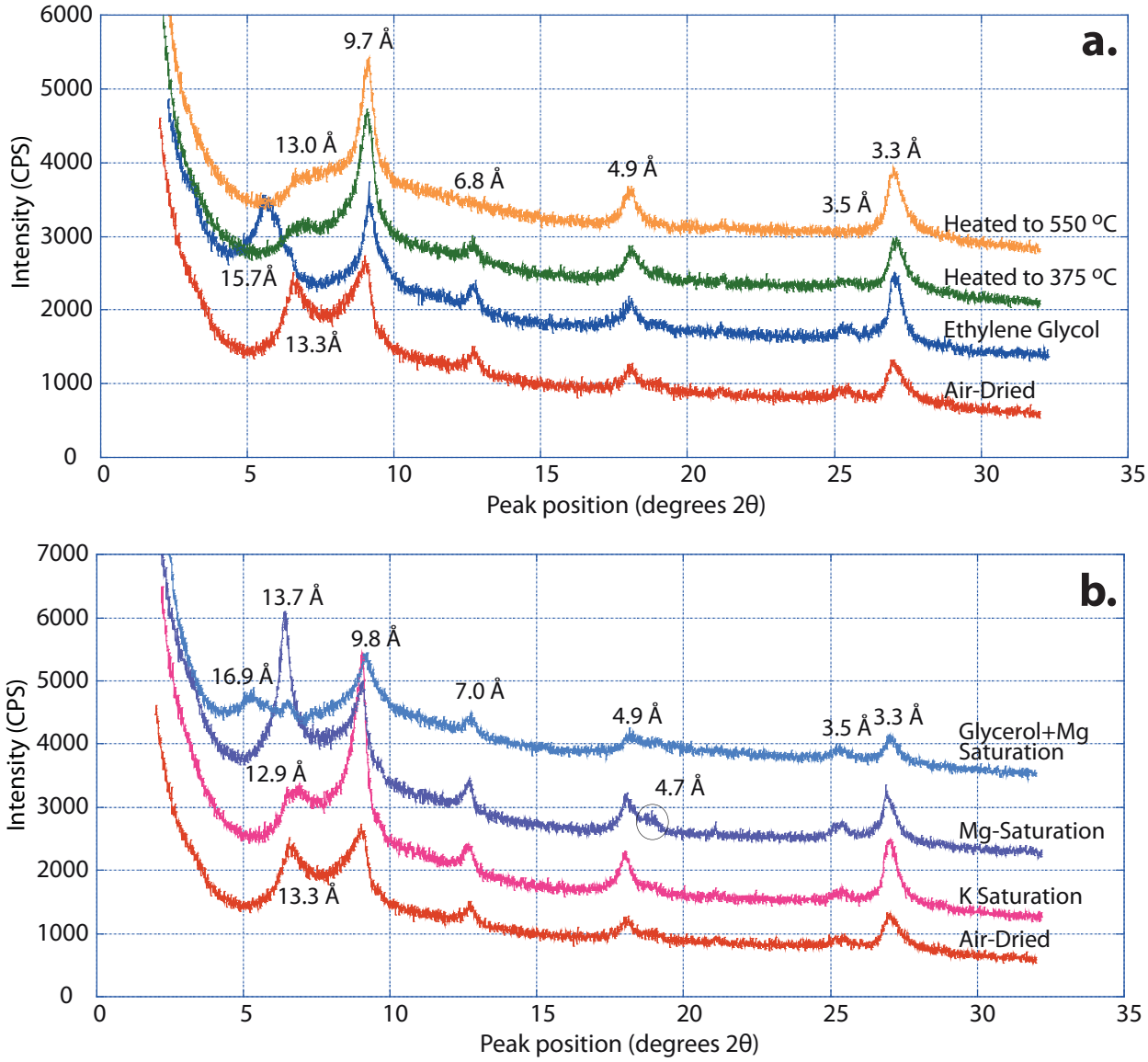

Figure 3.10. Diffractogram of an oriented mount for clay collected at 383-400 mm depth after six different treatments. With an exception for clay mineralogy in the upper 20 mm of the core, this sample is representative of the clay minerals observed in all other core samples.

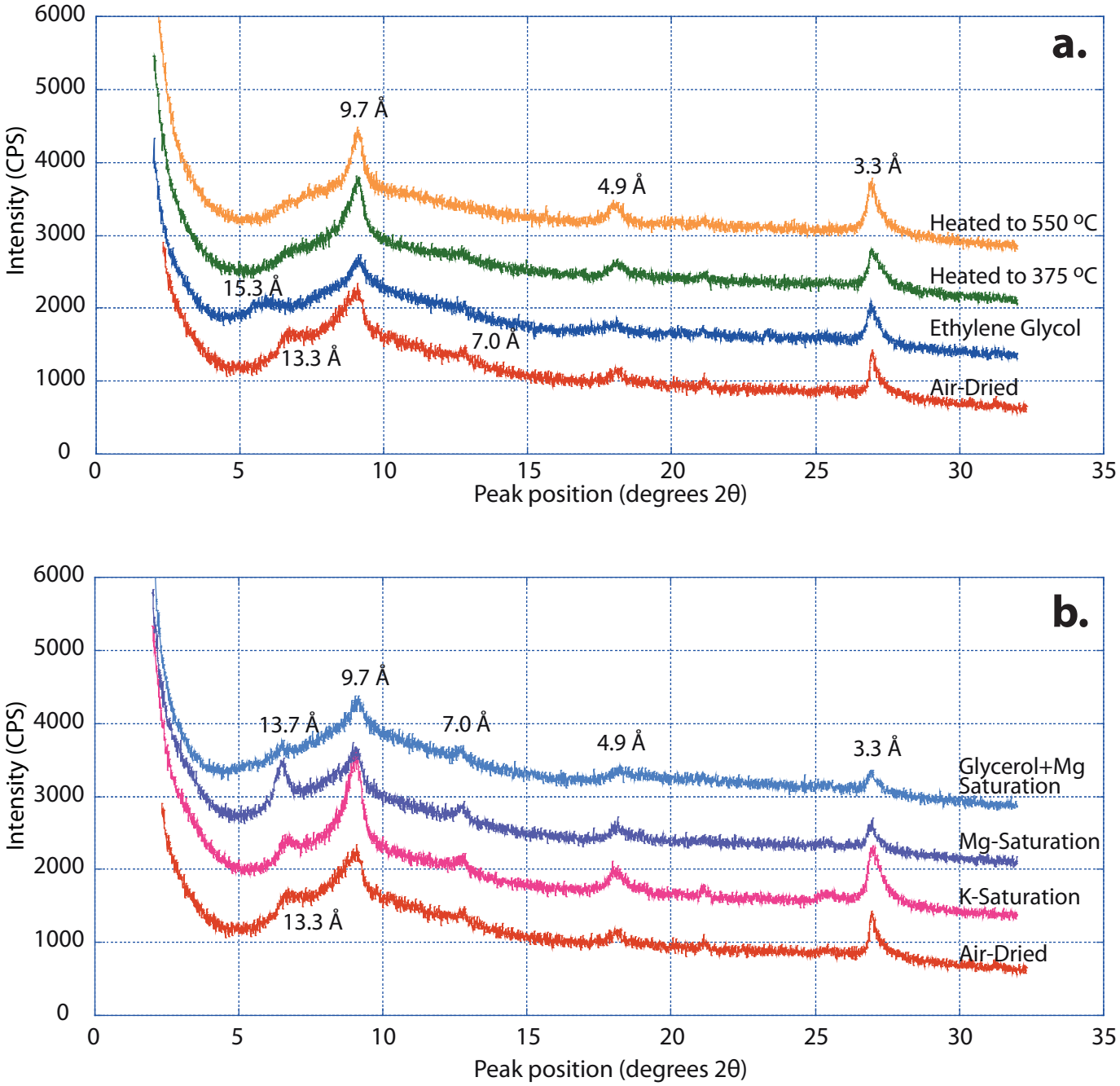

Figure 3.11. Diffractogram of an oriented clay mount for clays collected at 0-22 mm depth under six different treatments. The diffraction pattern of this clay differs from the other clays observed in the core in the relative 14 Å to 10 Å peak intensities.

3.2 X-Ray Fluorescence of Surface Sediments

3.2.1 Chemical Composition of the White Fan

Bulk analysis (<2.38 mm) for the White Fan samples demonstrates that the material is predominantly composed of calcium (36.51%) and silica (41.92%) oxides with a significant amount of magnesium oxide (12.60%). Aluminum (3.23%), iron (1.59%), and potassium (1.03%) oxides are minor components (Figure 3.12; Appendix 2). Bulk composition of the White Fan sediments does not significantly vary between samples, with the largest standard deviations for silica (±1.67%) and magnesium oxides (±1.27%), suggesting that the composition of fan sediments is fairly homogenous.

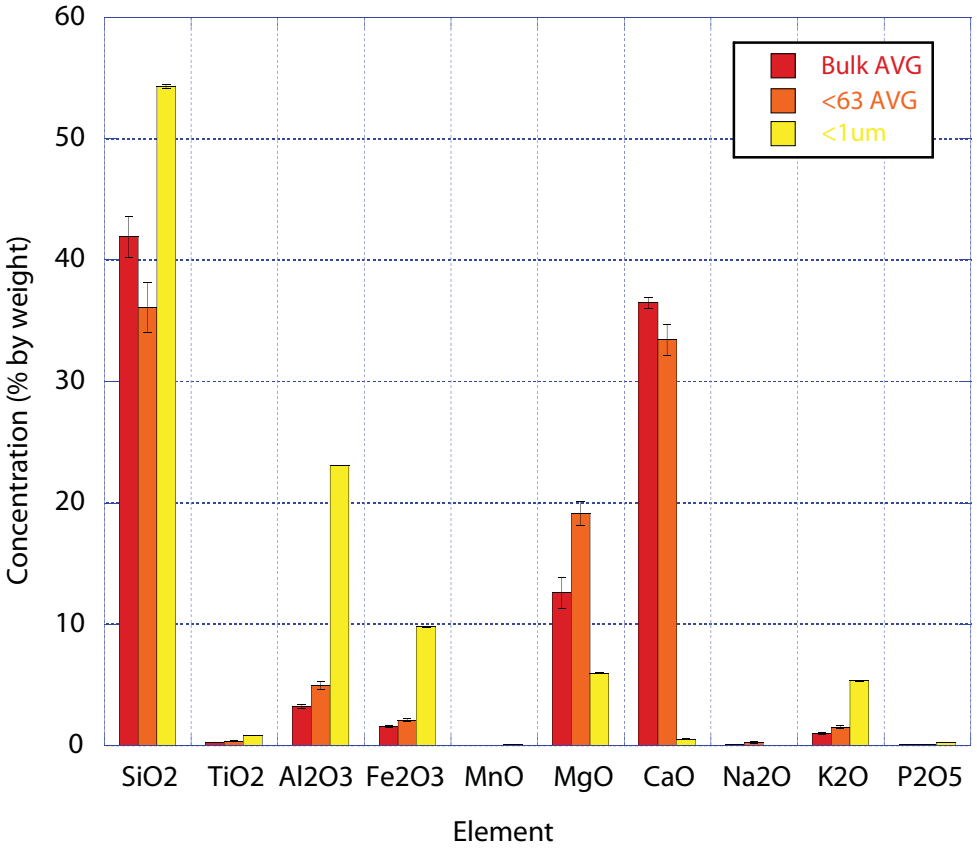

Figure 3.12: Concentration of major oxides in percent composition by weight for the bulk (red), < 63 µm (orange), and <1 µm (yellow) grain size fractions of the White Fan sediments. The error bars denote ± 1 standard deviation.

Elemental analysis of the <63 μm grain size fraction of the White Fan samples reveals depletion of silica and calcium oxide compared to bulk samples (concentrations of 36.09% and 33.45% respectively). The silt/clay size fraction was enriched in all other major oxides analyzed, with a 50% increase in aluminum, magnesium, potassium, and phosphorous oxides from the bulk concentrations. Similar to the bulk analysis, the composition of the <63 μm grain size fraction does not significantly vary between surface sediment samples, with the greatest standard deviations for silica (±2.05%), calcium (±1.29%), and magnesium oxides (±1.00%) (Figure 3.12).

The increase in aluminum and decrease in silica and calcium observed in the <63 μm fraction compared to the bulk samples likely represents an increase in clay content of the finer sediments. The elemental composition of the White Fan clay (<1 μm) deviates from the composition of both the bulk and <63 μm sediments. The <1 μm material of sample WF016 (collected from the edge of the white fan at approximately 30cm water depth) showed depletion in CaO, MgO, and Na_2O, relative to the bulk and <63 μm samples with a percent composition by weight of 0.54%, 5.98%, 0.03% respectively (Figure 3.12). Compared to the less than 63μm sediments, the <1 μm material was enriched in all other oxides, with the largest percent increases in aluminum (363% increase), iron (368% increase), and potassium (254% increase), indicating that these elements are the dominant components of the White Fan clay.

Zirconium, strontium, and cerium oxides dominate the White Fan bulk sample trace element assemblage with concentrations of 98.2 ppm, 122 ppm, and 80.8 ppm respectively (Figure 3.13). Rubidium (19.4 ppm), zinc (20.5 ppm), chrome (33.5 ppm), vanadium (25.0 ppm), and cerium (19.5 ppm) have relatively low concentrations in the White Fan sediments (Figure

3.13). Niobidium, yttrium, uranium, thorium, lead, gallium, nickel, and lanthanide are negligible components. Compared to the bulk samples, the <63 µm White Fan sediments are enriched in all of the trace elements except for strontium, which showed a 22% decrease from the bulk sediment composition.

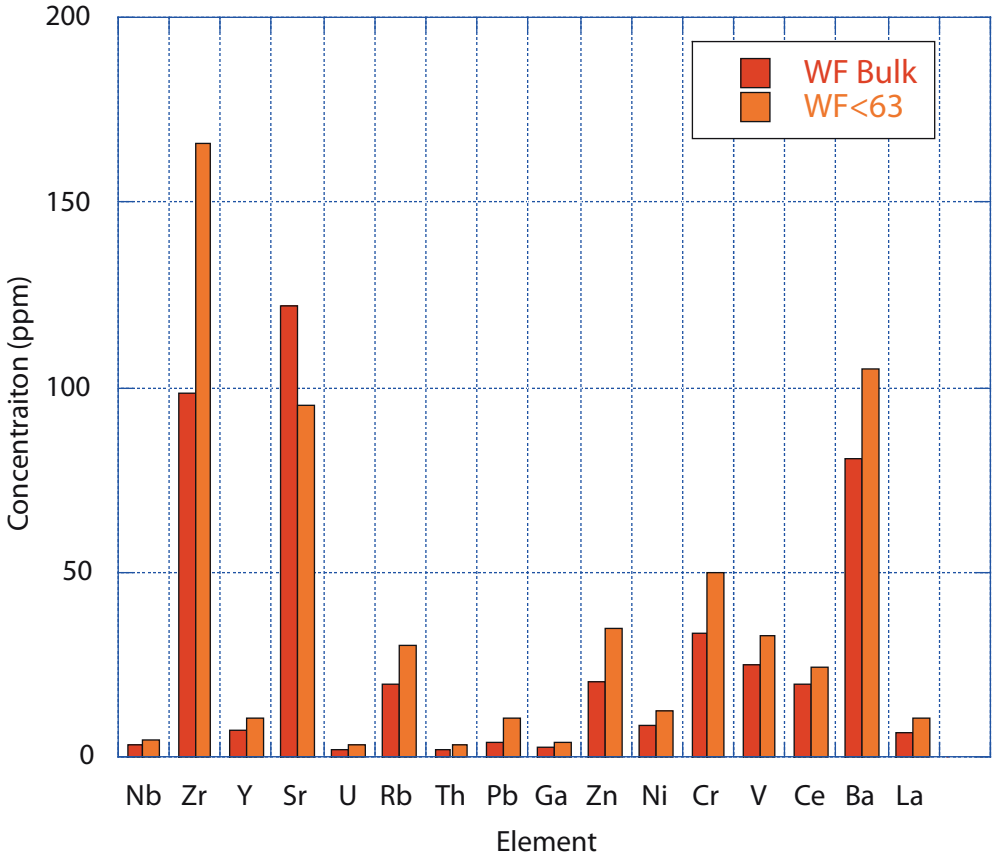

Figure 3.13. Concentration of trace elements in parts per million (ppm) for the bulk and <63 µm grain size fractions of the White Fan sediments. Limited amounts of fine-grained sediment prevented trace analysis of the <1 µm grain size fraction for trace elements.

Due to the hydroscopic nature of the ignited carbonate-rich samples, the totaled elemental compositions for the White Fan sediments only account for approximately 97-98% of the oxide concentration. During weighing of the samples, absorption of water poses a significant problem

in obtaining the required accuracy to achieve 99-100% oxide totals. However, the low standard deviations of the analyzed samples suggest that the proposed compositions accurately characterize the white fan sediments.

3.2.2 Chemical Composition of the Black Fan

Unlike the White Fan sediments, the bulk (<2.38 mm) Black Fan surface sediments are dominantly composed of silica (87.02%), with lesser amounts of aluminum (6.32%), and iron (2.76%). Titanium, magnesium, and potassium (0.48%, 0.90%, and 1.32% respectively) are a minor component of the Black Fan sediments; manganese (0.03%), calcium (0.21%), sodium (0.29%), and phosphorous (0.09%) concentrations are negligible (Figure 3.14, Appendix 2).

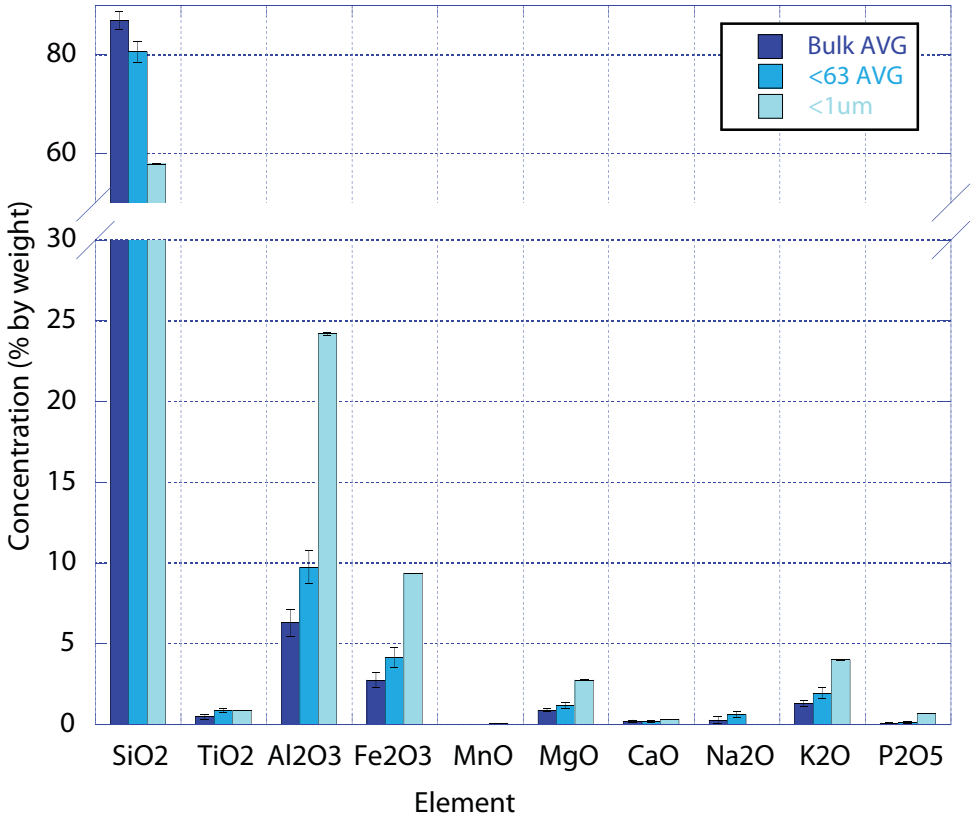

Figure 3.14. Concentration of major oxides in percent composition by weight for the bulk, < 63 µm, and <1 µm grain size fractions of the Black Fan sediments. The error bars denote ± 1 standard deviation.

Bulk composition of the Black Fan sediments does not significantly vary between samples. Similar to the White Fan sediments, the low deviation between samples suggests that the composition of sediments across the fan is fairly homogenous.

The <63 μm grain size fraction of the Black Fan sediments show on average an 8% depletion of silica compared to the bulk samples, yet revealed enrichment in all other oxides and a doubling (99-100% increase) of both manganese and titanium oxide (Figure 3.14). Aluminum, iron, and potassium oxide revealed a 60% increase in the <63 μm grain size fraction, while phosphorous and magnesium showed a 71% and 45% enrichment respectively. The composition of samples for <63 μm grain size fraction had a slightly greater variation than the bulk analyses, with the largest standard deviations for silica and aluminum (±2.67% and ±1.48% respectively) (Figure 3.14). Potassium concentrations in the Black Fan samples notably varied between all samples analyzed.

Similar to the White Fan sediments, the increase in aluminum and other oxides and the decrease in silica in the <63 μm material compared to the bulk composition of sediments likely reflects the greater clay content of the finer grain size fraction. The <1 μm material of BF003 0-2 cm (which represents the top 2 cm of a weathering horizon on the Black Fan) revealed an enrichment in most elements, with the most significant increases in iron, aluminum, and phosphorus, with percent compositions by weight of 9.39%, 24.21%, and 0.68% (Figure 3.14).

Trace element composition of the Black Fan sediments is dominated by zirconium oxide, with values of 199 ppm for the bulk sediments and 353 ppm for the <63 μm grain size fraction. Zinc (78.8), chromium (96.1), and barium (135 ppm) also are significant components of the trace element assemblage (Figure 3.15). Niobidium, yttrium, uranium, thorium, lead, gallium, and lanthanide are negligible. All trace elements reveal enrichment in the fine grain size fraction.

The Black Fan sediments contain greater concentrations than the White Fan in all trace elements analyzed except for strontium (Figure 3.15).

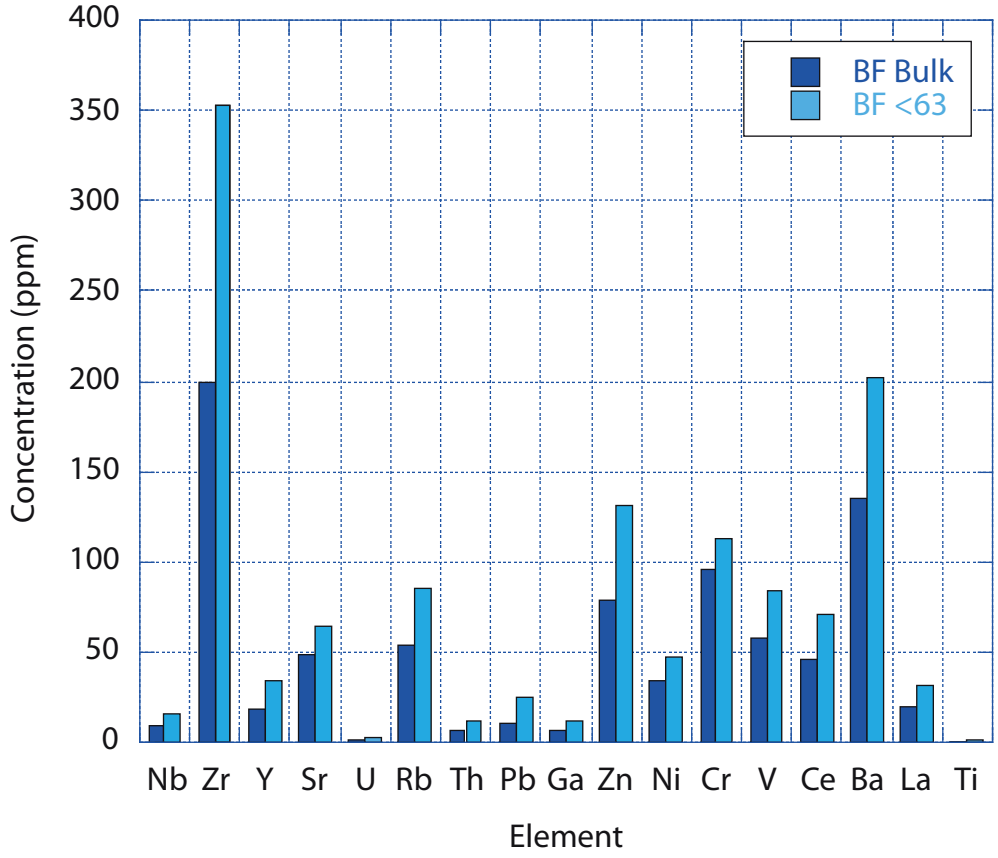

Figure 3.15. Concentration of trace elements in parts per million (ppm) for the bulk and <63 μm grain size fractions of the Black Fan sediments. Similar to the White Fan, limited amounts of fine-grained sediment prevented trace analysis of the <1 μm grain size fraction for trace elements.

3.3 Deep Basin Core Stratigraphy

Of the three cores collected, the core from the deep basin (DB-49) captured longest record of sedimentation in Kongressvatnet. DB-49 additionally displayed the least noticeable variations in grain size. Since the ITRAX Scanning XRF is sensitive to changes in porosity,

significant changes in grain size likely affect the results. Therefore, DB-49 was selected to be the primary focus of this study (Figure 2.1).

The top 28 mm of the deep basin core is composed of a gelatinous, black material that turns orange-brown upon exposure to air. No laminations are apparent in the upper section of the core (Figure 3.16). The section from 30 mm to approximately 42 mm is composed of lighter colored sediment than the overlying layer. This layer contains no internal laminations and appears to be very fine grained. Similar light-colored massive layers occur at approximately 99-111 mm and 105-205 mm (Figure 3.16).

The section of core between 40 mm to 80 mm is composed of sediments of a considerably darker brown and red/brown coloring than the deeper layers. This section is characterized by extremely fine laminations with a light-colored layer occurring at 48-49 mm depth. Below 111 mm, fine red laminations alternate with gray and brown colored laminations. The color of the laminations in this section of core is slightly redder and the grain size increases to very fine sand. The laminations are less distinct at approximately 90 mm depth (Figure 3.16).

Regular, very fine laminations occur throughout the section of the core at 300-400 mm depth. The color of these laminations is slightly redder than the overlying sediment. Below approximately 300 mm, the core sediments appear darker colored than the overlying sediment, and two black bands occur between 476 mm and 485 mm depth. The laminations in this section of the core are less distinct and composed of material of a more yellow coloring than the overlying sediment (Figure 3.16).

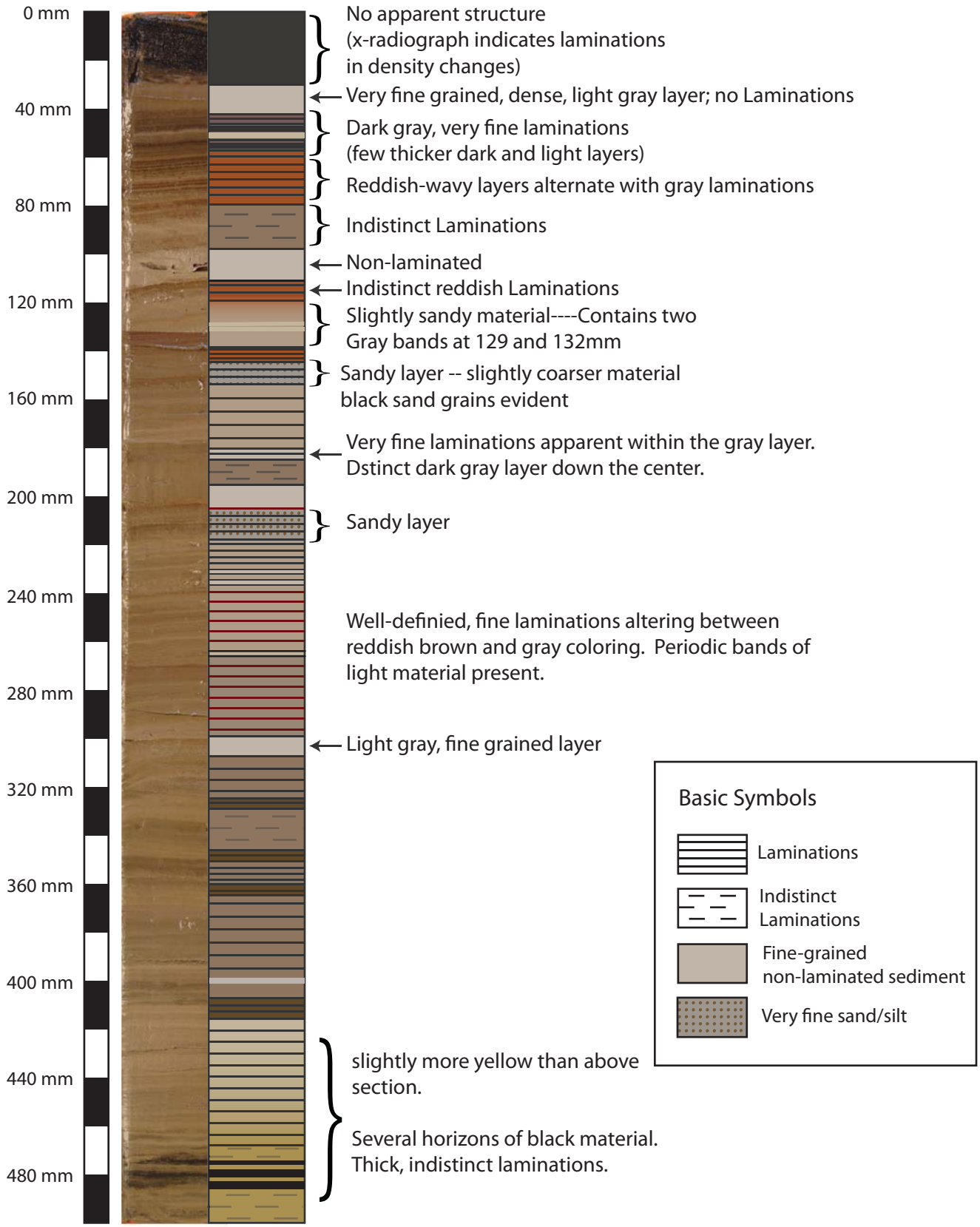

Figure 3.16. Annotated stratigraphic column of the Deep Basin core (DB-49), paired with an image of the core sediments that was taken shortly after the core was cut.

3.4 X-Ray Fluorescence of the Deep Basin Core

Variations of silica oxide throughout the deep basin core occur generally in phase with those of zirconium, rubidium, titanium, potassium, sulfur, and iron, with the greatest correlations with titanium, potassium, and rubidium (r^2 = 0.58, 0.42, and 0.37respectively[a]) (Figure 3.17, 3.18). Silica, potassium, and rubidium all reveal relative enrichment below 300 mm compared to sediments between 100-300 mm depths. Silica, iron, potassium, and rubidium additionally reveal two intense peaks at approximately 42-49 mm and 52-59 mm (Figure 3.18).

Although the general trends of these elements appear to correlate, there are several notable deviations. Peaks in iron oxide coincide with silica in the 29 mm to 310 mm range, yet this correlation does not persist in the core top (0-29 mm) or below 310 mm, the region of highest SiO_2 concentrations. Overall, iron reveals a low correlation with silica (r^2 = 0.06).

Iron and sulfur positively co-vary throughout the core (r^2 = 0.38)[b], with a notably strong correlation in the upper 300 mm of the core (r^2 = 0.55). Iron and sulfur both display strong peaks in concentration between 306 mm to 362 mm depth (Figure 3.19). The peaks coincide with a large peak in Mn, but similar spikes in concentration at this depth are not observed for any other element.

The chemistry of the core top also deviates from the co-variance observed in the lower sediments. Silica, potassium, and rubidium concentrations are relatively low, increasing in concentration until approximately 26-27 mm depth. Calcium is also relatively low in the upper 29mm of the deep basin core and sharply increases between 28mm and 31mm. Conversely, iron

[a] All correlation measurements for the Deep Basin core were calculated for sediments between 0-500 mm. Data collected below this depth (500-503 mm) all display anomalously high or low values and likely due to the collection of measurements beyond the end of the core sediments.
[b] This correlation only includes measurements from 0-499mm of the core because of a peak in iron concentration at the very bottom of the core, which is likely due to measurement beyond the core bottom.

displays relatively high concentrations in the top 30 mm, which rapidly falls to lower concentrations at the same point that calcium concentrations increase (Figure 3.18**)**.

Calcium reveals a negative correlation with silica and thus is also inversely correlated with the elements that co-vary with silica. Calcium strongly inversely correlates with iron in the upper 310 mm of the deep basin core (0-310 mm $r^2 = 0.71$). However, changes in calcium concentration below this depth do not mirror the large variation in the iron (Figure 3.18). Calcium and strontium have a negligible correlation in the deep basin core ($r^2= 0.02$). Counts per second recorded for strontium throughout the deep basin core are relatively low with little variability.

The X-Radiograph image also reveals distinct correlations with chemistry. Regions of high "brightness," in the X-radiograph indicate sections of high electron penetration, and therefore regions of low-density and high porosity. Conversely, sections of the image appearing dark indicate dense sediment, which prevents X-ray penetration.

Calcium and iron demonstrate notably strong relationship with density as inferred through X-radiography. Calcium inversely correlates with X-radiograph brightness in which regions of high calcium content correspond with "dark" or dense layers. The most notable peak in calcium concentration and density occur between 100 mm and 110 mm (Figure 3.18). Iron concentrations reveal the opposite trend, in which regions of high iron also are "light" or porous layers. Little correlation exists between X-radiograph brightness and other elements analyzed.

Iron, potassium, and to a limited extent calcium all reveal cyclic peaks at approximately 150-190 mm as well as 215-280 mm. This pattern also strongly correlates with the X-Radiograph image, in which the low iron and potassium and high calcium values correlate to dense laminations (Figure 3.18).

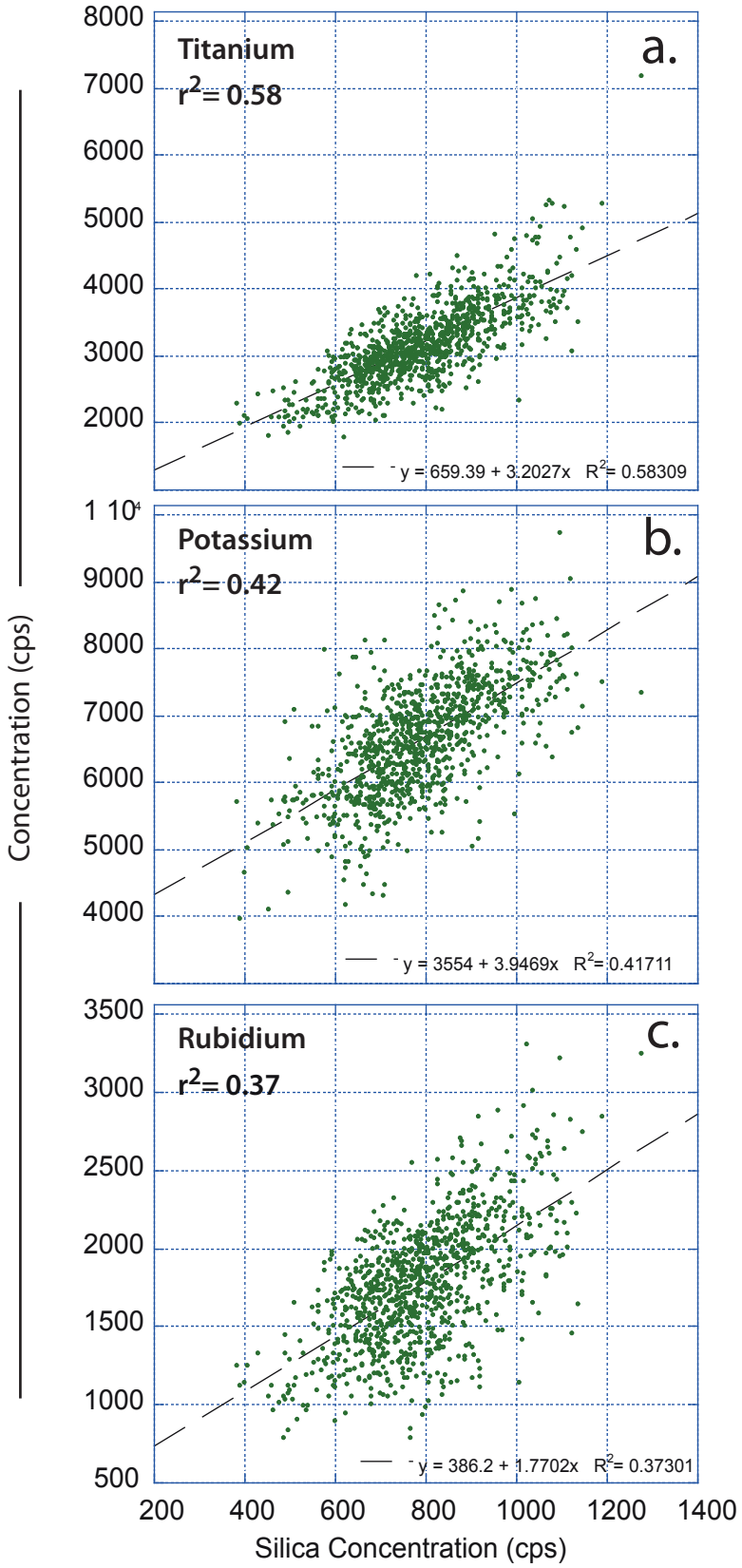

Figure 3.17. Correlation scatter plots of the ITRAX Scanning XRF results for titanium (a), potassium (b), and rubidium (b) with silica. Equations for each trend line and correlation coefficient (r2) are displayed on each graph.

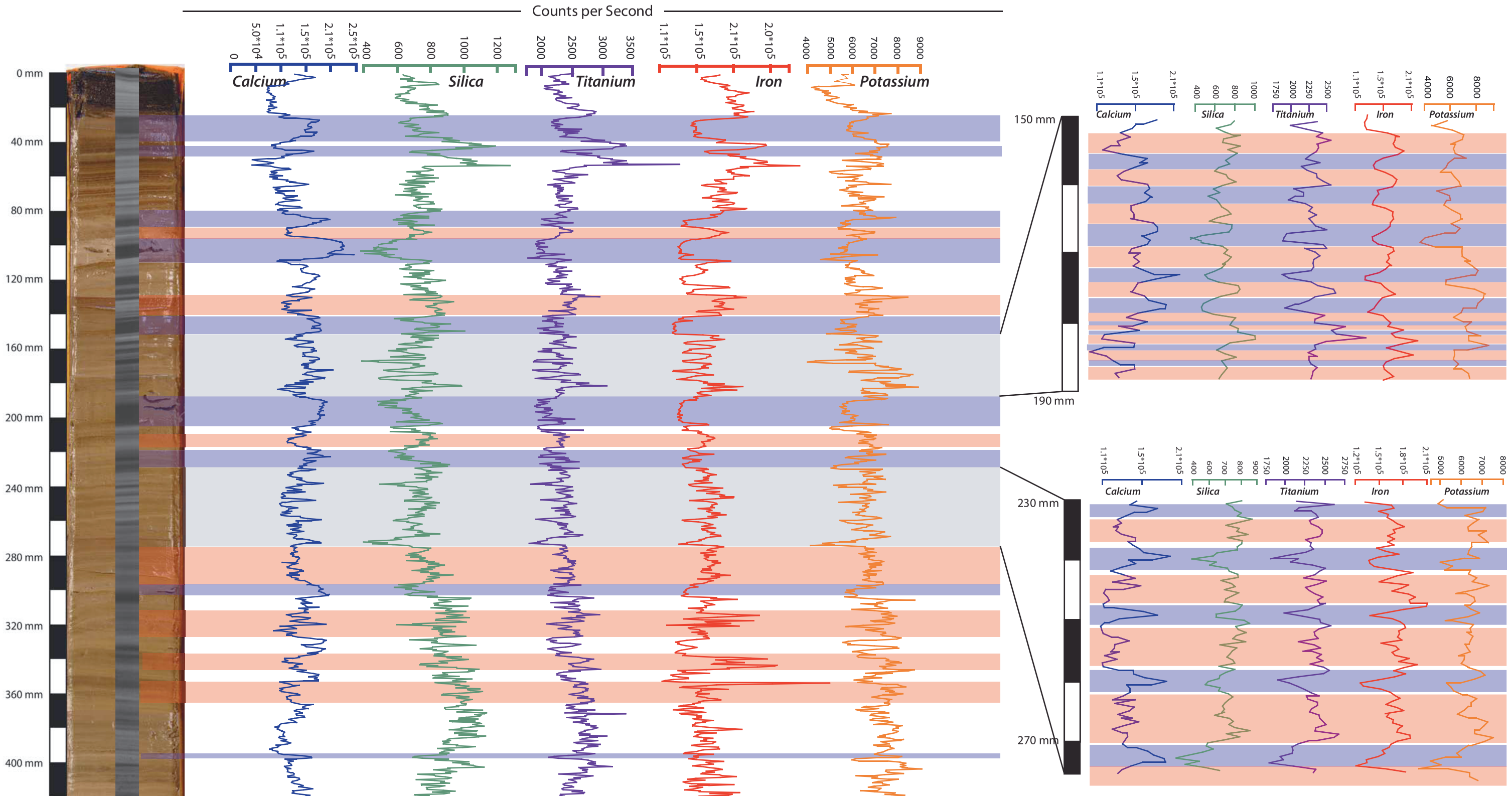

Figure 3.18: Summary of chemical trends observed in the core sediments for Ca, Si, Ti, Fe, and K. The red boxes highlight periods of low calcium and elevated concentrations of all other elements, while the purple boxes denote the opposite trend of high calcium and low concentrations of other elements. The two gray boxes mark the sections magnified in the two expanded sections (right).

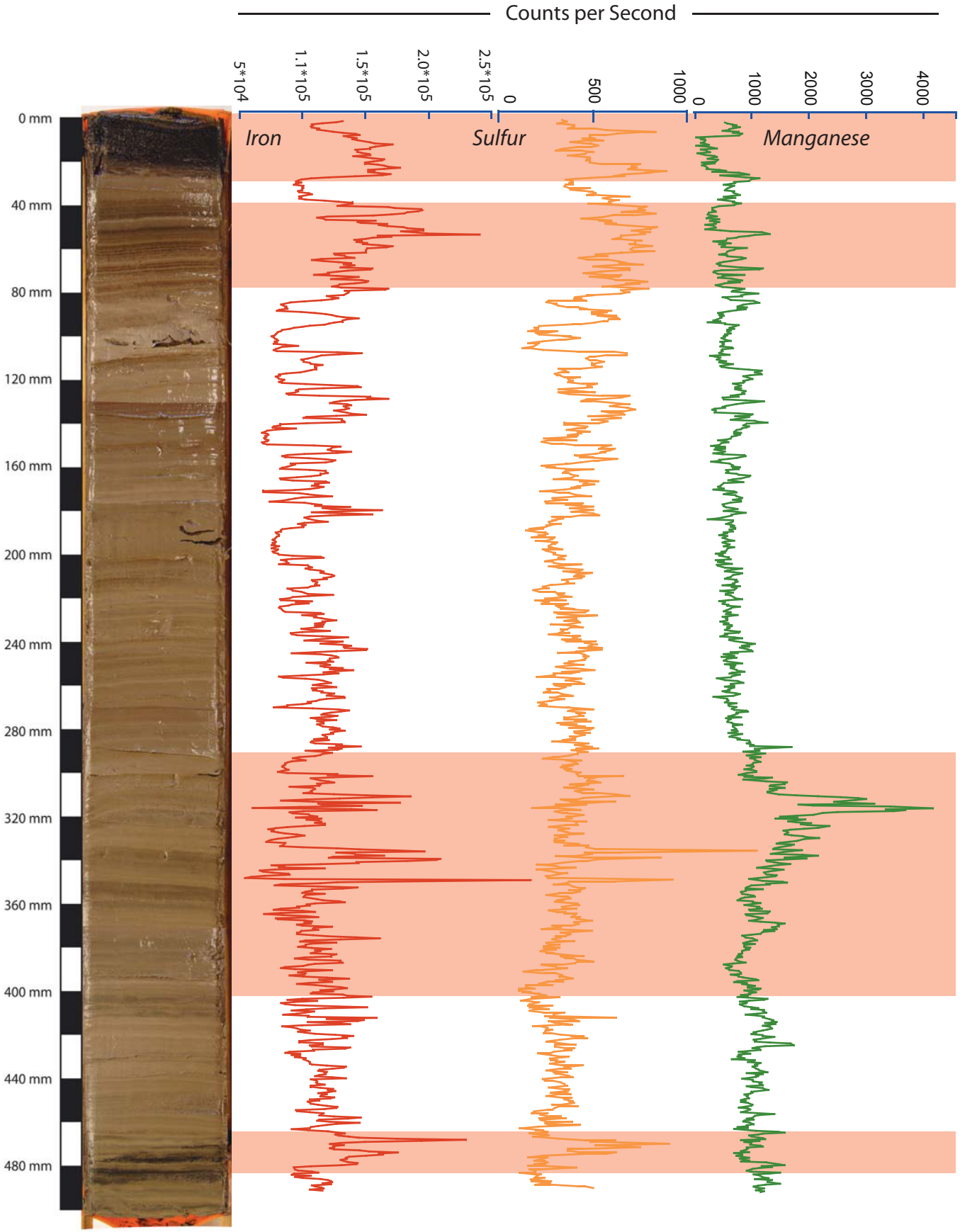

Figure 3.19. Summary of chemical trends observed in the core sediments for Fe, S, and Mn. The red boxes highlight periods of elevated iron and sulfur concentrations. Note the coincidence of the peak in Fe and S with Mn between 300-400 mm depth.

3.5 Magnetic Susceptibility

The deep basin core (DB-49) was analyzed using magnetic susceptibility to correlate the core with previous studies. The core displays overall low magnetic susceptibility with values ranging from 0-18 10^{-6} S.I. The magnetic susceptibility ranges from 1-2 10^{-6} S.I in the upper 300 mm of the core, but peaks at approximately 47 mm depth with a magnetic susceptibility of 17.8 10^{-6} S.I (Figure 3.20).

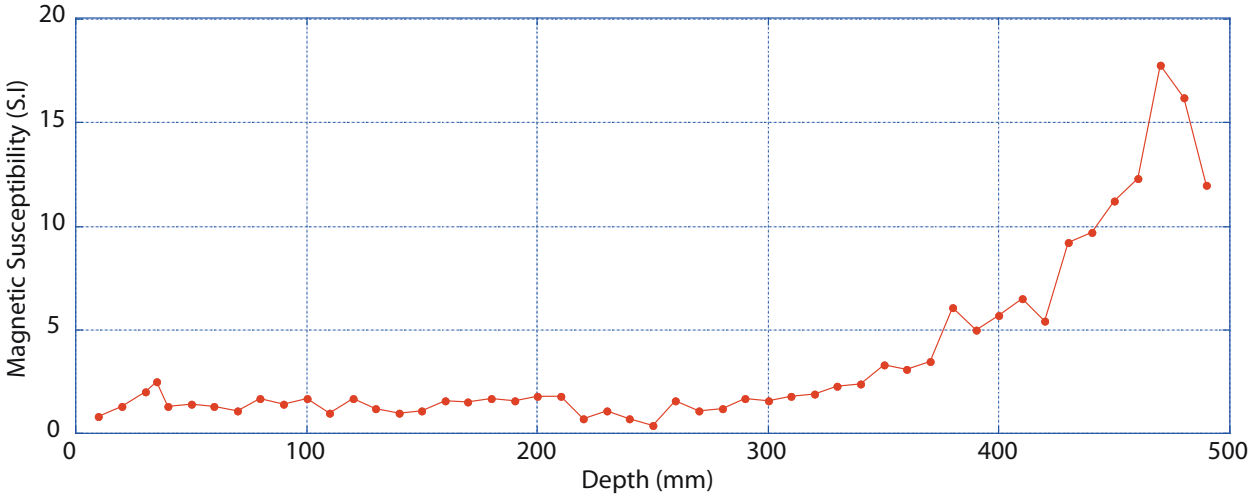

Figure 3.20: Magnetic susceptibility analysis of the deep basin core (DB-49).

3.5 Scanning Electron Microscopy and Electron Dispersive X-Ray Spectroscopy

Three samples from the deep basin core were analyzed using SEM. (depths of 10-50 mm, 122-173 mm, and 450-500 mm**).** Charging posed a significant problem during analysis of the samples in the aluminum holders, resulting in the dominant focus of SEM-EDS analysis on the two stubs prepared from depths between 40-55 mm. This section of the core is just beneath the black sediment that caps the core (Figure 3.21). SEM-EDS analysis reveals the presence of cuboidal iron sulfides, associated with what appears to be organic material. SEM analysis further reveals the presence of small euhedral rhombs ranging in size from 1 μm to 10 μm of calcite, Mg-rich calcite, and dolomite (Figure 3.21). The carbonate species tended to form in

either horizons of dolomite or calcite, rather than mixtures of the two minerals. The morphology of the rhombs varies throughout the sediment, yet many grains display sharp edges (Figure 3.21c-e). Considerable dissolution of sediments was evident in several regions of the core (Figure 3.21f).

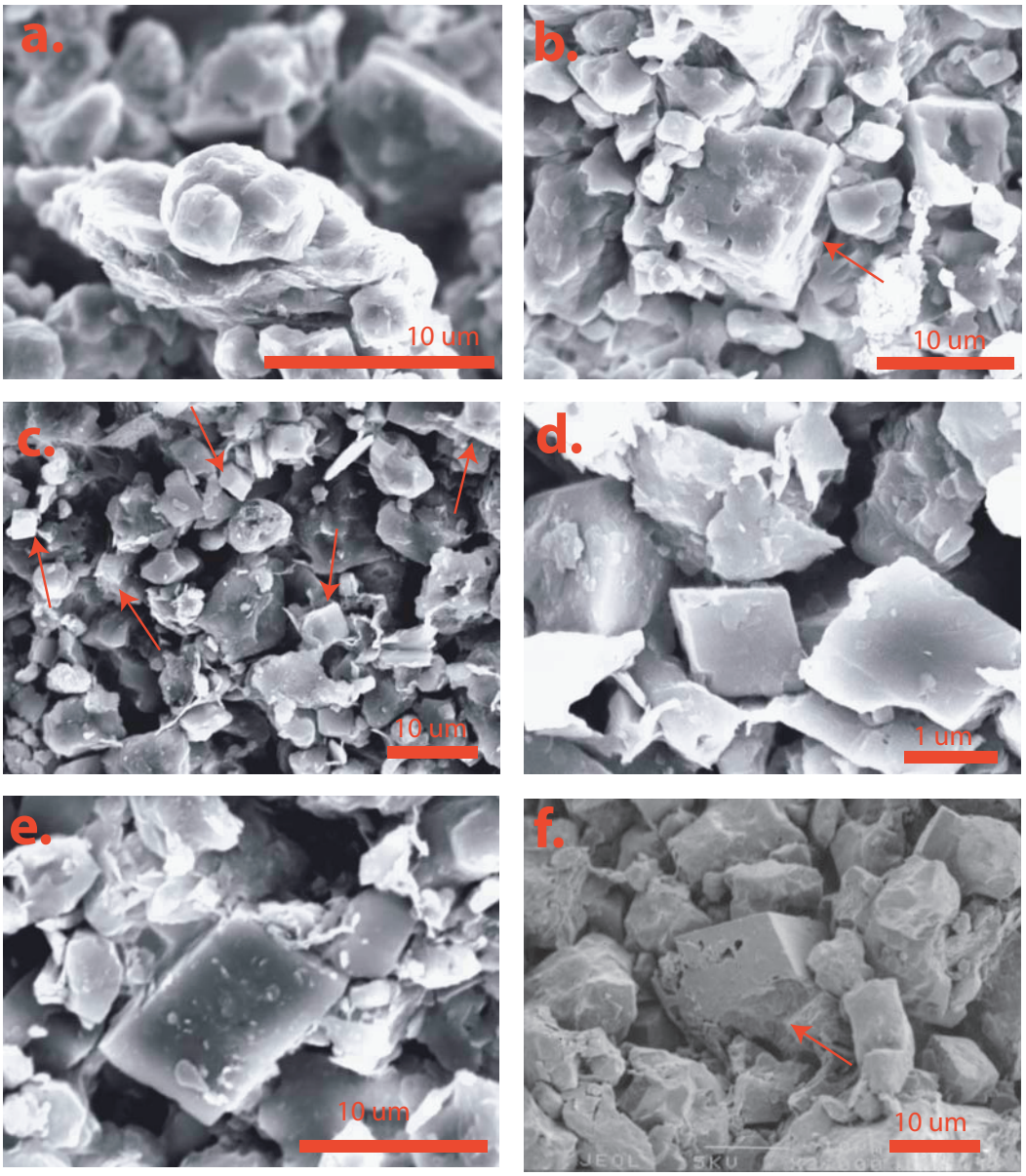

Figure 3.21. Scanning electron microscope image of the core sediments in the upper 30 mm of the core. a. Intergrowth of dolomite rhombohedra. b. Dolomitic rhomb displaying a laminar growth pattern. b. Horizon of very fine (~1 µm) euhedral calcite crystals (red arrows indicate distinct rhombs). d. Equaint, sharp-edged, calcite rhombohedron. e. Relatively large (~10 µm) calcite rhombohedron with slightly curved edges. f. Partially dissolved euhedral rhomb (red arrow).

4. DISCUSSION

4.1 Clay Mineralogy of the Black Fan Surface Sediment

4.1.1 Black Fan Weathering

The Black Fan clays are characterized by a mixture of discreet choritized vermiculite and interstratified illite/vermiculite. Although evidence of both minerals is apparent in all of the Black Fan surface sediments, the relative intensity of the illite/vermiculite 001 reflection (10 Å) and the chloritized vermiculite 001 reflection (14 Å) reveals significant variance between samples, reflecting several distinct zones of weathering in the debris flows between the two channels of the Black Fan (Figure 3.1).

As described, the fresh sediment collected from newly exposed sections of the Black Fan channels display intense 10 Å peaks and low intensity 14 Å peaks (Figure 3.2). Clays extracted from the crushed rock material further reflect this relationship with a negligible 14 Å peak and a 14Å/10Å peak ratio of 0.23 (Figure 3.5; Appendix 3). Conversely in the material collected from the upper horizon of the debris flows, which are vegetated with moss and lichen, the 14 Å reflection is nearly equivalent to or greater than the 10 Å phase (Figure 3.4).

This relationship is further illustrated by diffraction patterns for samples at site BF002, collected at varying depths. Samples collected between 5-10 cm and 10-15 cm depth reveal a significant 10 Å peak with a 14Å/10Å peak-ratio of approximately 0.6. However, the surface sediment samples collected between 0-2 cm depth have nearly equivalent 14 Å and 10 Å peaks (14Å/10Å = 1.27) (Figure 3.6). Similarly for sample BF003, also collected from a vegetated region, the 14 Å peak intensity exceeds that of the 10 Å peak at 5-10cm depth (14Å/10Å = 0.54), yet the trend is reversed in samples collected from 0-2 cm (14Å/10Å = 1.61) (Appendix 1).

The weathering profile observed at sample site BF002 also reveals the formation of an intermediary 11-12 Å, hydrobiotite-like phase due to the mixed layering of vermiculite and illite (Moore and Reynolds, 1997) (Figure 3.6). This mixed layer phase is a common intermediate in the weathering of mica-type clays to an expandable phase (Moore and Reynolds, 1997; Farmer and Wilson, 1970; Courbe et al., 1981). The ~12 Å peak disappears in the surface materials, which may reflect more advanced weathering of the clay and the formation of discreet vermiculite and vermiculite/illite.

Weathering of the Black Fan clays is also apparent in the chemistry of the Black Fan sediments. As illite weathers to vermiculite, octahedral iron (Fe^{2+}) is oxidized, reducing the layer charge and allowing mobilization of interlayer potassium ions (Galan, 2006). A generalized equation for the conversion of illite to vermiculite is as follows:

$$\left[K_{0.8}\left(MgFe^{+2}_{1.8}Fe^{+3}_{0.2}\right)\left(Si_3Al\right)O_{10}(OH)_2\right]+0.5H^+ + 0.125O_2 \rightarrow \left[\left(MgFe^{+2}_{1.3}Fe^{+3}_{0.7}\right)(Si_3Al)O_{10}(OH)_2\right]^{-0.3} + 0.8K^+ + 0.25H_2O \quad (4.1)$$

Ionic leaching is evident in the linear relationship between K_2O/Al_2O_3 plotted against the 14Å/10Å peak ratios as determined using XRD peak intensities. Thus, decreases in potassium concentration reflect increases in the intensity of the 14 Å vermiculite (001) peak and a diminishing in intensity of the 10 Å illite (001) peak (Figure 4.1). A similar, but slightly weaker relationship exists between MgO/Al_2O_3 and 14Å/10Å peak ratios (Figure 4.1**)**. However, this analysis is a general representation of relative amounts of each clay mineral present as there are many aspects that influence peak intensity (Moore and Reynolds, 1997), this relationship supports the efficacy of the 14Å/10Å peak ratios as a measure of relative amounts of weathering for the Black Fan sediments.

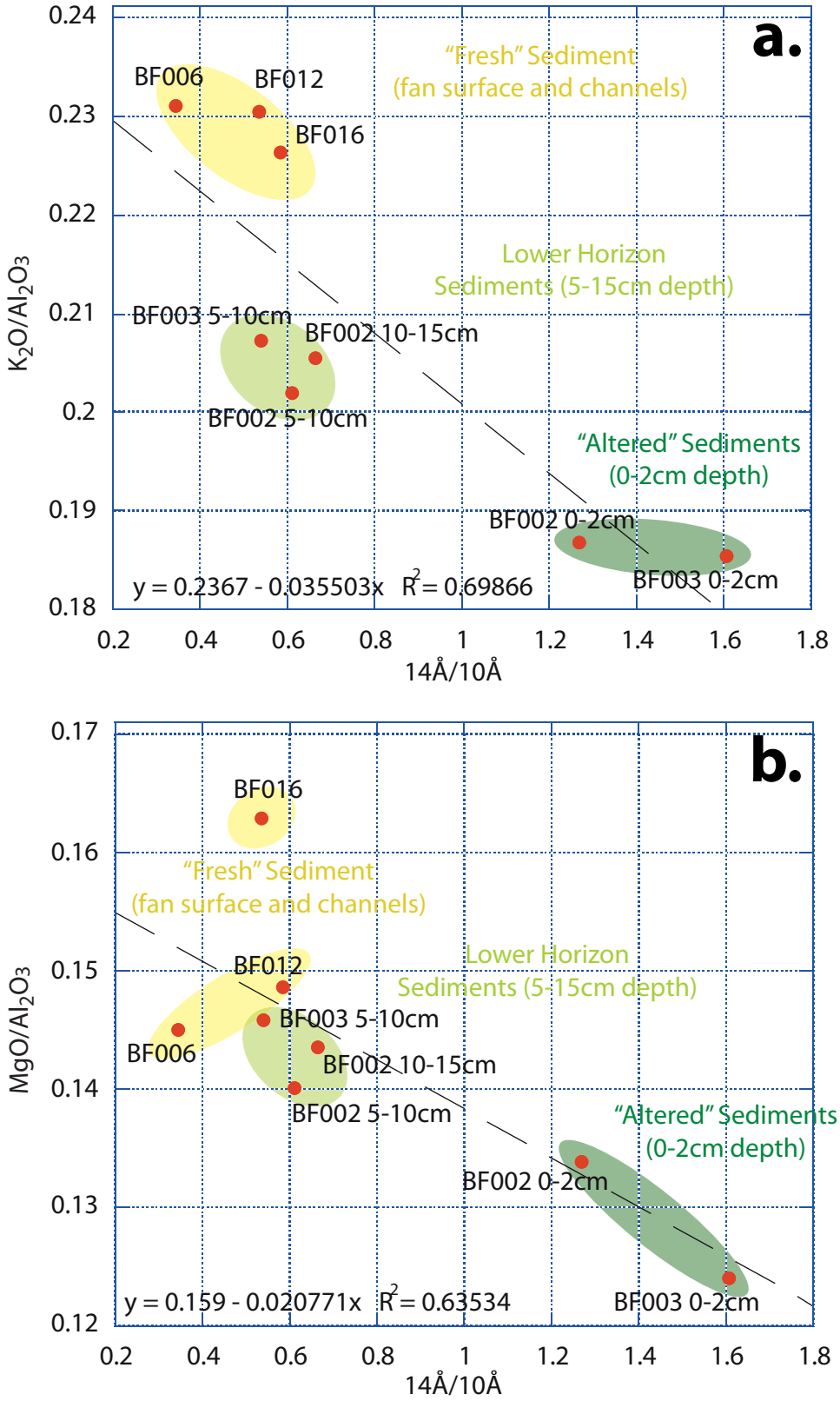

Figure 4.1: A scatter plot comparison of the 14Å/10Å peak ratios with the K/Al (a) and Mg/Al (b) of samples of variable levels of alteration: fresh sediment from the fan surface and channels (yellow), lower horizons of the debris flow lobes (light green), upper 2 cm of the debris flow lobes (dark green).

The relationship between the 14Å/10Å peak ratios and the chemistry of the Black Fan sediments reveals that the clay material collected from the channels and across the fan surface (BF006, BF012, and BF016) is the least weathered. The samples collected from the lower horizons of the debris flow lobes (BF003 5-10cm, BF002 5-10cm, BF002 10-15cm) are more weathered than the fan and channel sediments, but less altered than the samples collected from the upper horizon of the debris flow lobes (BF003 0-2cm and BF002 0-2cm) (Figure 4.1**)**.

4.1.2 Interpretations of Black Fan Weathering

Many factors affect the rate and the products of weathering including temperature, rainfall, topography, chemical composition of altering solution, and rock type (Galan, 2006). The products of chemical weathering are primarily controlled by the mineralogic composition of the original rock and the topography (Galan, 2006), where as weathering rate linearly increases with temperature (Velde, 1992).

The chemical composition of the weathered rock and the water/rock ratio are the principal factors determining the type of clay minerals formed, while temperature and time influence the rate of chemical processes.

Physical weathering in Arctic environments is commonly thought to dominate denudation processes through ice wedging and freeze/thaw action (Velde, 1992). Cold temperatures and sparse vegetation limit chemical weathering rates, which emphasizes importance of time in the formation of "soils" and clay (Velde, 1992; Galan. 2006; Anderson et al., 1997). Therefore, the abundance of clay minerals observed in the top 2 cm of the Black Fan debris flow lobes suggests that they must have been exposed for a substantial amount of time and consequently must have formed prior to the Little Ice Age advance of Kongressbreen.

Two hypotheses may explain the relatively old age of the surfaces. The fan may have been formed during a glacial advance prior to the Little Ice Age or alternatively, just the debris flow surfaces may be older. In the second hypothesis, meltwater released from Kongressbreen during the LIA eroded channels into the old debris flow surfaces during the deposition of the Black Fan.

Significant geomorphic evidence in the form of, lichenometric dating, and aerial photograph analysis supports the deposition of the Black Fan during the Little Ice Age (Anderson, 2007). A marked difference in clast size near the top of the topographic divide marks the proposed boundary for maximum LIA glacial advance (Anderson, 2007) (Figure 4.2).

Figure 4.2 Photograph facing toward the northeast, at the top of the topographic divide between Kongressdalen (left) and the valley leading to Grønfjord (right). The considerable change in clast size from along this divide marks the proposed limit for LIA glacial advance in Kongressdalen (blue line) (Image from Werner, A. Personal Communication, 2008).

Lichenometric dating revealed that the surfaces composed of larger clasts to the west of the LIA ice limit is of LIA age and the surfaces to the north are significantly older (Anderson, 2007). This evidence suggests that Kongressbreen transported meltwater into Kongressvatnet during the Little Ice Age, but did not significantly extend into Kongressdalen. The sharp slopes of the channels feeding the Black Fan also suggest a fairly recent formation and therefore support the LIA deposition of the fan (Werner, A., personal communication, 2009).

This evidence suggests that the observed weathering patterns reflect a pre-LIA glacial advance that deposited the debris flow lobes and subsequently the Black Fan was deposited during the LIA advance when meltwater from Kongressbreen carved channels through the lobes. Previous geomorphologic evaluations of the Kongressvatnet catchment also documented evidence of features attributed to earlier glaciations namely moraine-like debris lobes, trim lines, abandoned channels, and differences in lichen cover on the Kapp Starostin Formation (Anderson, 2007). Based on this evidence, Anderson (2007) proposes two additional scenarios for the position of glacial ice in Kongressdalen prior to the Little Ice Age (Figure 4.3).

Yet the question still remains, when did the earlier glaciation occur? As aforementioned, evidence from moraine position in addition to organic matter, whalebones, and lichenometric dating indicates that the Last Glacial Maximum in Svalbard occurred during the Late Weichselian (30-15 ka) (Mangerud et al., 1998; Mangerus and Landvik, 2007; Foreman, 1987). Therefore one possibility is that the older sediments were deposited during the retreat of Weichselian ice (Anderson, 2007).

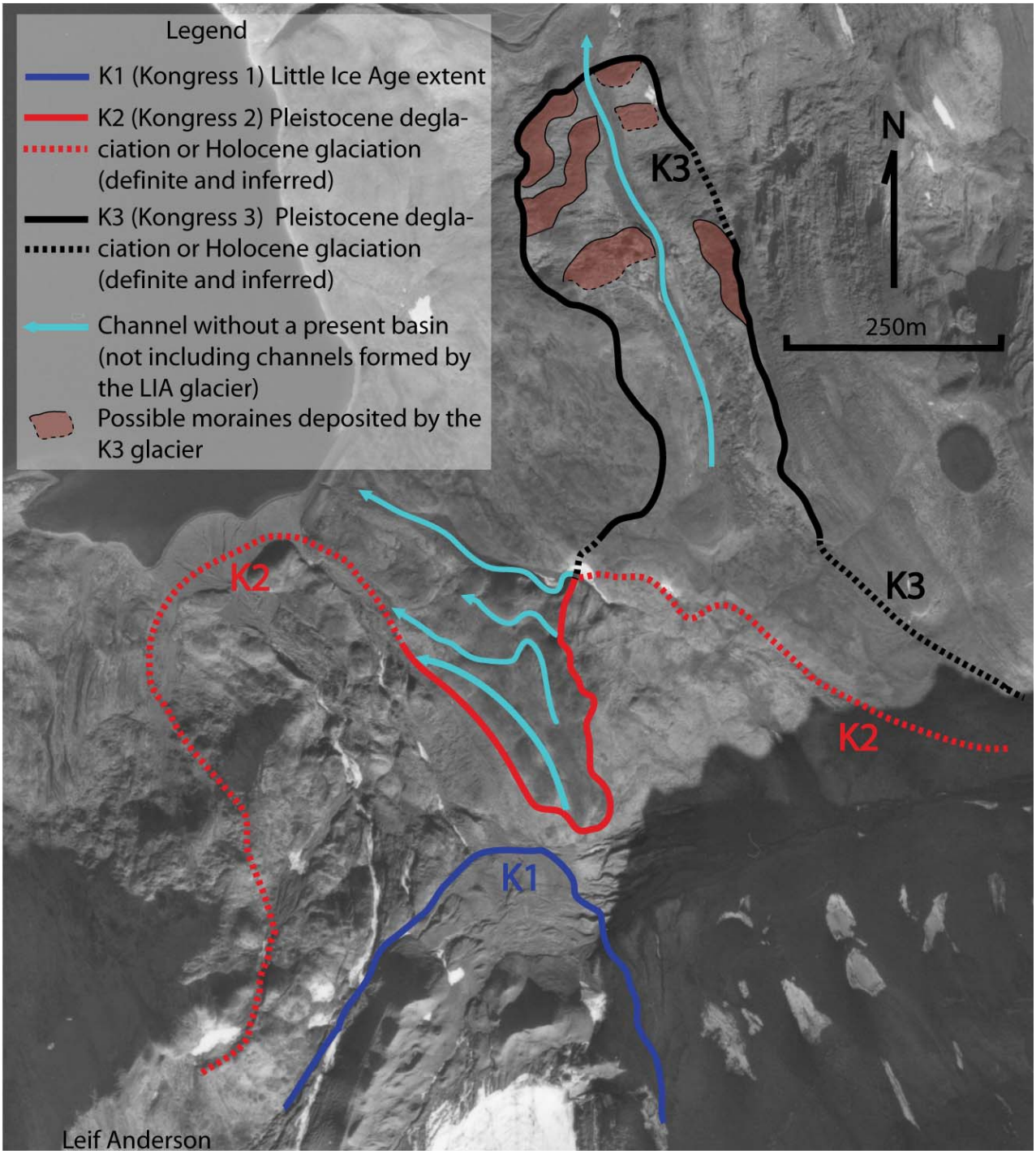

Figure 4.3: Previously proposed limits for glacial ice in Kongressvatnet during the Little Ice Age (K1, blue line) and two earlier periods of glaciation (K2, red line and K3, black line) (From Anderson, 2007).

Another possibility is that these deposits were formed during the Younger Dryas (approx. 12,900-11,500 yr BP) or the 8.2 cal yr PB glacial advances. Although significant glacial advance characterizes the Younger Dryas throughout Europe, Iceland, Greenland, and even the Canadian Rockies, evidence of an extensive advance during these periods has not yet been documented on Spitsbergen (Mangerud and Landvik, 2007; Clapperton, 1997; Nesje and Dahl, 2001).

A study of the geomorphology of the Scottbreen moraines, located approximately 50 km south of Kongressvatnet, suggests that western Spitsbergen glaciers were actually smaller during the Younger Dryas than during the Little Ice Age (Mangerud and Landvik, 2007). Linnévatnet sediment records further indicate negligible advance of Linnébreen during this time (Anderson, 2007). However, Scottsbreen and Linnébreen are both located further to the west of the proposed YD glacial ice extent than Kongressbreen (Figure 1.6a). This suggests that the glacier may have advanced during this period, yet extensive geomorphologic analysis is necessary to support this hypothesis. Based on the current evidence, it is not possible to determine the exact age of formation for the debris flow lobes, yet both Younger Dryas and the Late Weichelian glaciations are plausible sources for the altered material observed in Kongressdalen.

4.2 Provenance of Kongressvatnet Sediments

The deposition sediments from the Kapp Starostin Formation in Kongressdalen during the Little Ice Age and an older period of glaciation, suggests that changes in the elemental composition of the lake sediments should reflect these glacial periods. Many factors influence the chemical composition of lake sediments including climate, lake water redox conditions, source material, and post-depositional diagenesis (Dypvik and Harris, 2001; Junitta, 2007).

Previous studies have demonstrated that source material of fine-grained sediments is the dominant factor controlling their geochemical composition and trace element composition is one of the most sensitive geochemical parameters (Dypvik and Harris, 2001). This suggests that elemental analysis may be a valuable tool in differentiating the Black and White Fan sources in the lake sediments (e.g. Dypvik and Harris, 2001; Picone et al., 2008; Jin et al., 2006; Yang and Yun, 2007; Yang et al., 2007).

4.2.1 Surface Sediment Chemistry

The X-Ray Florescence analyses of the White and Black Fan sediments reveals that the two fans are covered in rock material with distinctly different chemical signatures. The chemistry of fan sediments vary with grain size, but despite these variations, both the bulk and the <63 μm fractions from the two fans have considerably different major and trace elements compositions. The Black Fan sediments have greater concentrations of K_2O, Fe_2O_3, Zr, Cr, while the White Fan sediments are characterized by higher concentrations of MgO, CaO, Sr, and slightly greater concentrations of U (Figure 4.4, 4.5). These results suggest that the chemistry of the core samples should reflect the relative contribution of each fan.

4.2.2 Core Chemistry

The 5 sub-samples from the deep basin core (DB-49) collected at depths of 0-22mm, 30-40mm, 99-111mm, 195-211mm, and 383-400mm, have chemical compositions similar to the White Fan (Figure 4.4, 4.5). Even though these samples span the maximum range of calcium and silica concentrations, all display similarly elevated MgO and CaO and depletion in K_2O and Fe_2O_3 concentrations as the White Fan surface sediments.

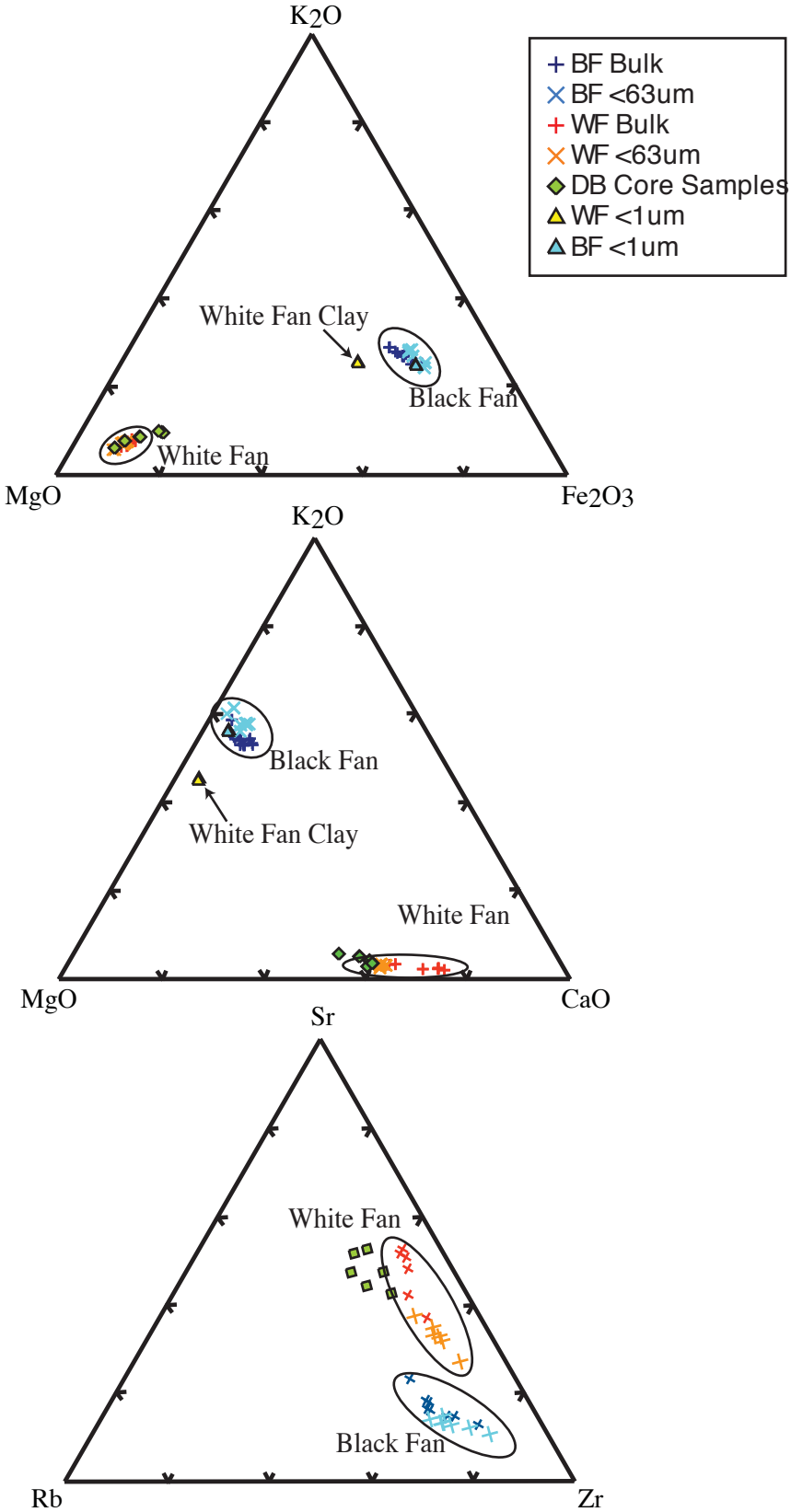

Figure 4.4. Ternary diagram demonstrating the characteristic major and trace element compositions for the White and Black Fans (red/orange/yellow and dark blue/light blue/turquoise respectively) and the sub-sampled core sediments (green diamonds). An oval is used to define the signature for each fan.

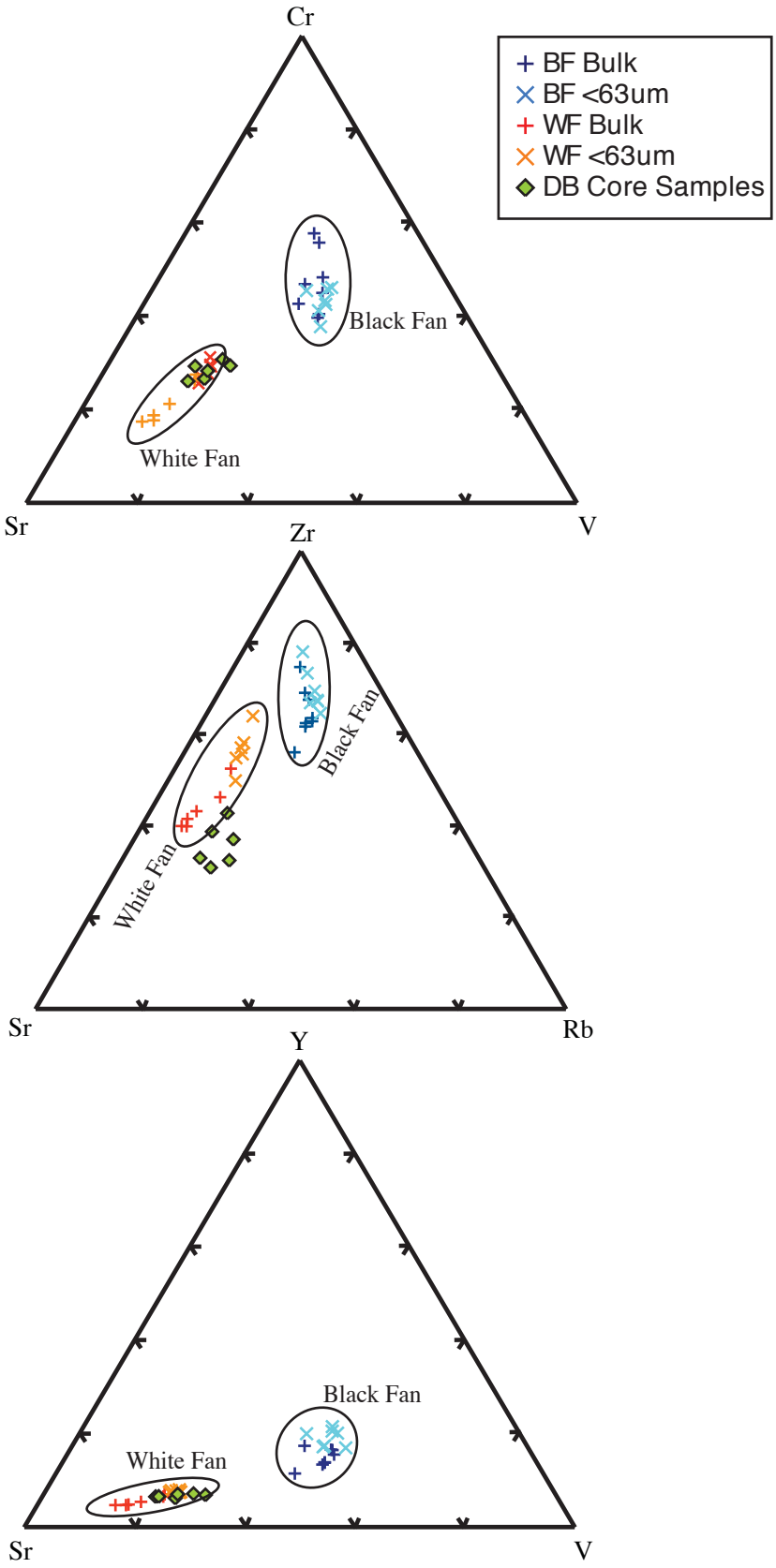

Figure 4.5. Ternary diagrams revealing distinctly different chemical signatures for the trace element assemblage of the White and Black Fans (red/orange/yellow and dark blue/light blue/turquoise respectively). Plotted sub-sampled core sediments (green diamonds) reveal similar composition to that of the White Fan.

Scatter plot comparisons of the core and the fan sediments further reveal the absence of a Black Fan signature in the core chemistry. The magnesium to aluminum ratios for combined bulk, <63µm, and <1µm grain size fractions of the fan sediments reveal a strong linear correlation for the Black Fan ($r^2 = 0.79$)[c] and positive linear trend for the White Fan, which is affected by the lack of magnesium in the White Fan clay samples. The core sediment concentrations of Mg to Al resemble the White Fan sediments with relatively high weight percent of magnesium compared to the percent composition of aluminum (Figure 4.6).

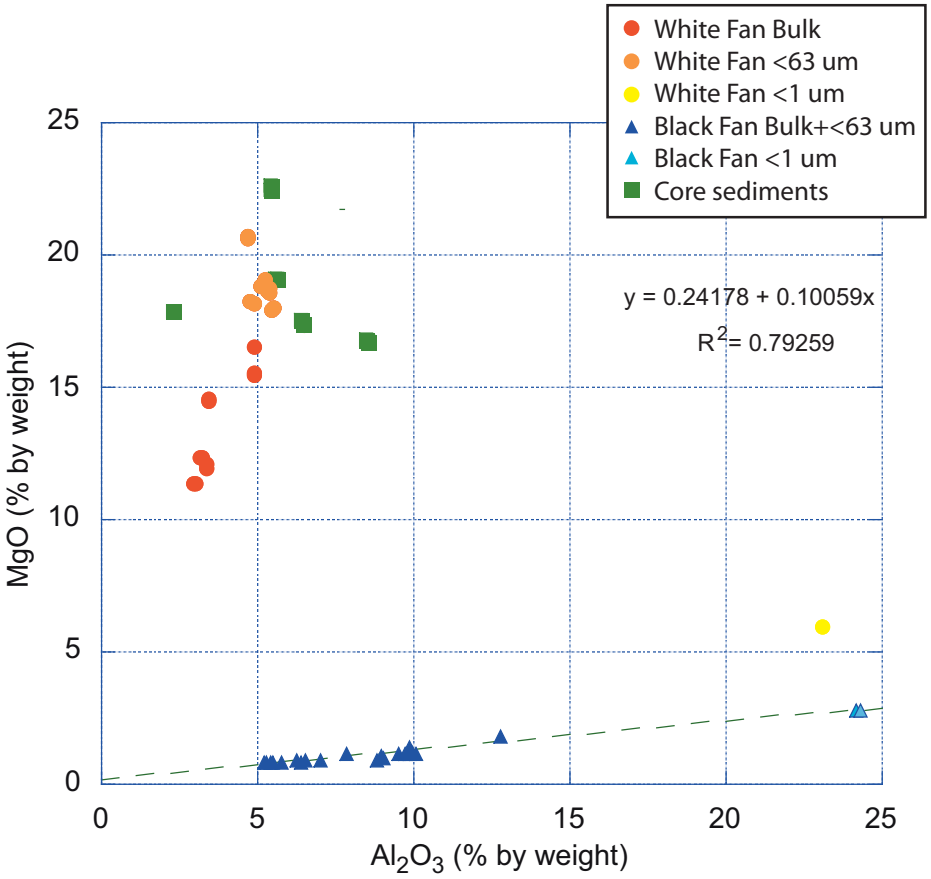

Figure 4.6. Scatter plot revealing the trend in Mg to Al of the White and Black Fans (red/orange and dark blue respectively). The deviation of chemistry for the <1 µm grain size fraction of the White Fan from the overall chemistry of the sediments.

[c] Pearson's correlation coefficient was calculated without the chemistry of the clay material due to the considerable difference in chemistry from the surface sediments. With the clay chemistry included in the regression analysis, $r^2 = 0.96$.

In order to directly compare the results from the ITRAX Scanning X-Ray Fluorescence in counts to the chemistry of the fan sediments in percent composition by weight, the chemistries of the 5 samples from the Deep Basin core were used to roughly calculate conversion ratios for each element. The average of the calculated ratios for the 5 samples was used as the final conversion factor (Appendix 4).

Similar to the sub-sampled core sediments, the converted percent composition by weight plotted on the ternary diagrams of the White and Black Fan sediments, lack the Black Fan chemical signature (Figure 4.7). A slight depletion in calcium and potassium of some of the core samples suggests limited mixing with Black Fan sediments may occur. Three samples plotted on the ternary diagram may have up to 30-40% Black Fan sediments, based on their relative positions between the compositions of the two fans (Figure 4.7). However, the bulk of samples appear to be composed at least 75% White Fan sediment. Significant contribution of Black Fan sediments, as would be expected from glacial inflow, is not apparent in any of the core samples.

4.2.3 Core Mineralogy

X-Ray Diffractometry reveals that the mineralogy of the <1 μm grain size fraction of the core samples is similar to that of the White Fan, displaying smectite 001 (~14 Å) and illite 001 (~10 Å) reflections of nearly equivalent intensity (Figure 3.10, 3.11). The similarity of the clays from the core to those collected from the surface of the White Fan further supports the dominance of White Fan contribution throughout the core.

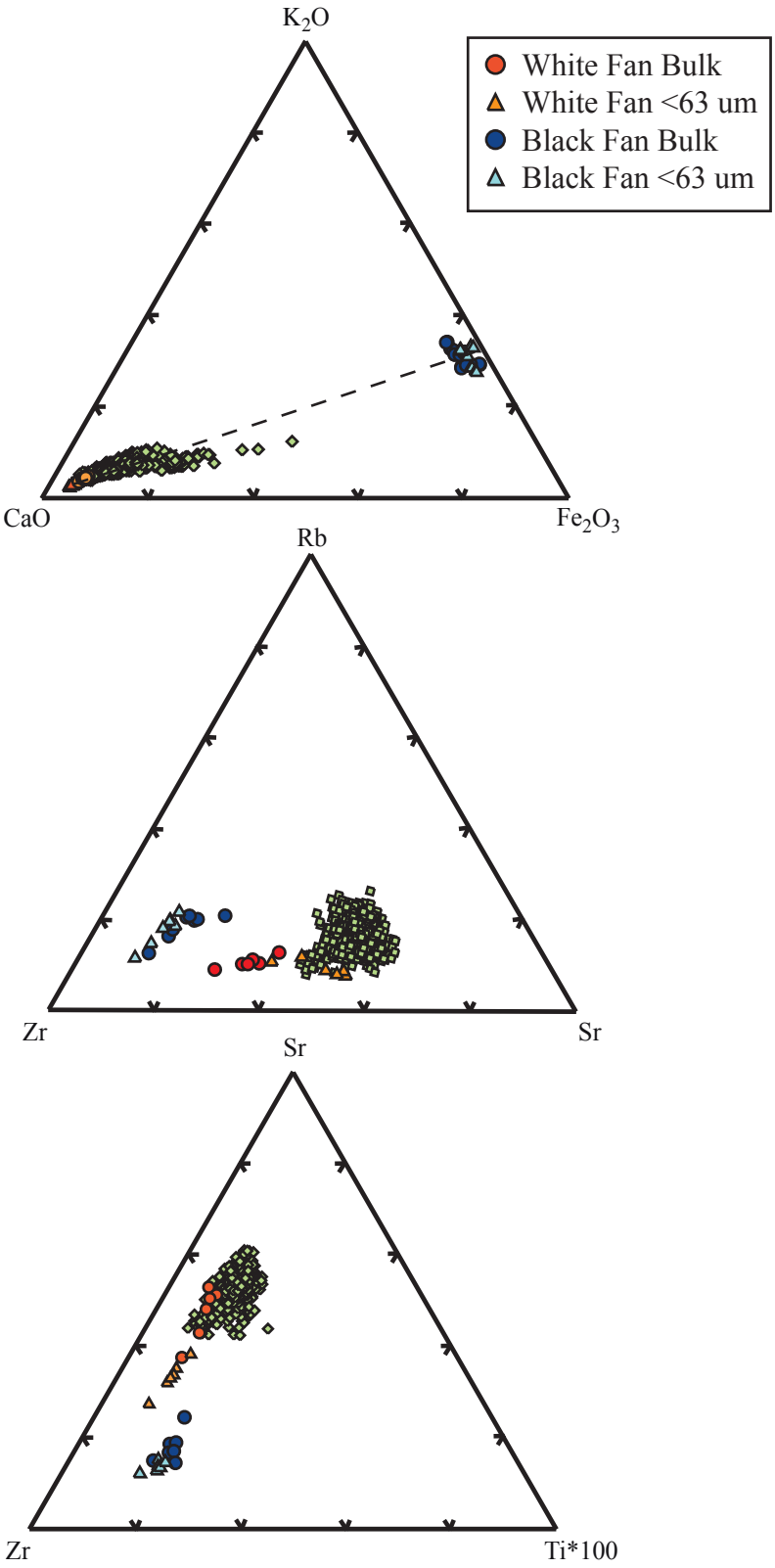

Figure 4.7. Ternary diagram of the White and Black Fan chemistries (red/orange and dark/light blue respectively) and the calibrated concentrations for the core sediments (green diamond). The dashed line (top) marks the intermediate chemistries between the signatures of the two fans revealing limited mixing of White and Black Fan chemistry in the core sediments.

Unexpectedly, the XRD pattern for the <1 μm sediment between 0-22 mm of the deep basin core resembles that of the clays extracted from the White and Black Fan rock material (Figure 3.11). The clay in this section of the core is dominantly composed of illite that is interstratfied with an expandable phase that may be the result of the alteration of smectite to illite. Thus, the clay sediment of the upper section of the core could have originally had a similar composition to the White Fan clays, yet was altered post-deposition. However, a more detailed study of the mineralogy of Kongressvatnet clays is required to draw further conclusions on post-depositional diagenesis.

4.2.4 Interpretation of Provenance

The chemical composition and clay mineralogy of the core and surface sediments indicate that the dominant material deposited into the lake originates from the White Fan. Two hypotheses may explain in the absence of Black Fan sediment in the core. The interval captured in the core may not extend back to the time when the Black Fan was active. This is most likely if the fan formed prior to the Little Ice Age. However, there is considerable geomorphic evidence that the Black Fan was active during the Little Ice Age.

The core is likely long enough to capture the Little Ice Age event, which ended during the early 20th century (Svendson and Mangerud, 1997). Although the Kongress cores are difficult to date because of the presence of carbonate rocks, lack of organic input, and carbon coal seams in the region, Guillizzoni et al. (2006) establishes a chronology for Kongress lake sediment using a combination of radiometric dating, varve counting, and paleomagnetics. Magnetic susceptibility correlation of DB-49 with the Guillizzoni et al. (2006) cores indicates that the core sediments analyzed in this study record deposition in Kongressvatnet from

approximately 600 AD (Figure 4.8). Thus the deep basin core should contain sediments deposited prior to the end of the Little Ice Age.

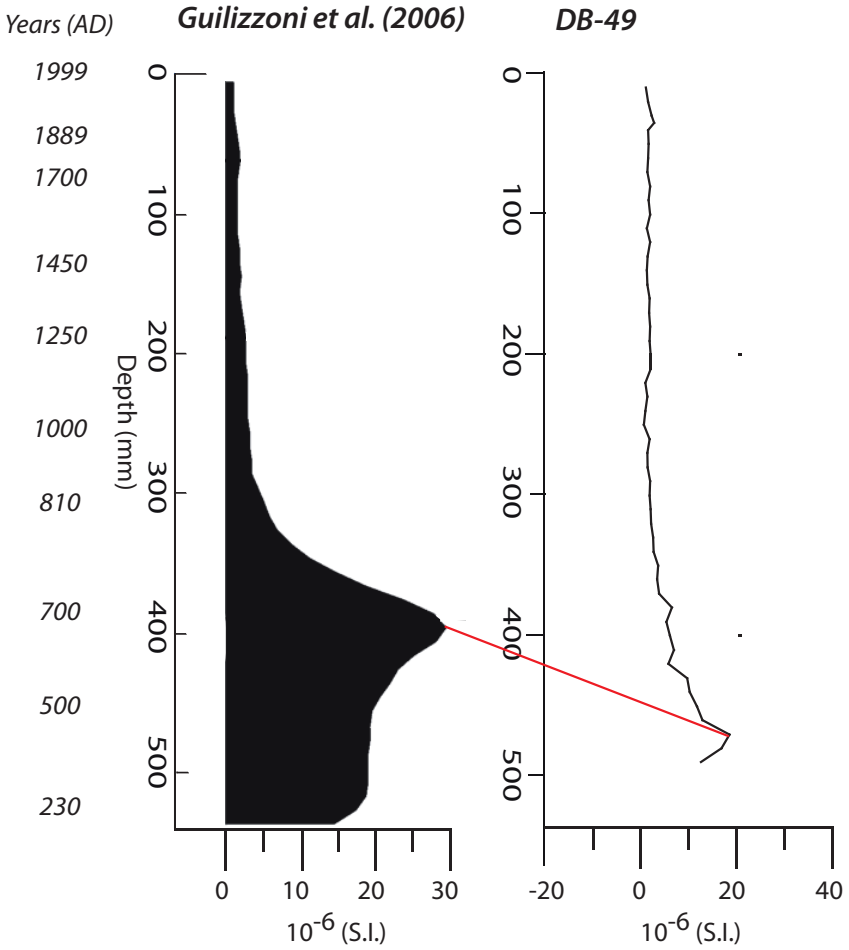

Figure 4.8: Magnetic susceptibility correlation of the deep basin core (DB-49) with Kongress cores dated by Guilizzoni et al. (2006).

A more plausible explanation for the absence of Black Fan sediments in Kongressvatnet is the formation of the fan by a cold-based glacier, which did not produce the fine glacial flour commonly associated with warm based glaciers. Based on moraines and supraglacial features, warm, cold, and polythermal glaciers have all been suggested to exist in Svalbard (Lonne and Lyså, 2005). Yet valley glaciers in Svalbard, such as Kongressdalen, commonly have cold-based margins (Lonne and Lyså, 2005). Supraglacial processes dominate the deposition of till in cold-

based glaciers, which commonly results in the formation of ice-cored moraines and subsequent melting results in hummocky terrain (Lonne and Lysså, 2005; Boulton, 1972). The observation of both of these features in the valley that once contained Kongressbreen further supports the cold-based classification of this glacier (Figure 4.9). Supraglacial deposits tend to be coarse grained. Thus, meltwater transporting the Black Fan sediments into Kongressdalen was dominated by coarse material and deficient in silt and clay sized sediment.

Figure 4.9. Evidence of Kongressbreen as a cold-based glacier: hummocky terrain in the valley east of the lake. The yellow arrow marks an ice-cored moraine identified during the 2008 field season.

4.3 Chemistry of the Deep Basin Core

4.3.1 Chemical Varves in Kongressvatnet

Despite a lack of significant changes in provenance, the sediments from Kongressvatnet reveal considerable variation in their chemical composition. ITRAX scanning XRF analysis of

the rhythmically laminated regions of the deep basin core reveals alternating calcium rich layers with silica, titanium, potassium, and iron rich layers (Figure 3.18).

The silica, titanium, potassium and iron rich sediments likely represent laminations dominated by clay minerals. Potassium and aluminum reveal a strong correlation in the <63 μm and bulk grain size fractions of the White Fan sediments (r^2=0.96), which likely results from interlayer potassium in illite (Figure 4.10a). Iron and aluminum also are strongly correlated (r^2 = 0.97) in the <63 μm fraction of the White Fan surface sediments (Figure 4.10b). Since iron commonly exchanges for silica in the tetrahedral layers of smectite, the correlation suggests that iron originates in the White Fan clay (Langmur, 1997; Moore and Raynolds, 1997).

Titanium does not correlate with aluminum and silica in samples from the White Fan but it does correlate with silica throughout the deep basin core (r^2 = 0.58) (Figure 3.17a). However, titanium is commonly associated with clay minerals due to anatase or rutile impurities (Cited as Raman and Jackson, 1965 in Borchardt, 1989) and the <1 μm grain size fraction of the White Fan sediments contains over twice the concentration of titanium than the <63 μm sediments (Appendix 2). Thus the relationship between titanium and silica observed in the core likely reflects winter clay deposition.

This apparent coupling of calcium-rich sediments capped with a clay layer, is suggestive of varves in which the summer inflow from the dolomitic White Fan deposits the calcium rich sediments, while the silica, titanium, and iron represent the winter clay lamination that settles from the water while the lake is ice-covered (Figure 3.18). Based on a comparison of paleomagnetic and $^{137}Cs/^{210}Pb$ age models with varve counting, Guilizzoni et al. (2006) previously suggested that the laminations of Kongressvatnet sediments are annual.

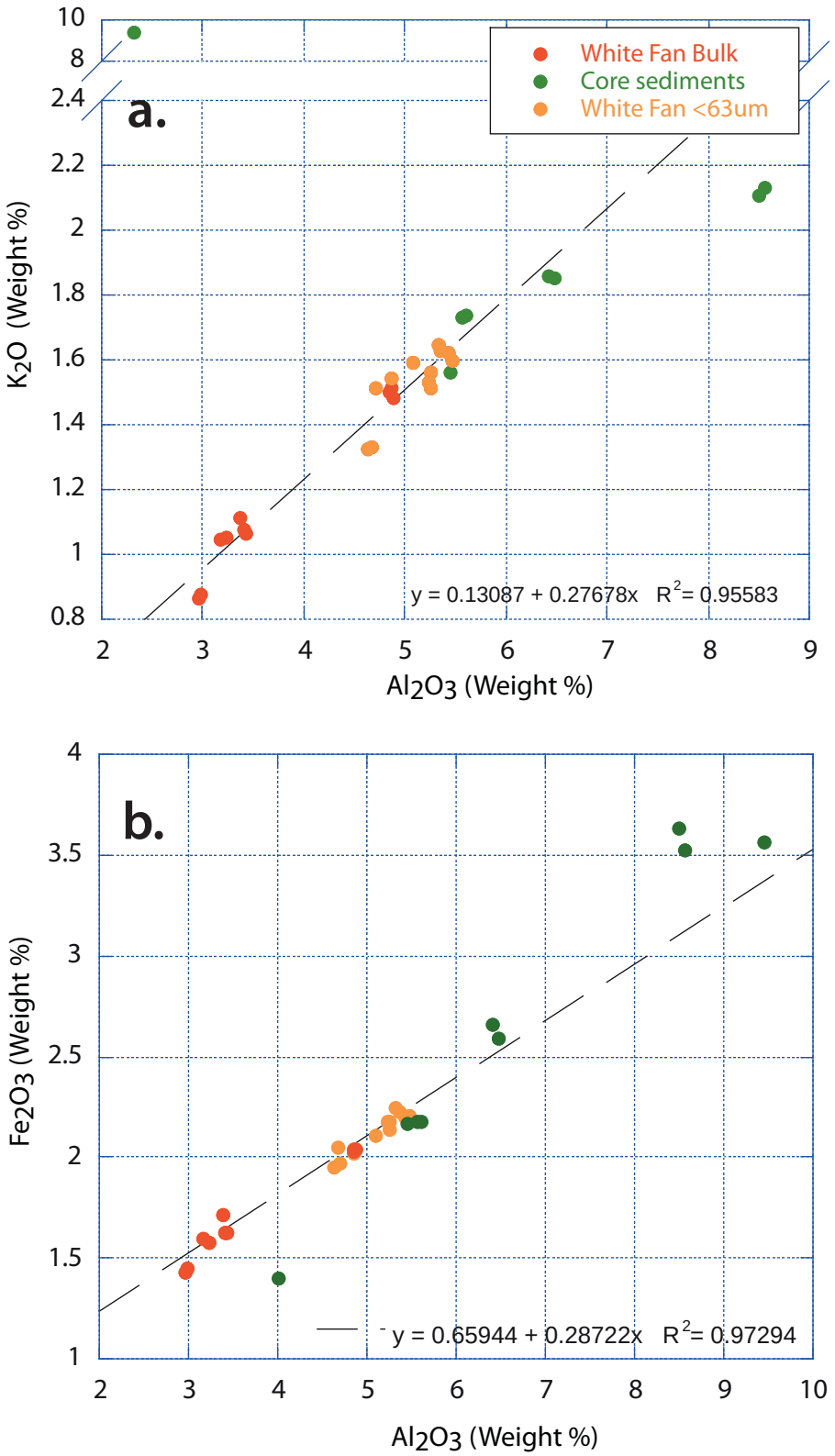

Figure 4.10: Scatterplots demonstrating the strong correlations between MgO and Al2O3, as well as Fe2O3 and Al2O3 in the White Fan, indicating that iron and aluminum originate in the clay minerals. The core sediments (green circles) are plotted for comparison purposes, but not included in the calculation of the correlation coefficient.

Yet if the sedimentation rate for DB-49 follows proposed rates in Kongressvatnet of approximately 0.47 mm annually (Guillizzoni et al., 2006), the 0.5 mm resolution of the ITRAX Scanning XRF analysis would not resolve such fine-scale sub-annual trends. Magnetic susceptibility correlation of DB-49 with the Guilizzoni et al. (2006) cores indicate that the cores analyzed in the present study have a slightly higher sedimentation rate, which could plausibly allow for sub-annual resolution of chemical variations in some regions of the core (Figure 4.8).

In a small-scale study, Johnson (2001) found analogous chemical variations in thin sections of Kongressvatnet core sediments using SEM and EDAX Genesis analysis. This study revealed similar results in alternating coarse, calcium and magnesium rich laminations with fine-grained, silica and aluminum rich layers (Johnson, 2001). From these results, Johnson (2001) concluded that Kongressvatnet sediments are chemically varved: the calcium and magnesium laminations are the result of coarse-grained detrital dolomitic summer input, while the alumino-silicate rich layers reflect winter deposition of clays.

4.3.1.a Bacterially mediated dolomite precipitation

The presence of chemical varves is likely influenced by the activity of the sulfate reducing bacteria and may reflect the input of organic material into Kongressvatnet. Preliminary SEM-EDS analysis of the core sediments reveals the presence of small euhedral Mg-rich cacite, and dolomite rhombohedra ranging in size from 1 μm to 10 μm (Figure 3.21). The euhedral shape and well-developed crystal faces of the rhombs suggest direct precipitate or an authogenic rather than detrital origin (Del Cura et al., 2001; Rosen and Coshell, 1992). SEM analysis further reveals the intergrowth of several rhombs, indicating multiple growth episodes and therefore an authogenic origin for the crystallites (Figure 3.21a) (Del Cura et al., 2001; Rosen

and Coshell, 1992). In her study of Kongressvatnet cores, Alden (2006) noted that the lake sediment carbonate index was greater than either of the fans (0.65-0.85 for core sediment compared to values less than 0.65 for fan sediment). This further supports the direct precipitation of carbonate from the water column.

Primary dolomite is not thought to form in low temperature environments due to kinetic inhibition (Arvidson and Mackenzie, 1999). Laboratory experiments of dolomite precipitation require temperatures exceeding 100°C to successfully produce crystal growth (Burns et al., 2000; Arvidson and Mackenzie, 1999). Computer modeling of dolomite precipitation at temperatures of 25°C indicates that even at relatively high concentrations of magnesium (0.05M), dolomite may require ~10 years to precipitate (Arvidson and Mackenzie, 1999).

However, primary dolomite formation could be stimulated by sulfate-reducing bacteria present in the anoxic waters below the chemocline in Kongressvatnet (Guilizzoni et al., 2006; Bøyum and Kjensmo, 1970). In oxic waters, the ionic association between Mg^{2+} and SO_4^{2-} reduces the activity of magnesium and thus its availability for dolomite formation (Burns et al., 2000). Yet in anoxic waters, the sulfate-reducing bacteria metabolically remove SO_4^{2-}, effectively releasing Mg^{2+} and in the process produce HCO^{3-} from reactions with organic material (Burns et al., 2000). This process optimizes conditions for dolomite precipitation.

Sulfate is abundant due to the presence of the sulfate-rich stream entering the lake from the north, and thus the sulfate-reducing bacteria productivity is limited only by organic input (Bøyum and Kjensmo, 1970). Accordingly, bacterial productivity and thus dolomite formation should increase during the summer or during extended ice-free periods and decrease during the winter and extended cold periods. As such, the aforementioned chemical varving observed in the scanning XRF analysis and previous SEM analysis of thin-sections of Kongressvatnet cores

(Johnston, 2001) is evidence of dolomite precipitation directly from the lake water rather than as a detrital sediment.

4.3.1.b Pyrite precipitation

Iron and sulfur strongly correlate throughout the upper 390 mm of the core sediments (r^2 = 0.51). The anomalous peaks in iron below 300 mm coincide only with peaks in sulfur and Mn but are not coincident with any other element, suggesting the precipitation of pyrite (Figure 3.19). Preliminary SEM-EDS analysis reveals the presence of pyrite framboids and one area of cuboidal iron-sulfides, associated with what appears to be organic material. Previous studies of Kongress note the presence of similar iron-sulfide framboids throughout the core sediments (Guillizzoni et al., 2006).

The activity of sulfate reducing bacteria previously documented in Kongressvatnet, influences the formation of iron sulfides by providing reduced sulfide species to react with iron (Berner, 1985; Langmur, 1997; Neumann et al., 2005) (Figure 4.11). The iron-rich, gelatinous, black sediments that form the top 20 mm to 30 mm of most cores collected from Kongress (Alden, 2007, Guillizzoni et al., 2006, Johnston, 2007; Van Der Bilt, 2009), are characteristic of the early stages of pyrite precipitation in which iron species react with the bacterially reduced sulfur, forming iron monosulfides (Neumann et al., 2005). Burial of the iron monosulfides and subsequent downward diffusion of a more oxidized aqueous sulfur species (H_2S or HS^-) completes the pyritization process, and is evident in a reduction of the black coloring observed near the sediment water interface (Neuman et al., 2005 cites Berner, 1970; Sternbeck and Sohlenius, 1997). Preservation of these black layers lower in the core may indicate prolonged

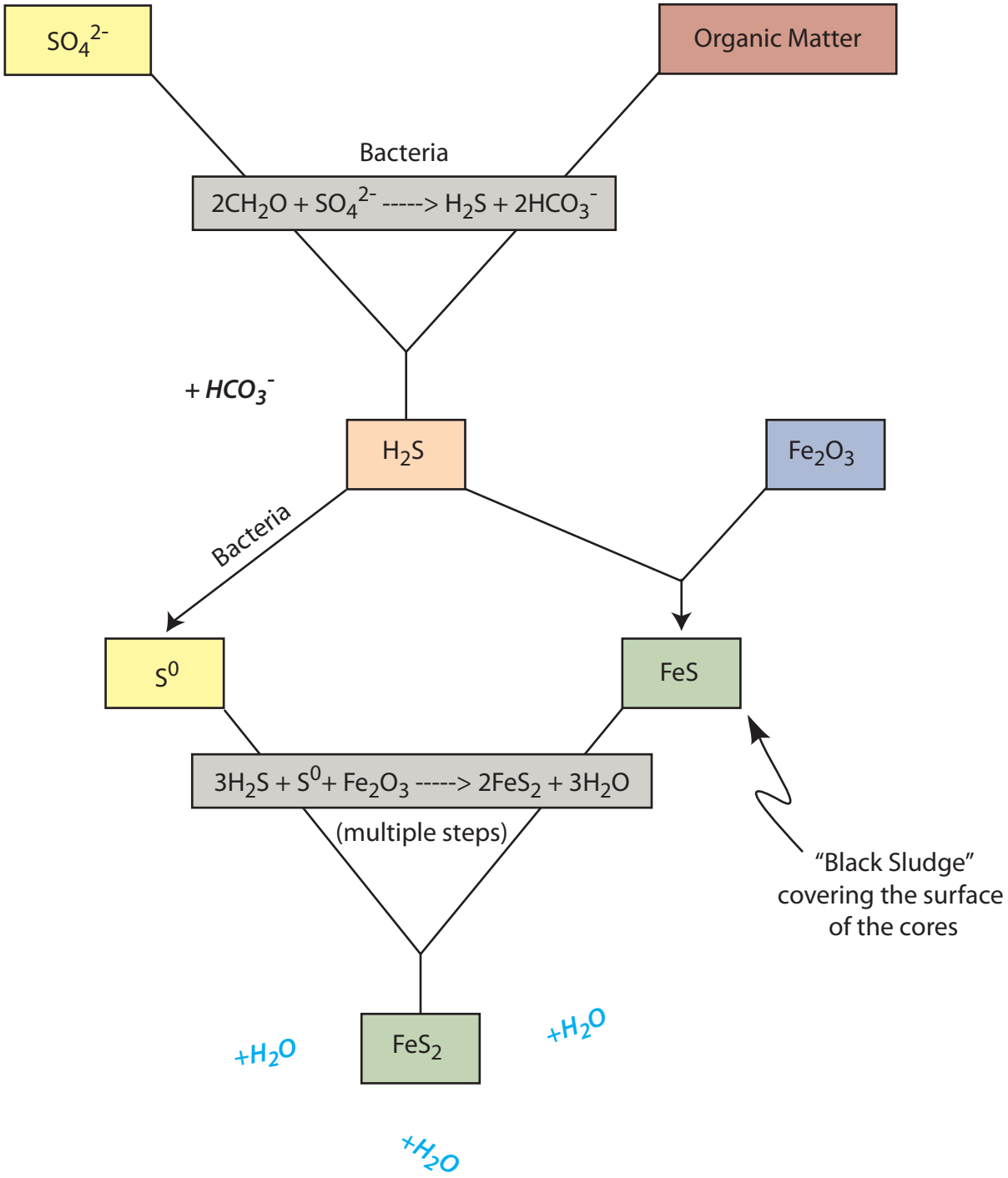

Figure 4.11. Pyrite reduction scheme illustrating the role of sulfate reduction in the precipitation of pyrite. Balanced reaction equations are highlighted in the gray boxes.

periods of reduction in which no oxidized aqueous sulfur species were available to complete the pyritization process.

The abundance of sulfate below the chemocline indicates that pyrite precipitation in Kongressvatent is likely limited by the availability of organic matter and reactive iron species from terrigenous material (Berner, 1984). Therefore, similar to dolomite, precipitation of iron may reflect warmer periods, which result in increased terrigenous organic inflow.

Despite these observations, cyclic peaks in iron and sulfur commonly coincide with the deposition of the clay materials, interpreted to represent the winter layers of the seasonal varves, which are deposited during periods of very little terriginous organic input into the lake. However, the observed correlation may be the result of dilution from relatively high sedimentation rates during the spring and summer melt. Hence the formation of iron sulfides, although occurring during the summer, is not expressed until the sedimentation rates reduce during the winter.

4.3.2 Climactic Influences on Core Chemistry

The annual chemical varves of the deep basin core are overprinted by larger fluctuations in chemical composition. In her study of chemical varves in Kongressvatnet sediments, Johnson (2001) notes that the "best" sample from the set of thin sections was selected for study, alluding to the fact that the trends are not evident throughout the core. These interruptions of the rhythmically laminated sediments suggest that factors other than annual coupling of coarse and fine-grained sediments influence the chemistry of the lake cores. The iron peaks in the lower sections and calcium peaks in the upper sections of the core are the most notable changes

observed in sediment chemistry and will be the focus for interpretations of climatic influences on sediment deposition.

4.3.2.a Pyrite precipitation during the Medieval Warm Period

The largest peaks in iron and sulfur occur between 300-400 mm depth and may reflect a period of significantly warmer climate. These peaks coincide with a strong peak in manganese, a common indicator of reducing conditions (Figure 3.19). In anoxic waters, manganese exists in the form, Mn^{2+}, which readily substitutes in the calcite crystal lattice for Ca^{2+} or in dolomite for Mg^{2+} (Sternbeck and Sohlenius, 1998). Under anoxic conditions, high alkalinity from sulfate reducing bacteria activity and the concentration of Mn^{2+} in the pore water results in the precipitation of manganese in the form of mixed Mn-Ca carbonates such as rhodochrosite [$MnCO_3$] and Kutnahorite [$CaMn(CO_3)_2$] (Jackson and Barak, 2005; Sternbeck and Sohlenius, 1998). Thus the simultaneous peaks in manganese and iron between 300-400 mm, suggest a period of elevated organic input in the lake, spurring activity of the sulfate reducing bacteria and the deposition of mixed Mn-Ca carbonates and pyrite.

Magnetic susceptibility correlations of the deep basin core (DB-49) with the core analyzed by Guilizzoni et al. (2006) indicate that the high iron, sulfur, and manganese peaks were deposited between approximately 800 AD and 1100 AD (Figure 4.8). Peaks in iron and sulfur coincide with the sediment in the Guilizzoni et al. (2006) cores deposited during the Medieval Warm Period, an episode of rapid warming that occurred between the 9th and the 14th centuries (Hunt, 1998). A mesotrophic assemblage of diatoms such as *Fragilaria crotonensis, Tabellaria flocculosa,* and *Synedra tenera* characterizes this section of the core, indicating a period of warmer climate (Guillizzoni et al., 2006). This correlation corroborates the proposed

deposition of pyrite and reduced sulfides in Kongressvatnet due to the development of strongly reducing conditions during warm periods.

4.3.2.b Little Ice Age calcite precipitation

The annual chemical changes in the deep basin core are also overprinted by centimeter scale, massive laminations of light gray material characterized by considerable increases in x-ray density and calcium concentrations. These high-calcium layers often do not contain any internal structure or laminations. Alden (2006) noted similar massive layers in her study of Kongressvatnet core sediments between 51-57 mm, 109-130 mm, and 225-231 mm (compared to depths of 30-42 mm, 99-111 mm, and 195-205 mm observed in DB-49). Based on Cs/Pb dating, Alden determined that the uppermost massive lamination (51-57 mm) was deposited in 0.69 years, and she suggested that these layers represent turbidites (Alden, 2006).

Although detailed grain size analysis is not available for the core sediments, these layers appear to be horizons that are finer than those occurring above and below this calcium-rich layer. If the sediments were derived from the upper basin located proximal to the inlet of the White Fan, as Alden suggests, the "turbidite" sediments would be expected to be graded and coarser than the sediments deposited into the distal deep basin (Cojan, 2002).

An alternative hypothesis is that these layers represent periods of rapid calcite precipitation from the lower part of the water column. Although only two samples were analyzed using SEM-EDS, calcite formed in layers of distinct micron-scale euhedral rhombs, suggesting the formation of primary calcite (Figure 3.21). Many factors influence the morphology of precipitated calcite grains including the calcite saturation index [$\log(IAP/K_{cal})$], bacterial mediation, rate of formation, and the presence of organic compounds or inhibiting ions

such as sulfate and phosphate (Bosak and Newman, 2005). Consequently, calcite may precipitate in a variety of crystal shapes including elongate fibrous needles, equaint rhombohedra, and scalene rhombohedra (known as "dogtooth spar") (Bosak and Newman, 2005; Lacelle, 2007).

Preliminary precipitation models of the H_2CO_3–HCO_3^-–CO_3^{2-} equilibrium systems using Kongress water chemistry indicate that the water below the chemocline is supersaturated with respect to calcite. During the 2006 summer field season, water samples were collected every 2 m and analyzed for major cations (Na^+, K^+, Mg^{2+}, and Ca^{2+}), anions (Cl^-, SO_4^{2-}), and pH (Holm, T.M., personal communication, 2008). Alkalinity was not directly measured but can be estimated from the difference between the sum of the base cations (C_B) and the sum of the acid anions (C_A) (Equation 4.2).

$$Alkalinity = C_B - C_A \qquad (4.2)$$

From these values the activity of each species in solution was calculated using the Debye-Hückel equation (Equation 4.3).

$$\log(\gamma_i) = \frac{-Az_i^2\sqrt{I}}{1 + Ba_i\sqrt{I}} \qquad (4.3)$$

Where m_i is the molarity and z_i is the charge of each ion (i). B and A are constants selected for a temperature of ~2.5°C and 1 bar pressure and a_i is a constant describing the hydrated radius of each species (Eby, 2004). The carbonate equilibrium system in Kongress was modeled for temperatures of 3°C, 6°C, and 9°C based on a series of equations derived from the dissolution of calcite and the carbonate equilibrium system (modified from Drever, 1997) (Equations 4.4-4.18).

$$CaCO_3 \rightleftharpoons Ca^{2+} + CO_3^{2-} \qquad K_{cal} = a_{Ca^{2+}} a_{CO_3^{2-}}{}^{d} \qquad (4.4)$$

[d] *a* indicates the activity of the species.

$$CO_2 + H_2O \rightleftharpoons H_2CO_3 \qquad K_{CO2} = \frac{a_{H_2CO_3}}{P_{CO_2}} \qquad (4.5)$$

$$H_2CO_3 \rightleftharpoons H^+ + HCO_3^- \qquad K_1 = \frac{a_{H^+} a_{HCO_3^-}}{a_{H_2CO_3}} \qquad (4.6)$$

$$a_{H^+} = \frac{K_1 a_{H_2CO_3}}{a_{HCO_3^-}} \qquad (4.7)$$

$$HCO_3^- \rightleftharpoons H^+ + CO_3^{2-} \qquad K_2 = \frac{a_{H^+} a_{CO_3^{2-}}}{a_{HCO_3^-}} \qquad (4.8)$$

$$a_{CO_3^{2-}} = \frac{K_2 a_{HCO_3^-}}{a_{H^+}} \qquad (4.9)$$

Substitute equation (4.7) into (4.9)

$$a_{CO_3^{2-}} = \frac{K_2 a^2_{HCO_3^-}}{K_1 a_{H_2CO_3}} \qquad (4.10)$$

Substitute equation (4.10) into (4.4)

$$K_{cal} = a_{Ca^{2+}} \frac{K_2 a^2_{HCO_3^-}}{K_1 a_{H_2CO_3}} \qquad (4.11)$$

$$\frac{K_{cal} K_1}{K_2} = \frac{a_{Ca^{2+}} a^2_{HCO_3^-}}{a_{H_2CO_3}} \qquad (4.12)$$

Substitute equation (4.5) into (4.12)

$$\frac{K_{CO_2} K_{cal} K_1}{K_2} = \frac{a_{Ca^{2+}} a^2_{HCO_3^-}}{P_{CO_2}} \qquad (4.13)$$

Charge balance equation:

$$\left[H^+\right] + 2\left[Ca^{2+}\right] = \left[HCO_3^{2-}\right] + 2\left[CO_3^{2-}\right] + \left[OH^-\right] \qquad (4.14)$$

Since the pH of Kongress is less than 9, $[H^+]$, $[CO_3^{2-}]$, $[OH^-]$ are negligible, simplifying equation 4.12

$$2\left[Ca^{2+}\right] = \left[HCO_3^{2-}\right] \qquad (4.15)$$

$$\frac{2a_{ca^{2+}}}{\gamma_{Ca^{2+}}} = \frac{a_{HCO_3^-}}{\gamma_{HCO_3^-}} \qquad (4.16)$$

$$a_{HCO_3^-} = 2a_{Ca^{2+}} \frac{\gamma_{HCO_3^-}}{\gamma_{Ca^{2+}}} \qquad (4.17)$$

Substituting equation 4.17 into 4.13

$$\left(a_{Ca^{2+}}\right)^3 = \frac{K_{cal} * K_1 * K_{CO2} * P_{CO2}(\gamma_{Ca^{2+}})^2}{4(\gamma_{HCO_3^-})^2 * K_2} \qquad (4.18)$$

Using equation 4.16, the model was calculated relating the activity of calcium concentration to the P_{CO2} of the water. The values for all the equilibrium constants (K) are adjusted for temperature (**Table 1**). Since data for the P_{CO2} of Kongressvatnet was not available, P_{CO2} was estimated based on the temperature, pH, and the calculated alkalinity (Equation 4.19).

Equilibrium Constant	**25 °C**	**3 °C**	**6 °C**	**9 °C**
K_1	$4.47*10^{-7}$	$3.34*10^{-7}$	$3.48*10^{-7}$	$3.63*10^{-7}$
K_2	$4.68*10^{-11}$	$2.93*10^{-11}$	$3.14*10^{-11}$	$3.36*10^{-11}$
K_{CO2}	$3.39*10^{-2}$	$1.80*10^{-2}$	$1.97*10^{-2}$	$2.16*10^{-2}$
K_{cal}	$3.31*10^{-9}$	$4.68*10^{-9}$	$4.45*10^{-9}$	$4.24*10^{-9}$
K_w	$1.00*10^{-14}$	$1.67*10^{-15}$	$2.17*10^{-15}$	$2.81*10^{-15}$

Table 1: Equilibrium constants used to calculate the solubility model for calcite at 25 °C and adjusted values at 3 °C, 6 °C, and 9 °C.

$$P_{CO_2} = \frac{[H_2CO_3]}{K_{CO_2}} = \frac{[H^+][HCO_3^-]}{Ka_1 * K_{CO_2}} \qquad (4.19)$$

A comparison of the calculated activities to the modeled calcite solubility indicates that the lakewater becomes supersaturated with respect to calcite below the chemocline, suggesting

that below approximately 45 m depth, calcite precipitation is possible (Figure 4.11). However, this model is only a rough estimate of the true calcite equilibrium system for Kongressvatnet since both alkalinity and P_{CO2} were calculated rather than directly measured. The development of a more accurate model for the calcite equilibrium system necessitates additional analyses of the water column.

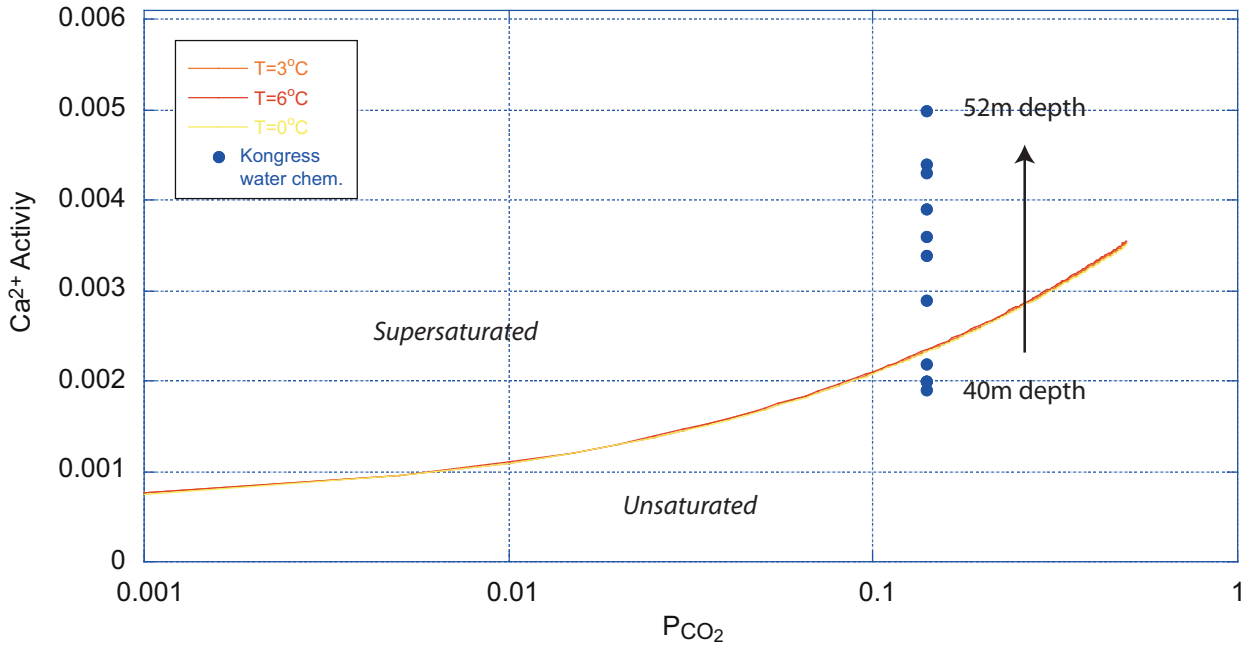

Figure 4.12: Model calculated for the activity of calcium in equilibrium with calcite as a function of P_{CO2} in Kongressvatnet. The equilibrium is plotted at 3 different temperatures, yet does not significantly affect the model. The activity of calcium in Kongress lake waters is plotted for samples 40-52 m depth at a calculated value for P_{CO2}. The points that fall below the equilibrium line are not saturated with respect to calcite, whereas the points above the equilibrium line indicate supersaturated conditions.

Although the waters are saturated enough to precipitate calcite below the chemocline, the lack of equilibrium between the ionic species and the precipitated minerals reflect outside influences on the carbonate equilibrium system. The common ion effect occurs due to the dissolution of several mineral species in natural waters that contain at least one common ion (Langmur, 1997). In Kongressvatnet, dissolution of the Gipshuken Formation saturates the lake water with respect to calcite. Inflow from the sulfurous northern stream containing dissolved

gypsum, results in supersaturation of the lake with respect to calcite and may result in calcite precipitation (Langmur, 1997) (Equation 4.20).

$$CaSO_4 \bullet H_2O(gypsum) + 2HCO_3^- \rightarrow CaCO_3(calcite) + SO_4^{2-} + 2H_2O + CO_2 \qquad (4.20)$$

However, calcite precipitation is inhibition by the presence of organic matter (Langmur, 1997). Inskeep and Bloom (1986) conducted laboratory experiments that demonstrated that the presence of soluble soil organic matter in the form of 0.15mM of water-soil extract (WSE) and 0.028mM of Seward fuluvic acid (FA) significantly inhibited the precipitation of calcite on seed crystals. Thus, periods of low organic input into Kongressvatnet, such as during the Little Ice Age, could cause episodic events of calcite precipitation, which may be the source of the inverse relationship between carbonate and organic content previously observed in the Kongressvatnet cores (Alden, 2006 and van der Bilt, 2009).

4.3.2.c Cryogenic calcite

The calcium-rich layers in the core sediments could alternatively result from thick ice cover during prolonged cold periods. The elution of ions from lake ice, concentrates the underlying water and may result in the precipitation of calcite near the water/ice interface. The presence of the ice shields the lake surface from wind interactions, which inhibits circulation and reduces the high temperature of the surface waters that produce the summer thermocline, potentially increasing the stratification of the upper water column and preventing circulation of the eluted ions to lower depths.

Many previous studies have documented a similar mechanism for calcite precipitation in Polar Regions throughout the Northern Hemisphere and have coined the term, “cryogenic calcite” (Lacelle, 2006). Cryogenic calcite commonly forms in cave environments, but has also

been documented to form as subglacial deposits and within aufeis, or icings that accumulate over perennially frozen river channels (Lacelle, 2007). Laboratory modeling of the production of cryogenic calcite indicates that despite increases in P_{CO2} as temperature drops, the calcite saturation index may increase enough to promote precipitation (Killawee et al., 1998).

Guillizzoni et al. (2006) determined calcite and dolomite abundance using X-Ray Diffractometry. Based on magnetic susceptibility correlations, the peaks in calcium concentration of DB-49 correspond to regions of elevated calcite concentrations in the Guillizzoni et al. (2006) cores, despite a dominance of dolomite throughout the rest of the core (Figure 4.12). This zone is interpreted to represent the peak of the Little Ice Age due to the absence of planktonic diatoms and an *S. construens*, which indicate oligotrophic conditions and low water levels (Guillizzoni et al., 2006). Low bacterial pigment abundance (isorenieratene and okenone) and low concentrations of lutein or chlorophyll derivatives in this section of the core, further reflect limited vegetation transported into the lake (Guillizzoni et al., 2006).

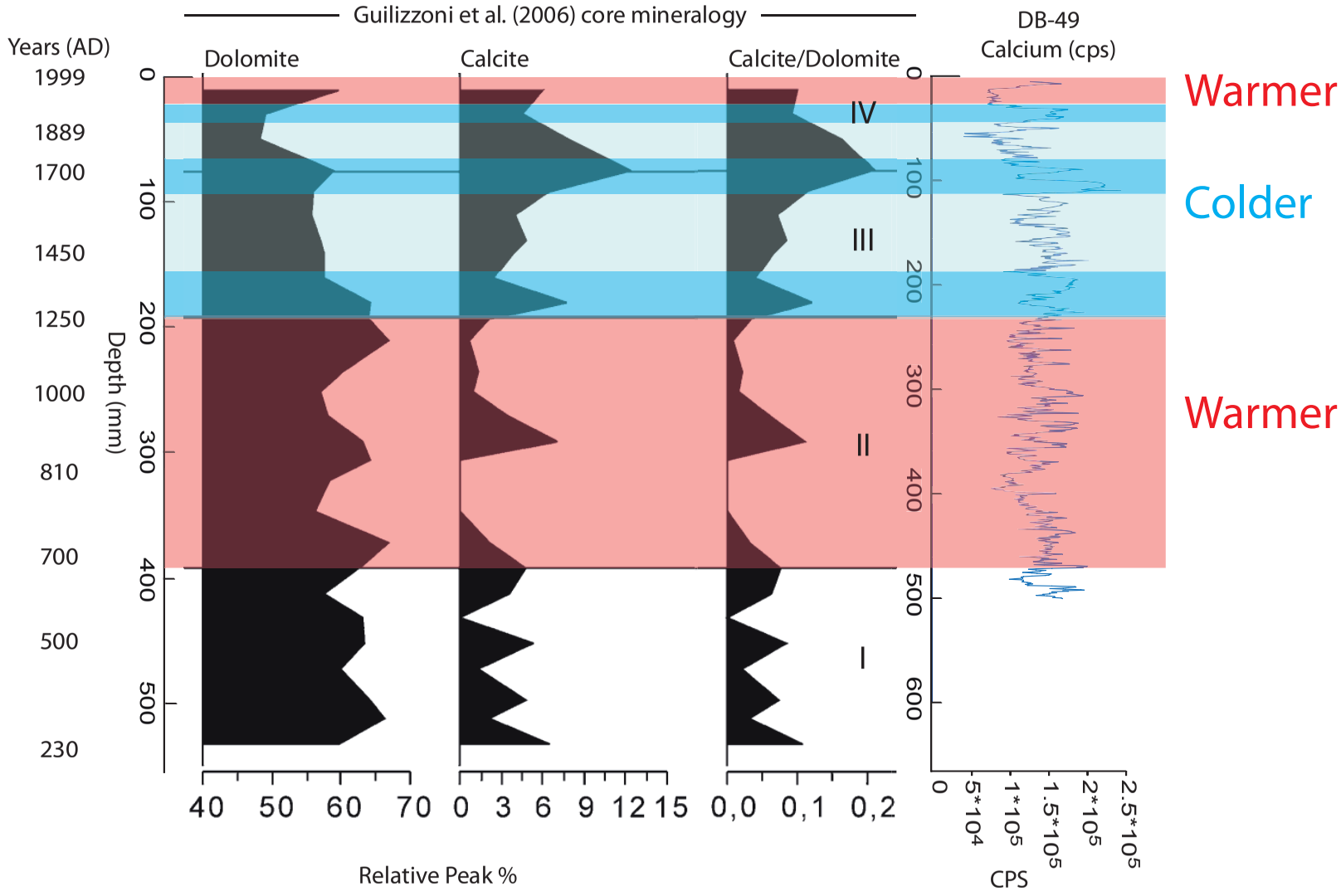

Figure 4.13. Correlation of calcium concentration for DB-49 with the chemistry of the Guilizzoni et al. (2006) core sediments. The roman numerals indicate zones designated by Guilizzoni et al. (2006) marking proposed changes in climate regime. Zone II corresponds to the Medieval Warm Period, zone III indicates the peak of the Little Ice Age, and Zone I represents the transition from the cold LIA conditions to the current warm conditions. The colors reflect the periods of warm (red) or cold (blue) climate. The periods of high calcite precipitation in DB-49 are highlighted in dark blue.

Based on the average chemistry in 2006 of the upper water column, a model was used to determine if precipitation of calcite due to the freezing of lake ice is plausible. Assuming that the upper 2 m of the lake freeze during the winter, the volume of water to 2 m depth was calculated based on GIS analysis of the Kongressvatnet bathymetry (Table 2). This volume was then used to determine the concentration of ions eluted during formation of lake ice (Table 3). These calculations reveal that if the eluted ions remain in the upper 1 m of the lake, the average activity of calcium is 3.1 mM, resulting in supersaturation with respect to calcite at a P_{CO2} of 0.14 atm (estimated based on temperature and pH**;** Equation 4.19) (Figure 4.13). However if the ions diffuse past 2 m depth, the average activity of calcite is 2.1 mM, indicating that the lake is no longer supersaturated with respect to calcite at the same P_{CO2}. Changing P_{CO2} and ion diffusion depths will influence the precipitation of cryogenic calcite, thus further study is required to prove or disprove this hypothesis.

Lake volume 0-2m (L)	$1.04*10^9$
Lake volume 2-2.5 m (L)	$2.44*10^8$
Lake volume 2-3 m (L)	$4.87*10^8$
Lake volume 2-4 m (L)	$9.53*10^8$

Table 2: Volume of Kongressvatnet water at different depths used for calculation of eluted ion concentrations.

[ions] of lake ice ~2 m	Cl	SO4	Na	K	Mg	Ca	Ca Activity
Avg. conc. Kongress waters 0-2 m (mol/L)	1.4E-04	1.6E-03	1.0E-04	5.1E-06	1.5E-04	1.7E-03	1.21E-03
Total ions 0-2m (mol)	1.4E+05	1.7E+06	1.1E+05	5.3E+03	1.6E+05	1.7E+06	

Diffusion to 0.5 m

Avg. conc. Kongress waters at 2 m (mol/L)	1.3E-04	1.6E-03	9.6E-05	5.1E-06	1.2E-04	1.4E-03	
Total ions 2-2.5 m (mol)	3.2E+04	3.8E+05	2.3E+04	1.2E+03	3.0E+04	3.4E+05	
Total ions (mol) = Eluted + 2-2.5 m	1.8E+05	2.1E+06	1.3E+05	6.6E+03	1.9E+05	2.1E+06	
Conc. with 0.5 m diffusion (mol/L)	7.3E-04	8.5E-03	5.3E-04	2.7E-05	7.7E-04	8.5E-03	4.80E-03

Diffusion to 1 m

Avg. conc. 2-4 m (mol/L)	1.3E-04	1.6E-03	9.4E-05	5.1E-06	1.0E-04	1.4E-03	
Total ions 2-3 m (mol)	6.3E+04	7.6E+05	4.6E+04	2.5E+03	5.0E+04	6.9E+05	
Total ions (mol) = Eluted + 2-3 m	2.1E+05	2.5E+06	1.5E+05	7.8E+03	2.1E+05	2.4E+06	
Conc with 1 m diffusion (mol/L)	4.3E-04	5.0E-03	3.1E-04	1.6E-05	4.2E-04	5.0E-03	3.07E-03

Diffusion to 2 m

Avg conc 3-5 m (mol/L)	1.3E-04	1.6E-03	9.4E-05	5.1E-06	1.0E-04	1.4E-03	
Total ions 2-4 m (mol)	1.2E+05	1.5E+06	8.9E+04	4.9E+03	9.8E+04	1.4E+06	
Total ions (mol) = Eluted + 2-4 m	2.7E+05	3.2E+06	1.9E+05	1.0E+04	2.5E+05	3.1E+06	
Conc with 2 m diffusion (mol/L)	2.8E-04	3.3E-03	2.0E-04	1.1E-05	2.7E-04	3.2E-03	2.14E-03

Table 3: Table of calculations used to determine the concentration of the residual water after the formation of lake ice. The moles of eluted ions were calculated based on the volume of the lake 0-2 m and the average concentration of ionic species (row 1-2). This value was used to calculate the average molar concentrations of Kongress lake waters for the diffusion of eluted ions to three different depths (2-2.5 m, 2-3 m, and 2-4m). The resulting calcium concentrations were converted to activities using the Debye-Hückel equation (Appendix 5), and the values are highlighted in blue.

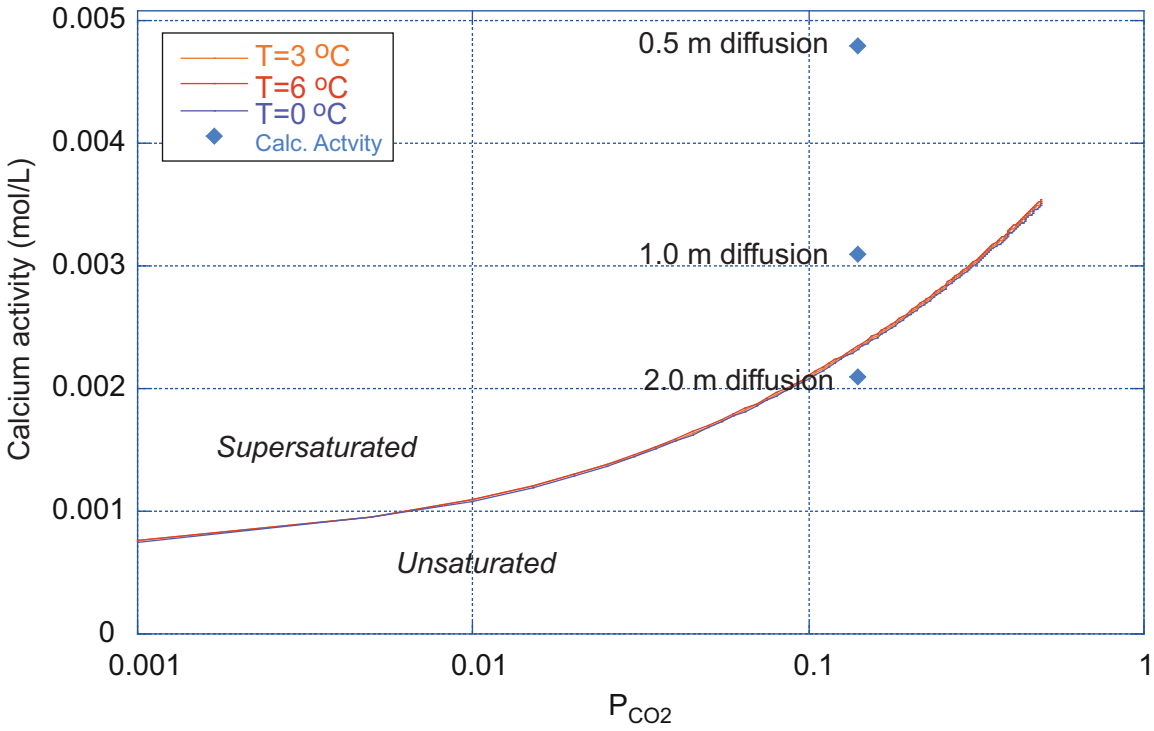

Figure 4.14. Calculated calcium activities after the elution of ions in the formation of lake ice (~2 m ice thickness). The activity of Ca^{+2} is calculated for 3 different diffusion depths of the eluted ions (0.5 m, 1 m, and 2 m). The equilibrium activity of calcium and calcite was plotted at 3 different temperatures, 0 °C, 3 °C, and 6 °C, yet the difference in temperature did not significantly affect the model. Points that fall above the equilibrium line are supersaturated with respect to calcite, while the region below the equilibrium line indicate unsaturated conditions.

One concern with the precipitation of calcite along the water/ice interface is the settling velocity of such small calcite grains, which SEM observations indicate range in size from 2 µm to 10 µm. Stokes' Law was used to calculate the time required for a 10 µm grain to settle to the bottom of a 45 m lake (Garrels and Mackenzie, 1971) (Equation 4.21).

$$V = \left(\frac{2}{9}\right)\left(\frac{(\rho_s - \rho_f) * g * r^2}{\eta}\right) \qquad (4.21)$$

In this equation, g is gravitational acceleration, ρ_s is the density of the solid, ρ_f is the density of fluid, and η is the kinematic viscosity of the fluid (Garrels and Mackenzie, 1971).

Using a density for calcite of 2.715 g/cm^3 (Deer et al., 1975), a water density of 1.00g/cm^3 at 4°C, and a fluid viscosity of $1.6*10^{-3}$ Pa*s at 3°C (Denny, 1993), a 10 μm crystal of calcite settles at a velocity of $5.84*10^{-5}$ m/s and requires approximately 2.4 years to settle to the bottom of the lake (45 m depth).

Although, a 2-year settling period is extremely long for the travel time of one calcite grain, during the peak of the Little Ice Age the lake ice covering Kongressvatnet may have never completely melted (Retelle, M., personal communication, 2009). Thus, the calcite crystals could slowly settle through the water column undisturbed for extended periods.

The long time required for a grain to settle raises the issue of calcite dissolution. While the water below the chemocline is saturated with respect to calcite, the water above is slightly unsaturated at the calculated values of P_{CO2}. Partial dissolution of sediments observed in several regions of the core, which may reflect dissolution of calcite grains during settling through the water column (Figure 3.21f). However, many of the rhombs observed have well-defined edges, suggesting precipitation of the calcite in situ or from the overlying 15 m of water below the chemocline. Therefore, based on the analysis of Kongressvatnet water chemistry, precipitation of cryogenic calcite could plausibly occur. The presence of both euhedral rhombs and partially dissolved crystals, suggests that multiple precipitation mechanisms may be involved in the formation of the calcite rich layers. However, both mechanisms, precipitation below the chemocline or from the upper 1-2 m of the water column support that the calcium-rich laminations in the core sediments indicate periods of cold climate and likely represent sediments deposited during the Little Ice Age.

5. CONCLUSIONS

This thesis addressed two principle hypotheses:

I. *Changes in the chemistry and mineraology of Kongressvatnet lake sediments reflect Late Holocene climate change in this region.*

II. *Mineral weathering products reflect the relative age of the surfaces of meltwater deposits.*

Elemental analysis of the two fans reveals distinct chemical signatures, which confirms the use of chemical composition in determining sediment provenance in Kongressvatnet. The elemental chemistry of the core sediments only resembles that of the White Fan, indicating negligible sediment input from meltwater traveling over the Black Fan. Similar to the White Fan clays, the mineralogic assemblage of the <1 μm core sediment is dominated by discreet smectite and interlayered illite/smectite, further supporting the absence of Black Fan influence. The absence of Black Fan signature in the core suggests Kogressbreen was a cold-based glacier. Contrary to previous studies (Alden, 2007; Anderson, 2007; Guilizzoni et al., 2006), these results indicate that the provenance of sediments in Kongressvatnet cannot be used as a proxy for the onset of the Little Ice Age in Western Spitsbergen.

Although the lake sediments solely originate from the White Fan, the ITRAX Scanning XRF analysis of the cores reveal considerable changes in elemental composition. The results of this study indicate that these changes in chemistry are intimately related to both annual fluctuations in temperature and changes in climate that influence the biogeochemical cycles within the lake. The coupling of carbonate rich layers with iron, potassium, titanium, and silica rich layers suggests chemical varves. The calcium rich layer is deposited from meltwater transporting dolomitic White Fan sediment during the spring melt, together with the formation of primary dolomite, mediated by sulfate-reducing bacteria. The potassium, titanium, iron, and

silica rich layers indicate clastic clay deposition when the lake is ice covered during the winter. The covariance of iron and sulfur with clay deposition indicates the additional influence of bacteria mediated pyrite precipitation. Although this process is likely occurring throughout the year, there is considerable dilution by calcium rich detrital sediment during the summer.

The fine-scale varves are overprinted by large fluctuations in chemistry that result from changes in climate. In the upper 200 mm of the core, large peaks in calcium that correspond to centimeter scale layers with no internal laminations reflect extended cold periods and the precipitation of cryogenic calcite (Figure 5.1a). The discovery of ~10 μm euhedral rhombs with well-defined edges using SEM-EDS, further supports this hypothesis. Magnetic susceptibility correlations of DB-49 to the cores analyzed in the Guilizzoni et al. (2006) study indicate that this section of the core corresponds to the period the authors postulate represents the Little Ice Age.

Peaks in iron in the sections of the core below 300 mm depth, indicate the reduction of iron and the formation of iron sulfides. Since the limiting factor in this process is terriginous organic material and reactive iron species, the large peaks in iron and sulfur likely represent periods of warm climate when more organic material was available (Figure 5.1b). Magnetic susceptibility correlations with the Guillizzoni et al. (2006) cores indicate that the high-iron sections correspond to the Medieval Warm Period, further corroborating this hypothesis.

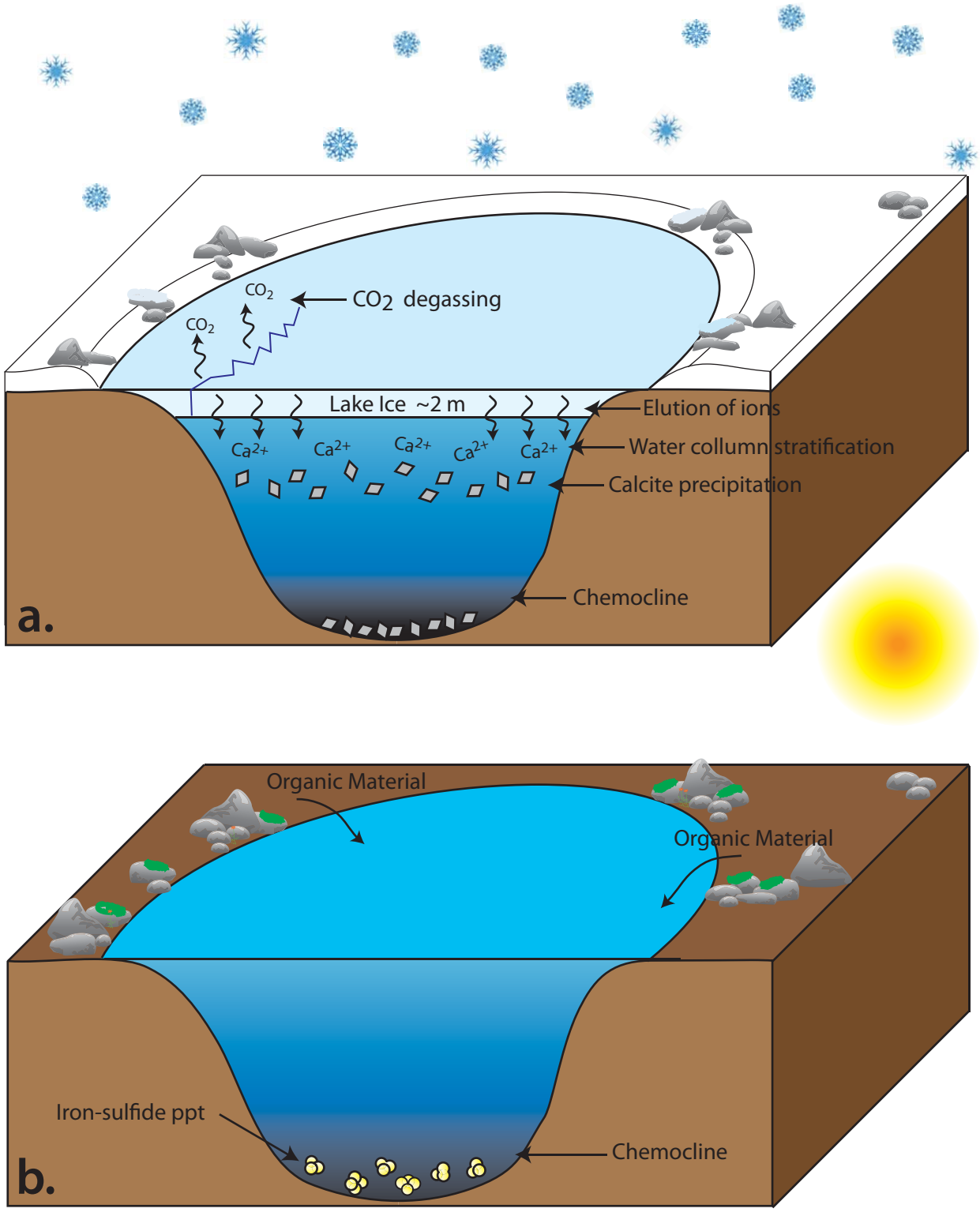

5.1 Model of the proposed impacts of climate on the lake sediment chemistry. a. Formation of lake ice causes the elution of ions into the underlying water column and precipitation of carbonate species. Extended periods of ice cover allows for the precipitated carbonate to settle through the water collumn, forming massive calcite-rich layers in the core. b. Periods of warm temperature induce elevated organic input into the lake, spurring the activity of sulfur-reducing bacteria and thus the formation of abundant iron sulfides.

The results additionally support the second principle hypothesis posed in this study. High concentrations of discreet chloritized vermiculite relative to interstratified vermiculite/illite in the raised debris flow lobes between the two primary channels of the Black Fan indicate at least two distinct periods of fan deposition in Kongressdalen. The debris flow lobes were likely deposited during the Late Weschelian (30 ka) or the Younger Dryas (11.5 ka) glacial retreat. The meltwater from Kongressbreen during the Little Ice Age subsequently carved channels through these deposits and formed the Black Fan.

6. FUTURE STUDY

In order to further probe the correlation between the climate and the processes controlling the sediments in Kongressvatnet, an accurate method of dating the cores must be developed. Current studies in paleomagnetic correlations and tephra calibrations appear to be promising dating methods (Schupack, B., pers. comm., 2009; Mortazavi, E., pers. comm., 2009).

Future SEM analysis of the Kongressvatnet core sediments should focus on the morphologic changes in calcite and dolomite throughout the core as well as sediments collected in sediment traps at varying depths in the lake. The morphology of precipitated euhedral grains may reveal important information about the rates of mineral precipitation and concentration of the precipitating waters. This information would further elucidate the controls of climate on the deposition of sediment in Kongressvatnet and aid in refining the proposed modes of deposition.

Further attention may also be directed toward the mineralogy of the clay deposited into the lake. The influence of the lake chemistry on post-depositional diagenesis of the clays may yield information on the formation of the chemocline as well as the processes currently occurring in the bottom waters of Kongressvatnet.

Dating of the raised debris flows of the Black Fan is another promising opportunity for future study. The possibility of Younger Dryas deposition of these sediments suggests such a study could reveal significant information about the extent of glacial advance on Svalbard during this time.

7. REFERENCES

Åberg, G., Lundquist, J., Saarnisto, M. (1995). "Provenance and Weathering Depth of Carbonaceous Gotland Sandstone by use of Carbon and Oxygen Isotopes." *Atmospheric Environment*, 29.7: 781-9.

Aga, O.J. (ed.) (1986). *The Geological History of Svalbard*. Stavanger, Statoil, 121

Akerman, J. (1980). "Studies on Periglacial Geomorphology in West Spitsbergen." Department of Geology. The Royal University of Lund, Sweden.

Alden, C. (2007). *"Glacial History of the Little Ice Age in Kongress Valley, Svalbard: a study of lacustrine sediment."* Senior thesis, Colorado College Department of Geology.

Alley, R. B. (2000). "The Younger Dryas Cold Interval as Viewed from Central Greenland." *Quaternary Sciences Reviews*, 19.1-5: 213-26.

Amorosi, A., Sammartino, I.,Tateo, F. (2007). "Evolution Patterns of Glaucony Maturity: A Mineralogical and Geochemical Approach." *Deep Sea Research Part II: Topical Studies in Oceanography*, 54.11-13: 1364-74

Andersen, B.G., Lundqvist, J., Saarnisto, M. (1995). "The Younger Dryas Margin of the Scandinavian Ice Sheet — an Introduction." *Quaternary International*, 28: 145-6.

Anderson, L. (2007). "*Surficial Geology of the Kongressvatnet Catchment, Svalbard, Norway."* Senior Honors thesis, Montana State University.

Appleby, P. G. (2004) "Environmental Change and Atmospheric Contamination on Svalbard: Sediment Chronology." *Journal of Paleolimnology,* 31.4: 433-43.

Baker, P.A., Kastner, M.(1981). "Constraints on the Formation of Sedimentary Dolomite." *Science*, 213.4504: 214-6.

Bergaya, F., Theng, B. K. G., Lagaly, G. (2006). *Handbook of Clay Science.* Amsterdam; London: Elsevier.

Bergh, S. G.; Maher, H. D. Jr., Braathen, A. ed., (2000). *Tertiary Divergent Thrust Directions from Partitioned Transpression, Broggerhalvoya, Spitsbergen.* Vol. 80. Norway: Taylor & Francis : Oslo, Norway.

Berner, R. A., Leeuw, J.W.De, Spiro, B., Murchison, D.G., Eglington, G. (1985) "Sulphate Reduction, Organic Matter Decomposition and Pyrite Formation [and

Discussion]." *Philosophical Transactions of the Royal Society of London.Series A, Mathematical and Physical Sciences, 315.1531: Geochemistry of Buried Sediments,* 25-38.

Berner, R. A. (1970). "Sedimentary Pyrite Formation." *American Journal of Science,* 268.1: 1-23.

---. (1984). "Sedimentary Pyrite Formation: An Update." *Geochimica et Cosmochimica Acta,* 48.4: 605-15.

Birks, H. J. B., Jones, V. J., Rose, N. L. (2004). "Recent Environmental Change and Atmospheric Contamination on Svalbard as Recorded in Lake Sediments: Synthesis and General Conclusions." *Journal of Paleolimnology,* 31.4: 531-46.

Birks, H., Birks, H. (2006). "Multi-Proxy Studies in Palaeolimnology." *Vegetation History and Archaeobotany,* 15.4: 235-51.

Borchardt, G., Dixon, J.B., Weed, S.B., (ed.) (1989)., Chapt 14: Smectites. *Minerals in Soil Environments (2nd ed.),* 675-727.

Bosak, Tanja, Newman, Dianne K. (2005). “Microbial Kinetic Controls on Calcite Morphology in Supersaturated Solutions” *Journal of Sedimentary Research.* 75: 190-199.

Boulton, G. S. (1972). "Modern Arctic Glaciers as Depositional Models for Former Ice Sheets." *Journal of the Geological Society,* 128.4: 361-93.

Boyle, J. F., Rose, N. L., Appleby, P. G., Birks, H. J. B. (2004). "Recent Environmental Change and Human Impact on Svalbard: The Lake-Sediment Geochemical Record." *Journal of Paleolimnology,* 31.4: 515-30.

Bøyum, A., Johannes, K. (1970). "Kongressvatn. A Creogenic Meromictic Lake at Western Spitsbergen." *Archiv fuer Hydrobiologie,* 67.4: 542-52.
Braissant, O., Decho, A. W., Dupraz, C., Glunk, C., Przekop, K. M., Visscher, P.T. (2007). "Exopolymeric Substances of Sulfate-Reducing Bacteria: Interactions with Calcium at Alkaline pH and Implication for Formation of Carbonate Minerals." *Geobiology*, 5.4: 401-411.

Braathen, A., Bergh, S., Maher, H. D., Jr. (1997). "Thrust Kinematics in the Central Part of the Tertiary Transpressional Fold-Thrust Belt in Spitsbergen." *NGU Bulletin*, 433: 32

Cojan, I., and Renard, M. (2002). *Sedimentology*. Taylor & Francis, Inc.

Cutbill, J. L., Challinor, A.. (1965). "Revisions of the Stratigraphical Scheme for the Carboniferous and Permian Rocks of Spitsbergen and Bjornoya." *Geology Magazine*, 102.5: 419-440.

Deer, W. A., Howie, R. A., Zussman, J. (1975). *An Introduction to the Rock Forming Minerals*. Longman Group Limited. London.

Drever, J. I., Hurcomb, D. R. (1986). "Neutralization of Atmospheric Acidity by Chemical Weathering in an Alpine Drainage Basin in the North Cascade Mountains." *Geology*, 14.3: 221-4.

Dypvik, H., Harris, N. B. (2001). "Geochemical Facies Analysis of Fine-Grained Siliciclastics using Th/U, Zr/Rb and (Zr+Rb)/Sr Ratios." *Chemical Geology*, 181.1-4: 131-46.

Egli, M., Mirabella, A., Sartori, G. (2008). "The Role of Climate and Vegetation in Weathering and Clay Mineral Formation in Late Quaternary Soils of the Swiss and Italian Alps." *Geomorphology*, 102.3-4: 307-24.

Eusterhues, K., Heinrichs, H., Schneider, J. (2005). "Geochemical Response on Redox Fluctuations in Holocene Lake Sediments, Lake Steisslingen, Southern Germany." *Chemical Geology*, 222.1-2: 1-22.

Fagel, N., Boski, T., Likhoshway, L., Oberhaensli, H. (2003). "Late Quaternary Clay Mineral Record in Central Lake Baikal (Academician Ridge, Siberia)." *Palaeogeography, Palaeoclimatology, Palaeoecology*, 193.1: 159-79.

Farmer, V. C., Wilson, M. J. (1970). "Experimental Conversion of Biotite to Hydrobiotite." *Nature*, 226.5248: 841-2.

Forman, S. L., Miller, G.H. (1984). "Time-Dependent Soil Morphologies and Pedogenic Processes on Raised Beaches, Bröggerhalvöya, Spitsbergen, Svalbard Archipelago." *Arctic and Alpine Research*, 16.4: 381-94.

Forman, S. L., Lubinski, D. J., Ingolfson, O., Zeeberg, J. J., Snyder, J.A., Siegert, M. J., Matishov G. G. (2004). "A review of Postglacial Emergence on Svalbard, Franz Josef Land Novaya Zemla, Northern Eurasia." *Quaternary Science Reviews*, 23: 1391-1434.

Forman, S. L., Mann, D. H., Miller, G. H. (1987). "Late Weichselian and Holocene Relative Sea-level History of Broggerhalvoya, Spitsbergen." *Quaternary Research*, 27: 41-50.

Galan, E.; Bergaya, F., Theng, B.K.G., and Lagaly G., (ed.) (2006). “Genesis of Clay Minerals” *Handbook of Clay Science.* Elsevier: 1129-1167.

Gonzalez, L. A., Carpenter, S.J., Lohmann, K. C. (1992). "Inorganic Calcite Morphology - Roles of Fluid Chemistry and Fluid-Flow." *Journal of Sedimentary Petrology*, 62.3: 382-399.

Grove, J. M. (2001). "The Initiation of the "Little Ice Age" in Regions Round the North Atlantic." *Climatic Change,* 48.1: 53-82.

Guilizzoni, P., Marchetto, A., Lami, A., Brauer, A., Vigliotti, L., Musazzi, S., Langone, L., Manca, M., Lucchini, F., Calanchi, N., Dinelli, E., Mordenti, A. (2006). "Records of Environmental and Climatic Changes during the Late Holocene from Svalbard: Palaeolimnology of Kongressvatnet." *Journal of Paleolimnology,* 36.4: 325-51.

Hjelle, A., Lauritzen, Ø., Salvigsen, O., Winsnes, T.S. (1986). Geological map, Svalbard, B10G Van Mijenfjorden, Norsk Polarinstitutt, Temakart 2: Oslo, Norsk Polarinstitutt, scale 1:100000.

Hjelle, A. (1993). *The Geology of Svalbard.* Oslo, Norsk Polarinstitutt.

Hughen, K. A., Southon, J. R., Lehman, S. J., Overpeck, J. T. (2000). "Synchronous Radiocarbon and Climate Shifts during the Last Deglaciation." *Science,* 290.5498: 1951-4.

Humlum, O., Elberling, B., Hormes, A., Fjordheim, K., Hansen, O. H., Heinemeier, J. (2005). "Late Holocene Glacier Growth in Svalbard, Documented by Subglacial Relict Vegetation and Living Soil Microbes." *The Holocene,* 15.3: 396-407.

Humphrey, J. D., Howell, R. P. (1999). "Effect of Differential Stress on Strontium Partitioning in Calcite." *Journal of Sedimentary Researc*h, 69.1: 208-15.

Ingólfsson, Ó. (2006). "Outline of the Geography and Geology of Svalbard." UNIS Course Packet.

Inskeep, W. P., Bloom, P. R. (1986). "Kinetics of Calcite Precipitation in the Presence of Water-Soluble Organic Ligands." *Soil Science Society of America Journal,* 50.5: 1167-72.

Jackson, M.L. (1969). *Soil Chemical Analysis – Advanced Course.* Second Edition. Library of Congress Catalogue. USA.

Jin, Z., Li, F., Cao, J.,Wang, S., Yu, J. (2006). "Geochemistry of Daihai Lake Sediments, Inner Mongolia, North China: Implications for Provenance, Sedimentary Sorting, and Catchment Weathering." *Geomorphology,* 80.3-4: 147-63.

Jones, V. J., Birks, H. J. B. (2004). "Lake-Sediment Records of Recent Environmental Change on Svalbard: Results of Diatom Analysis." *Journal of Paleolimnology,* 31.4: 445-66.

Krishnaswamy, S., Lal, D., Martin, J. M., Meybeck, M. (1971). "Geochronology of Lake Sediments." *Earth and Planetary Science Letters,* 11.1-5: 407-14.

Lacelle, D. (2007). "Environmental Setting, (Micro)Morphologies and Stable C–O Isotope Composition of Cold Climate Carbonate precipitates—a Review and Evaluation of their Potential as Paleoclimatic Proxies." *Quaternary Science Reviews,* 26.11-12: 1670-89.

Lambeck, K. (1995). "Constraints on the Late Weichselian Ice Sheet Over the Barents Sea from Observations of Raised Shorelines." *Quaternary Science Reviews,* 14.1: 1-16.

Lan, X., Wang, H., Li, R., Lin, Z., Zhang, Z. (2007). "Major Elements Composition and Provenance Analysis in the Sediments of the South Yellow Sea." *Earth Science Frontiers,* 14.4 : 197-203.

Landvik, J. Y., Bondevik, S., Elverhøi, A., Fjeldskaar,W., Mangerud, J., Salvigsen, O., Siegert, M. J., Svendsen, J-I., Vorren, T. O. (1998). "The Last Glacial Maximum of Svalbard and the Barents Sea Area: Ice Sheet Extent and Configuration." *Quaternary Science Reviews,* 17.1-3: 43-75.

Leonard, E., (1986). "Use of lacustrine sedimentary sequences as indicators of Holocene glacial history, Banff National Park, Alberta, Canada." *Quaternary Research,* 26: 218-231.

Lorens, R. B. (1981). "Sr, Cd, Mn and Co Distribution Coefficients in Calcite as a Function of Calcite Precipitation Rate." *Geochimica et Cosmochimica Acta,* 45.4: 553-61.

Malone, M.J. and Baker P.A. (1999). "Temperature Dependence of the Strontium Distribution Coefficient in Calcite: An Experimental Study from 40° to 200°c and Application to Natural Diagenetic Calcites." *Journal of Sedimentary Research,* 69.1: 216-23.

Mangerud, J., Landvik, J. (2007). "Younger Dryas Cirque Glaciers in Western Spitsbergen: Smaller than during the Little Ice Age." *Boreas,* 36.3: 278-85.

Mangerud, J., Dokken,T., Hebbeln, D., Heggen, B., Ingólfsson, Ó., Landvik, J.Y., Mejdahl, V., Svendsen, J. I., Vorren, T. O. (1998). "Fluctuations of the Svalbard-Barents Sea Ice Sheet during the Last 150 000 Years." *Quaternary Science Reviews,* 17.1-3: 11-42.

Mangerud, J., Svendsen, J. I. (1992). "The Last Interglacial-Glacial Period on Spitsbergen, Svalbard." *Quaternary Science Reviews,* 11.6: 633-64.

Moore, D. M., Reynolds, R. C. (1997). *X-Ray Diffraction and the Identification and Analysis of Clay Minerals.* Oxford; New York: Oxford University Press.

Mucci, A., Morse, J. W. (1983). "The Incorporation of Mg2+ and Sr2+ into Calcite Overgrowths: Influences of Growth Rate and Solution Composition." *Geochimica et Cosmochimica Acta,* 47.2: 217-33.

Nawrocki, J. (1999). "Paleomagnetism of Permian through Early Triassic Sequences in Central Spitsbergen: Implications for Paleogeography." *Earth and Planetary Science Letters,* 169.1-2: 59-70.

Nesje, A., Dahl, S., Thun, T., Nordli, Ã. (2008). "The 'Little Ice Age' Glacial Expansion in Western Scandinavia: Summer Temperature Or Winter Precipitation?" *Climate Dynamics,*30.7: 789-801.

Neumann, T., Rausch, N., Leipe, T., Dellwig, O., Berner, Z., Böttcher, M. E. (2005). "Intense Pyrite Formation Under Low-Sulfate Conditions in the Achterwasser Lagoon, SW Baltic Sea." *Geochimica et Cosmochimica Acta,* 69.14: 3619-30.

Norrish, K., Chappel, B.W.; Zussman, J. (ed.) (1977). "X-Ray Fluorescence Spectrometry." *Physical Methods in Determinate Mineralogy,* p. 235.

Norrish, K., Hutton, J. T. (1969). "An Accurate X-Ray Spectrographic Method for the Analysis of a Wide Range of Geological Samples." *Geochimica et Cosmochimica Acta,* 33.4: 431-53.

Ottesen, D., Dowdeswell, J.A., Benn, D.I., Kristensen, L., Christiansen, H.H., Christensen, O., Hansen, L., Lebesbye, E., Forwick, M., Vorren, T.O. (2008). "Submarine Landforms Characteristic of Glacier Surges in Two Spitsbergen Fjords." *Quaternary Science Reviews,* 27.15-16: 1583-99.

Overpeck, J., Hughen, K., Hardy, D., Bradley, R., Case, R., Douglas, M., Finney, B. Gajewski, K., Jacoby, G., Jennings, A., Lamoureux, S., Lasca, A., MacDonald, G., Moore, J., Retelle, M., Smith, S., Wolfe, A., Zielinski, G. (1997). "Arctic Environmental Change of the Last Four Centuries." *Science,* 278.5342:1251.

Peel, M. C., Finlayson, B. L., McMahon, T. A. (2007). "Updated world map of the Köppen-Geiger climate classification". *Hydrology Earth System Science,* 11:1633-1644.

Pinglot, J. F., Pourchet, M., Lefauconnier, B., Ove Hagen, J., Isaksson, E., Vaikmäe, R., Kamiyama, K. (1999). "Accumulation in Svalbard Glaciers Deduced from Ice

Cores with Nuclear Tests and Chernobyl Reference Layers." *Polar Research,* 18.2: 315-21.

Prestrud Anderson, S., Drever, J. I., Humphrey, N. F. (1997). "Chemical Weathering in Glacial Environments." *Geology,* 25.5: 399-402.

Rosen, M. R., Coshell, L. (1992) "A New Location of Holocene Dolomite Formation, Lake Hayward, Western Australia." *Sedimentology,* 39.1: 161.

Saalman, K., Thiedig, F. (2002). "Thrust Tectonics on Broggerhalvoya and their Relationship to the Tertiary West Spitsbergen Fold-and-Thrust Belt." *Geology Magazine*, 139: 47-72.

Schaetzl, R. J., Anderson, S. (2005). *Soils: Genesis and Geomorphology*. Cambridge; New York: Cambridge University Press.

Schaller, T. H., Moor C., Wehrli, B. (1997). "Sedimentary Profiles of Fe, Mn, V, Cr, as and Mo as Indicators of Benthic Redox Conditions in Baldeggersee." *Aquatic Sciences - Research Across Boundaries,* 59.4: 345-61.

Sharp, M., Creaser, R. A., Skidmore, M. (2002). "Strontium Isotope Composition of Runoff from a Glaciated Carbonate Terrain." *Geochimica et Cosmochimica Acta,* 66.4: 595-614.

Smol, J. P., Walker, I. R., Leavitt, P. R. (1991). "Paleolimnology and Hindcasting Climate Trends." *International Association of Theoretical and Applied Limnology*, 24.2: 1240-6

Środoń, J. (1999). "Nature of Mixed-Layer Clays and Mechanisms of Their Formation and Alteration." *Annual Review of Earth and Planetary Sciences,* 27.1: 19-53.

Sternbeck, J., Sohlenius, G. (1997). "Authigenic Sulfide and Carbonate Mineral Formation in Holocene Sediments of the Baltic Sea." *Chemical Geology,* 135.1-2: 55-73.

Sunagawa, I., Takahashi, Y., Imai,. (2007). "Strontium and Aragonite-Calcite Precipitation." *Journal of Mineralogical and Petrological Sciences*, 102.3: 174-81.

Svendsen, J. I.; Mangerud, J. (ed.) (1997). *Holocene Glacial and Climatic Variations on Spitsbergen, Svalbard,* Vol. 7. United Kingdom: Edward Arnold : Sevenoaks, United Kingdom.

Takahashi, T., Broecker, W., Li, Y. H., Thurber, D. (1968). "Chemical and Isotopic Balances for a Meromictic Lake." *Limnology and Oceanography,* 13.2: 272-92.

Tang, J., Köhler, S. J., Dietzel, M. (2008). "Sr2+/Ca2+ and 44Ca/40Ca Fractionation during Inorganic Calcite Formation: I. Sr Incorporation." *Geochimica et Cosmochimica Acta,* 72.15: 3718-32.

U.S. Geological Survey Certificate of Analysis: Basalt, Hawaiian Volcano Observatory, BHVO-1. *U.S. Geological survey.* <http://minerals.cr.usgs.gov/geo_chem_stand/basaltbhvo1.html> [04 Dec. 2008]. Last Accessed 13 Mar 2009.

U.S. Geological Survey Certificate of Analysis: Granite, G-2. *U.S. Geological survey.* <http://minerals.cr.usgs.gov/geo_chem_stand/granite.html> [04 Dec. 2008]. Last Accessed 13 Mar 2009.

Viscosi-Shirley, C., Mammone, K., Pisias, N., Dymond, J.(2003). "Clay Mineralogy and Multi-Element Chemistry of Surface Sediments on the Siberian-Arctic Shelf: Implications for Sediment Provenance and Grain Size Sorting." *Continental Shelf Research,* 23.11-13: 1175-200.

Vogt, C., Knies, J. (2008). "Sediment Dynamics in the Eurasian Arctic Ocean during the Last Deglaciation — the Clay Mineral Group Smectite Perspective." *Marine Geology,*250.3-4: 211-22.

Werner, A. (1993). Holocene moraine chronology, Spitsbergen, Svalbard: lichenometric evidence for multiple Neoglacial advances in the Arctic. *The Holocene* 3:128–137

White, A. F., Blum, A. E. (1995). "Effects of Climate on chemical_ Weathering in Watersheds." *Geochimica et Cosmochimica Acta*, 59.9: 1729-47.

Willem, G. M. van der Bilt (2009). *"Post Little Ice Age environmental change documented in lake sediments from Kongressvatnet, Spitsbergen."* Senior thesis, Utrecht University, The University Centre in Svalbard.

Yang, S., Youn, J-S. (2007). "Geochemical Compositions and Provenance Discrimination of the Central South Yellow Sea Sediments." *Marine Geology*, 243.1-4: 229-41.

Whie Fan Bulk (<2.38 mm)

Sample	Nb ppm	Zr ppm	Y ppm	Sr ppm	U ppm	Rb ppm	Th ppm	Pb ppm	Ga ppm	Zn ppm	Ni ppm	Cr ppm	V ppm	Ce ppm	Ba ppm	La ppm
WF002	3.3	100	7.6	112	2	20.1	2	4	3	22	8	37	27	20	83	8
WF005	2.8	96	7.0	127	2	18.0	2	4	2	19	8	31	22	18	69	5
WF007	3.2	96	7.3	125	2	20.4	3	5	3	21	9	32	26	20	87	8
WF009	2.9	101	7.0	124	2	19.0	2	4	3	20	8	34	25	20	84	6
WF015	4.4	147	9.9	104	3	29.5	3	7	4	29	12	48	32	22	110	10
WF016	4.4	118	9.5	108	3	29.7	3	8	4	29	12	53	33	25	111	10
Average	*3.50*	*109.67*	*8.05*	*116.67*	*2.33*	*22.78*	*2.50*	*5.33*	*3.17*	*23.33*	*9.50*	*39.17*	*27.50*	*20.83*	*90.67*	*7.83*
STDEV	*0.72*	*20.03*	*1.30*	*9.87*	*0.52*	*5.35*	*0.55*	*1.75*	*0.75*	*4.50*	*1.97*	*9.15*	*4.23*	*2.40*	*16.57*	*2.04*

White Fan <63 µm

Sample	Nb ppm	Zr ppm	Y ppm	Sr ppm	U ppm	Rb ppm	Th ppm	Pb ppm	Ga ppm	Zn ppm	Ni ppm	Cr ppm	V ppm	Ce ppm	Ba ppm	La ppm
WF002	4.1	141	9.3	90	3	26.6	3	8	4	30	10	44	29	22	93	10
WF005	4.9	226	11.0	96	4	31.6	4	13	4	38	13	54	34	27	103	10
WF007	4.5	157	10.1	94	3	31.4	4	14	4	36	13	52	34	26	109	12
WF009	4.6	170	10.2	93	3	29.7	3	9	4	33	12	56	32	24	109	12
WF015	4.8	170	10.7	98	3	30.3	3	10	4	35	13	44	32	25	107	10
WF016	4.8	130	10.3	98	3	33.2	4	11	5	36	13	50	35	23	108	10
Average	*4.62*	*165.67*	*10.27*	*94.83*	*3.17*	*30.47*	*3.50*	*10.83*	*4.17*	*34.67*	*12.33*	*50.00*	*32.67*	*24.50*	*104.83*	*10.67*
STDEV	*0.29*	*33.57*	*0.58*	*3.13*	*0.41*	*2.24*	*0.55*	*2.32*	*0.41*	*2.80*	*1.21*	*5.06*	*2.16*	*1.87*	*6.21*	*1.03*

Black Fan Bulk

Sample	Nb ppm	Zr ppm	Y ppm	Sr ppm	U ppm	Rb ppm	Th ppm	Pb ppm	Ga ppm	Zn ppm	Ni ppm	Cr ppm	V ppm	Ce ppm	Ba ppm	La ppm
BF002 0-2 cm	8.0	164	15.8	47	1	51.9	5	11	7	67	27	68	57	41	142	18
BF002 5-10 cr	8.8	174	20	44	1	56	6	10	7	79	36	83	58	46	126	20
BF003 5-10 cr	6.9	141	14.9	42	1	45.8	5	8	6	86	33	128	52	36	120	16
BF002 10-15 c	8.6	164	18.3	43	2	54.2	6	10	7	82	37	94	58	44	119	18
BF003 0-2 cm	10.5	239	17.9	51	2	56.3	6	12	8	73	29	77	63	51	162	20
BF006	10.5	192	19.1	42	2	50.5	7	10	7	81	42	123	56	48	112	21
BF012	6.9	123	12.7	51	1	45.7	4	7	6	62	27	74	49	35	101	13
BF016	**14.7**	**396**	**28.9**	**68**	**3**	**66.4**	**10**	**19**	**9**	**100**	**39**	**122**	**71**	**63**	**195**	**28**
Average	*9.36*	*199.13*	*18.45*	*48.50*	*1.63*	*53.35*	*6.13*	*10.88*	*7.13*	*78.75*	*33.75*	*96.13*	*58.00*	*45.50*	*134.63*	*19.25*
STDEV	*2.56*	*86.75*	*4.86*	*8.70*	*0.74*	*6.68*	*1.81*	*3.64*	*0.99*	*11.78*	*5.68*	*24.58*	*6.72*	*8.99*	*30.76*	*4.37*

Black Fan <63 µm

Sample	Nb ppm	Zr ppm	Y ppm	Sr ppm	U ppm	Rb ppm	Th ppm	Pb ppm	Ga ppm	Zn ppm	Ni ppm	Cr ppm	V ppm	Ce ppm	Ba ppm	La ppm
BF003 0-2 cm	16.2	393	29.7	65	3	78	11	20	11	103	35	101	80	71	215	28
BF003 5-10 cr	16.2	328	36.1	60	3	84.6	12	24	11	166	50	122	85	68	206	35
BF002 0-2 cm	14.1	293	30.4	65	2	80.6	10	25	11	107	34	88	81	68	214	30
BF002 5-10 cr	13.4	269	33.9	53	3	78.5	9	22	10	111	44	92	72	62	163	28
BF002 10-15 c	14.7	291	34.3	57	3	83.8	11	24	11	136	52	102	77	67	173	29
BF012	17.7	336	36.9	73	4	111.7	13	33	14	173	66	156	110	85	215	39
BF016	**19.6**	**564**	**39.3**	**77**	**4**	**82.0**	**13**	**29**	**11**	**127**	**46**	**132**	**82**	**76**	**229**	**34**
Average	*15.99*	*353.43*	*34.37*	*64.29*	*3.14*	*85.60*	*11.29*	*25.29*	*11.29*	*131.86*	*46.71*	*113.29*	*83.86*	*71.00*	*202.14*	*31.86*
STDEV	*2.16*	*101.27*	*3.45*	*8.54*	*0.69*	*11.77*	*1.50*	*4.39*	*1.25*	*28.24*	*10.93*	*24.57*	*12.24*	*7.48*	*24.46*	*4.22*

Core sediments (bulk)

Sample	Nb ppm	Zr ppm	Y ppm	Sr ppm	U ppm	Rb ppm	Th ppm	Pb ppm	Ga ppm	Zn ppm	Ni ppm	Cr ppm	V ppm	Ce ppm	Ba ppm	La ppm
WF 213-238 n	5.9	99	12.5	119	3	50.3	5	9	7	50	19	74	49	32	123	14
DB 0-22 mm	6.2	92	13.3	155	3	52.5	5	16	7	67	24	75	54	35	127	16
DB 30-40 mm	5.4	119	11.8	119	3	41.1	4	8	6	42	16	63	42	29	115	14
DB 99-111mm	3.9	71	9.8	114	3	31.3	3	5	4	30	12	51	32	24	83	11
DB 195-211m	4.3	95	10.2	117	3	34.1	3	5	5	32	12	62	34	25	105	12
DB 383-400 m	6.9	96	14.7	141	3	60.2	5	10	9	68	25	85	65	40	133	17
Average	*5.43*	*95.33*	*12.05*	*127.50*	*3.00*	*44.92*	*4.17*	*8.83*	*6.33*	*48.17*	*18.00*	*68.33*	*46.00*	*30.83*	*114.33*	*14.00*

North Shore Sample

Sample	Nb ppm	Zr ppm	Y ppm	Sr ppm	U ppm	Rb ppm	Th ppm	Pb ppm	Ga ppm	Zn ppm	Ni ppm	Cr ppm	V ppm	Ce ppm	Ba ppm	La ppm
KI102 <2.38µı	2.7	79	7	156	2	22.2	2	6	3	21	8	43	25	20	93	8
KI102 <63µm	4.6	140	9.8	98	3	37.6	4	14	5	43	14	51	38	27	116	12

Appendix 2: Major element chemistry of surface sediments

Whie Fan Bulk (<2.38 mm)

Sample	Nb ppm	Zr ppm	Y ppm	Sr ppm	U ppm	Rb ppm	Th ppm	Pb ppm	Ga ppm	Zn ppm	Ni ppm	Cr ppm	V ppm	Ce ppm	Ba ppm	La ppm
WF002	3.3	100	7.6	112	2	20.1	2	4	3	22	8	37	27	20	83	8
WF005	2.8	96	7.0	127	2	18.0	2	4	2	19	8	31	22	18	69	5
WF007	3.2	96	7.3	125	2	20.4	3	5	3	21	9	32	26	20	87	8
WF009	2.9	101	7.0	124	2	19.0	2	4	3	20	8	34	25	20	84	6
WF015	4.4	147	9.9	104	3	29.5	3	7	4	29	12	48	32	22	110	10
WF016	4.4	118	9.5	108	3	29.7	3	8	4	29	12	53	33	25	111	10
Average	*3.50*	*109.67*	*8.05*	*116.67*	*2.33*	*22.78*	*2.50*	*5.33*	*3.17*	*23.33*	*9.50*	*39.17*	*27.50*	*20.83*	*90.67*	*7.83*
STDEV	*0.72*	*20.03*	*1.30*	*9.87*	*0.52*	*5.35*	*0.55*	*1.75*	*0.75*	*4.50*	*1.97*	*9.15*	*4.23*	*2.40*	*16.57*	*2.04*

White Fan <63 µm

Sample	Nb ppm	Zr ppm	Y ppm	Sr ppm	U ppm	Rb ppm	Th ppm	Pb ppm	Ga ppm	Zn ppm	Ni ppm	Cr ppm	V ppm	Ce ppm	Ba ppm	La ppm
WF002	4.1	141	9.3	90	3	26.6	3	8	4	30	10	44	29	22	93	10
WF005	4.9	226	11.0	96	4	31.6	4	13	4	38	13	54	34	27	103	10
WF007	4.5	157	10.1	94	3	31.4	4	14	4	36	13	52	34	26	109	12
WF009	4.6	170	10.2	93	3	29.7	3	9	4	33	12	56	32	24	109	12
WF015	4.8	170	10.7	98	3	30.3	3	10	4	35	13	44	32	25	107	10
WF016	4.8	130	10.3	98	3	33.2	4	11	5	36	13	50	35	23	108	10
Average	*4.62*	*165.67*	*10.27*	*94.83*	*3.17*	*30.47*	*3.50*	*10.83*	*4.17*	*34.67*	*12.33*	*50.00*	*32.67*	*24.50*	*104.83*	*10.67*
STDEV	*0.29*	*33.57*	*0.58*	*3.13*	*0.41*	*2.24*	*0.55*	*2.32*	*0.41*	*2.80*	*1.21*	*5.06*	*2.16*	*1.87*	*6.21*	*1.03*

Black Fan Bulk

Sample	Nb ppm	Zr ppm	Y ppm	Sr ppm	U ppm	Rb ppm	Th ppm	Pb ppm	Ga ppm	Zn ppm	Ni ppm	Cr ppm	V ppm	Ce ppm	Ba ppm	La ppm
BF002 0-2 cm	8.0	164	15.8	47	1	51.9	5	11	7	67	27	68	57	41	142	18
BF002 5-10 cr	8.8	174	20	44	1	56	6	10	7	79	36	83	58	46	126	20
BF003 5-10 cr	6.9	141	14.9	42	1	45.8	5	8	6	86	33	128	52	36	120	16
BF002 10-15 c	8.6	164	18.3	43	2	54.2	6	10	7	82	37	94	58	44	119	18
BF003 0-2 cm	10.5	239	17.9	51	2	56.3	6	12	8	73	29	77	63	51	162	20
BF006	10.5	192	19.1	42	2	50.5	7	10	7	81	42	123	56	48	112	21
BF012	6.9	123	12.7	51	1	45.7	4	7	6	62	27	74	49	35	101	13
BF016	**14.7**	**396**	**28.9**	**68**	**3**	**66.4**	**10**	**19**	**9**	**100**	**39**	**122**	**71**	**63**	**195**	**28**
Average	*9.36*	*199.13*	*18.45*	*48.50*	*1.63*	*53.35*	*6.13*	*10.88*	*7.13*	*78.75*	*33.75*	*96.13*	*58.00*	*45.50*	*134.63*	*19.25*
STDEV	*2.56*	*86.75*	*4.86*	*8.70*	*0.74*	*6.68*	*1.81*	*3.64*	*0.99*	*11.78*	*5.68*	*24.58*	*6.72*	*8.99*	*30.76*	*4.37*

Black Fan <63 µm

Sample	Nb ppm	Zr ppm	Y ppm	Sr ppm	U ppm	Rb ppm	Th ppm	Pb ppm	Ga ppm	Zn ppm	Ni ppm	Cr ppm	V ppm	Ce ppm	Ba ppm	La ppm
BF003 0-2 cm	16.2	393	29.7	65	3	78	11	20	11	103	35	101	80	71	215	28
BF003 5-10 cr	16.2	328	36.1	60	3	84.6	12	24	11	166	50	122	85	68	206	35
BF002 0-2 cm	14.1	293	30.4	65	2	80.6	10	25	11	107	34	88	81	68	214	30
BF002 5-10 cr	13.4	269	33.9	53	3	78.5	9	22	10	111	44	92	72	62	163	28
BF002 10-15 c	14.7	291	34.3	57	3	83.8	11	24	11	136	52	102	77	67	173	29
BF012	17.7	336	36.9	73	4	111.7	13	33	14	173	66	156	110	85	215	39
BF016	**19.6**	**564**	**39.3**	**77**	**4**	**82.0**	**13**	**29**	**11**	**127**	**46**	**132**	**82**	**76**	**229**	**34**
Average	*15.99*	*353.43*	*34.37*	*64.29*	*3.14*	*85.60*	*11.29*	*25.29*	*11.29*	*131.86*	*46.71*	*113.29*	*83.86*	*71.00*	*202.14*	*31.86*
STDEV	*2.16*	*101.27*	*3.45*	*8.54*	*0.69*	*11.77*	*1.50*	*4.39*	*1.25*	*28.24*	*10.93*	*24.57*	*12.24*	*7.48*	*24.46*	*4.22*

Core sediments (bulk)

Sample	Nb ppm	Zr ppm	Y ppm	Sr ppm	U ppm	Rb ppm	Th ppm	Pb ppm	Ga ppm	Zn ppm	Ni ppm	Cr ppm	V ppm	Ce ppm	Ba ppm	La ppm
WF 213-238 m	5.9	99	12.5	119	3	50.3	5	9	7	50	19	74	49	32	123	14
DB 0-22 mm	6.2	92	13.3	155	3	52.5	5	16	7	67	24	75	54	35	127	16
DB 30-40 mm	5.4	119	11.8	119	3	41.1	4	8	6	42	16	63	42	29	115	14
DB 99-111mm	3.9	71	9.8	114	3	31.3	3	5	4	30	12	51	32	24	83	11
DB 195-211m	4.3	95	10.2	117	3	34.1	3	5	5	32	12	62	34	25	105	12
DB 383-400 m	6.9	96	14.7	141	3	60.2	5	10	9	68	25	85	65	40	133	17
Average	*5.43*	*95.33*	*12.05*	*127.50*	*3.00*	*44.92*	*4.17*	*8.83*	*6.33*	*48.17*	*18.00*	*68.33*	*46.00*	*30.83*	*114.33*	*14.00*

North Shore Sample

Sample	Nb ppm	Zr ppm	Y ppm	Sr ppm	U ppm	Rb ppm	Th ppm	Pb ppm	Ga ppm	Zn ppm	Ni ppm	Cr ppm	V ppm	Ce ppm	Ba ppm	La ppm
KI102 <2.38µı	2.7	79	7	156	2	22.2	2	6	3	21	8	43	25	20	93	8
KI102 <63µm	4.6	140	9.8	98	3	37.6	4	14	5	43	14	51	38	27	116	12

Appendix 5: Lake ice activity calculations

Depth m	Cl^- mol	SO_4^{2-} mol	Na^+ mol	K^+ mol	Mg^{2+} mol	Ca^{2+} mol	pH	Sum acid	Sum base	HCO_3^- (mol/L)
2-3 m	4.3E-04	5.0E-03	3.1E-04	1.6E-05	4.2E-04	5.0E-03	8.0E+00	1.1E-02	1.1E-02	6.1E-04
3-4 m	2.8E-04	3.3E-03	2.0E-04	1.1E-05	2.7E-04	3.2E-03	8.0E+00	7.2E-03	7.0E-03	2.6E-04
2-2.5 m	7.3E-04	8.5E-03	5.3E-04	2.7E-05	7.7E-04	8.5E-03	8.1E+00	1.9E-02	1.8E-02	1.3E-03
0-2m	1.4E-04	1.6E-03	1.0E-04	5.1E-06	1.5E-04	1.7E-03	9.1E+00	3.7E-03	3.4E-03	3.3E-04

Activity -- Iteration 1								
Ionic Strength (1)	[Ca] gamma	[HCO3] gamma	[Cl] gamma	[SO4] Gamma	[Na] gamma	[K] gamma	[Mg] gamma	[H+] gamma
2.2E-02	5.1E-01	8.5E-01	8.5E-01	5.1E-01	8.5E-01	8.5E-01	5.1E-01	8.5E-01
1.4E-02	5.8E-01	8.7E-01	8.7E-01	5.8E-01	8.7E-01	8.7E-01	5.8E-01	8.7E-01
3.7E-02	4.2E-01	8.0E-01	8.0E-01	4.2E-01	8.0E-01	8.0E-01	4.2E-01	8.0E-01
7.2E-03	6.8E-01	9.1E-01	9.1E-01	6.8E-01	9.1E-01	9.1E-01	6.8E-01	9.1E-01

Activity -- Iteration 1 (gamma * initial concentration) cont.								Activity -- Iteration 2 (gamma2 * initial concentration)			
Cl- Activity	SO42- Activity	Na+ Activity	K+ Activity	Mg2+ Activity	Ca2+ Activity	H+ Activity	HCO3- Activity	Ionic Strength (2)	[Ca] Gamma2	HCO3- Gamma2	Ca2+ Activity
3.6E-04	2.6E-03	2.6E-04	1.4E-05	2.2E-04	2.6E-03	9.5E-09	5.2E-04	1.1E-02	6.2E-01	8.9E-01	3.1E-03
2.4E-04	2.0E-03	1.8E-04	9.4E-06	1.6E-04	1.9E-03	8.5E-09	2.3E-04	8.3E-03	6.6E-01	9.0E-01	2.1E-03
5.8E-04	3.6E-03	4.3E-04	2.2E-05	3.2E-04	3.6E-03	6.5E-09	1.1E-03	1.6E-02	5.6E-01	8.7E-01	4.8E-03
1.3E-04	1.1E-03	9.2E-05	4.6E-06	1.0E-04	1.1E-03	7.4E-10	3.0E-04	5.0E-03	7.3E-01	9.2E-01	1.2E-03